20030128062

AD-A176 630

GC-TR-86-1536

VOLUME I OF II

CHEMICAL AND ELECTROMAGNETIC METHODS FOR HIGH EXPLOSIVE/ORDNANCE DETECTION

GEO-CENTERS, INC.

GC-TR-86-1536

VOLUME I OF II
CHEMICAL AND ELECTROMAGNETIC METHODS FOR HIGH EXPLOSIVE/ORDNANCE DETECTION

PREPARED FOR

NAVAL RESEARCH LABORATORY
4555 OVERLOOK AVENUE, S.W.
WASHINGTON, DC 20375-5000

UNDER CONTRACT NO. N00014-84-C-2399

PREPARED BY

GEO-CENTERS, INC.
7 WELLS AVENUE
NEWTON CENTRE, MASSACHUSETTS 02159

NOVEMBER, 1986

GEO-CENTERS, INC.

INTRODUCTION

The United States Navy is the lead service for the development of explosive ordnance disposal (EOD) technology. In addition to its routine research activities it has more recently been tasked, through the U.S. Army Corps of Engineers, to assist in the response to the provisions of Public Law 98-212 requiring the Department of Defense to institute a remedial action plan to decontaminate various domestic sites polluted with hazardous explosive materials. Lastly, the Federal Aviation Administration (FAA), in response to increasing terrorist threats against civilian aircraft, has requested assistance of the DOD's EOD community in developing technologies for the detection of explosive materials and/or their associated components.

The focal points for these Naval activities have been the Naval Explosive Ordnance Disposal Technology Center (NAVEODTECHCEN) and the Naval Research Laboratory (NRL). In support of these agencies, GEO-CENTERS has completed a two-year research effort under NRL contract number N00014-84-C-2399 to investigate a number of alternate technologies, each appropriate to various aspects of the detection problem.

The statement of work for this effort is presented separately below. For the purposes of this report the nine specific tasks have been grouped into 5 distinct areas, each of which is described separately in different chapters. Tasks 1 and 2 are grouped under the heading of Optoacoustic Detection of Explosive Vapors; Tasks 3 and 4 are grouped under Surface Towed Ordnance Locator System; Task 5 is discussed under Ground Penetrating Radar for Ordnance Location; Task 6 is covered under Electromagnetic

Tagging of Electric Blasting Caps; Task 7 calling for field measurements is detailed under the individual chapters; Task 8 (documentation) is addressed by the final report, as well as detailed progress reports; and Task 9, calling for portions of the work to be performed at NRL, has been appropriate to Tasks 1 and 2 only. An additional section, Borehole Ordnance Detection System has resulted from a specialized hybrid of Tasks 4 and 5.

Each of the five technical chapters stands alone. Edited versions of some of these chapters have appeared or will do so as separate publications. The technical chapters appear in the following order (Volume I):

Section 1 - Optoacoustic Detection of Explosive Vapors
Section 2 - Surface Towed Ordnance Locator System
Section 3 - Borehole Ordnance Detection System
Section 4 - Ground Penetrating Radar for Ordnance Location
Section 5 - Electromagnetic Tagging of Electric Blasting Caps

In addition, there are 6 appendices (Volume II):

Appendix A - Geomagnetic Units
Appendix B - Mathematic Derivation of Magnatic Anomaly Model
Appendix C - Electromagnetic Propagation
Appendix D - Summary of Signal and Image Processing Techniques
Appendix E - Field Test Sites
Appendix F - Fortran Program to Model Microstrip Parameters

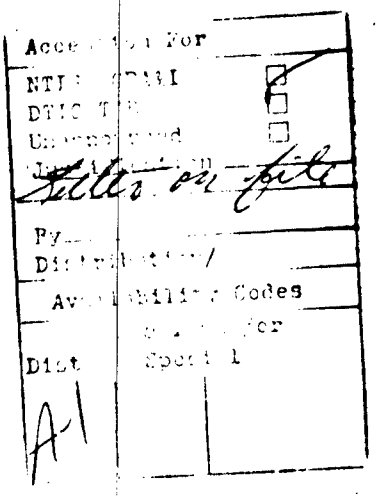

GEO-CENTERS, INC.

STATEMENT OF WORK

Because of the need to reclaim land or waterways which have been previously used as battlefields or test ranges, the Department of Defense must design and develop instrumentation and procedures, based upon chemical and physical principles, to access, detect, and render-safe unexploded ordnance of both conventional and improvised designs. There is interest in both fixed sensors, capable of detecting (e.g. a checkpoint monitor) the presence or passage of high explosive materials and components and in mobile sensors for the surveying of both open and developed areas. Detection methods can range from both active and passive chemical sensors to electromagnetic techniques; viable options include the introduction of taggants to assist in detection. All sensors have as design goals 100% detection efficiencies with minimal false alarm rates. The contractor shall perform the following tasks:

(1) Develop a passive chemical sensor ("sniffer") capable of detecting and discriminating low concentrations of NO or other chemical compounds uniquely associated with high explosives. A variety of instrumental methodologies are potentially appropriate. In addition to instrument sensitivity, processing techniques, capable of correlating results and enhancing signal to noise, will be necessary.

(2) Develop a chemical sensor based upon electrooptical techniques capable of detecting and discriminating low concentrations of nitrogen containing molecules or other chemical compounds uniquely associated with high explosives. Of interest are active laser spectroscopic methods appropriate to checkpoint operations which can accurately measure and correlate airborne concentrations and resolve compounds of interest in a complex background. Sophisticated processing methods will be required to enhance

signal to noise ratios and to improve confidence levels in detection.

(3) Develop a new class of magnetometer, based upon fiber optic technology for potential use as either a stand-alone, hand-held instrument or in an array configuration (discussed in Task (4)). Design goal is to develop a small, light, low-power, total field instrument with sensitivity better than 0.1 gamma and a heading error of less than 0.1 gamma. Instrument must be operable in both surface and underwater environments. Data output must be formatted as to be completely compatible with the (Task (4)) system to permit the potential integration of this new component sensor into a total system under parallel development.

(4) Develop a surface towed ordnance locator system (STOLS) based upon chemical or electromagnetic technology for the detection, location, and possible identification of subsurface unexploded ordnance. The system approach must consider detection sensitivities, array configurations, data processing and correlation, self signatures of instrumentation and vehicles, target signatures, background conditions, and field environments. Familiarity with target signatures of both U.S. and foreign ordnance will be required.

(5) Develop and/or refine ground penetrating radar technology as an alternate electromagnetic detection method for the detection, location, and possible identification of unexploded subsurface ordnance. To achieve both penetration depth and spatial resolution, an array of antennas ranging from 10-1000 MHz will be required. Because of noisy backgrounds encountered in field conditions, the development of directional antennas is highly desirable. As with all systems described, sophisticated data processing and interpretation capability is required to reliably extract weak signals from noisy backgrounds.

(6) Investigate the use of "taggants" or other labels to be incorporated into the manufacture of high explosive/ordnance components which can subsequently be used in their detection. Among the candidates to be considered are distinctive chemical

additives with evolution rates sufficient to provide both detectable concentrations and extended (ten year plus) lifetimes. Other candidates to be considered are miniature passive electrical circuits that uniquely respond to active probes.

(7) For each system designed and constructed conduct evaluation tests at Navy-designated test sites to characterize performance under field conditions. Parameters to be evaluated will consist of system sensitivity, resolution, detection efficiency, false alarm rate, user friendliness, and reliability in the field.

(8) Provide technical documentation of all results which will variously include: detailed technical discussion of principles of operation, evaluation of performance under laboratory and/or field conditions, operator/user manuals for instruments to be fielded, and source listings for analytical software.

(9) Portions of the research may be required to be performed at the Naval Research Laboratory or other Navy facilities as may be dictated.p

SECTION 1

OPTOACOUSTIC DETECTION OF EXPLOSIVE VAPORS

TABLE OF CONTENTS

LIST OF FIGURES

LIST OF TABLES

EXECUTIVE SUMMARY

The following report describes the work performed on Optoacoustic Detection of Explosives Vapors. The program was initiated to decrease the minimum detectable concentration of explosives using traditional optoacoustic spectroscopy by at least two orders of magnitude to approximately one part-per-trillion (ppt).

The critical concept is the introduction of Zeeman frequency modulation of the absorption resonance in and out of coincidence with a near-by laser emission line. The laser itself is amplitude modulated at a second frequency and either the sum or difference frequency used to excite the acoustic resonance in the cell. The net result of these operations is the suppression of all interfering absorptions thereby allowing the full sensitivity of the optoacoustic method to be employed.

This effort was spent in experimentally verifying predictions of a 1 part-per-trillion usable detection limit. We have observed signals at the ppb level, and have performed sufficient experimentation and analysis to extrapolate these initial results to the ppt level, as initially theoretically predicted.

1.1.0 INTRODUCTION

Research programs concerned with detection of explosives have explored two avenues for explosives detection; namely, bulk detection and vapor detection.[1] The applications of bulk detection techniques include examination of the use of X-rays, NMR/NQR, and neutron activation. Vapor detection techniques include the use of sampling networks, preconcentrators and adsorption tubes for sampling and analysis by the application of mass spectrometric, ion mobility, optical, electron capture/gas chromatography, chemiluminescence, biochemical and olfaction techniques. Recently, the FAA held a workshop to review explosives detection and generate additional approaches to the solution of the problem.[2] The laser/optical methods working group at this workshop identified three optical techniques as having the most promise for future development as explosive vapor sensors. These techniques are

- o laser multiphoton ionization (MPI) - based on generation of a small molecular fragment or daughter molecule product of explosive
- o chemiluminescence - based on the reaction NO+O3 --> NO2*; and
- o Zeeman modulated optoacoustic detection - based on detection of a small fragment molecule characteristic of explosives (e.g., NO)

MPI suffers from the need for elaborate laboratory equipment, high laser power requirements and skilled operating personnel. Instruments for the detection of chemiluminescence are commercially available, although they have not been applied at the 1 part per trillion (ppt) detection limit needed for explosives detection. The optoacoustic technique was therefore selected for development

as an explosives detection system. The optoacoustic technique was selected because:

- o it has a demonstrated high sensitivity and selectivity for NO;
- o it should ultimately have a very fast response time;
- o it has the flexibility to be used at any pressure above a few millitorr; thus, system conditions can dictate operating conditions;
- o its sensitivity increases with diluent pressure up to ~1 atm thus providing the opportunity for efficient sample collection, transfer and changing; and
- o it has the potential to be less costly to produce, operate and service.

The optoacoustic detection technique is based on the following principles:

Irradiation of a gas sample within a cell or enclosure by a laser tuned to a vibrational absorption frequency of one of the gas constituents results in vibrational excitation of these molecules. Subsequent collisional de-excitation of these energetic molecules (V-T relaxation) causes a thermalization of the absorbed energy and a pressure rise within the cell. Modulation of the gas absorption generates pressure fluctuations which can be detected with a microphone. If no other absorption artifacts or interferences are present, the acoustic signal generated is proportional to the concentration of absorber molecules in the cell.

The vapors associated with explosives are generally characterized by species containing nitrogen and oxygen.[3] While there are particular molecules such as nitromethane, EGDN, and nitrotoluenes which are common to several explosives, there is no

single vapor that is common to all explosive materials which could be used to design a chemical specific detector. Vapor detection techniques are further complicated by the extremely low vapor pressures associated with many of the explosives in use. It is further recognized that measurements need to be made in the presence of a number of time-varying potentially interfering species that may be present at significant concentrations. Thus, NO, as a derivative produced from decomposition of preconcentrated explosives vapors, represents an attractive means of monitoring the presence of explosives.

An explosives detection system based on application of the optoacoustic technique would have several components; namely,

- o A concentration/separation module - the explosive vapors are retained on a suitable substrate while atmospheric NO/N02 remain in the vapor. The retained vapors are desorbed into a sample gas stream which is NO/N02 free.
- o A decomposition module - the explosive vapors are decomposed to fragments containing NO and N02. N02 is subsequently reduced to NO.
- o An optoacoustic cell module - the NO product gas stream flows through a specially designed cell which is continuously irradiated with a low power IR laser tuned to the appropriate frequency. An electromagnet is used to generate a time varying magnetic field which tunes the NO transition in and out of resonance with the laser frequency.
- o A detection module - the Zeeman modulated optoacoustic signal is detected, amplified and correlated with the NO concentration in the cell.
- o A data processing module - the existence of microprocessors and data processing algorithms allows the raw signal to be manipulated using powerful statistical procedures.

In Section 1.2., optoacoustic theory and experimental design considerations are discussed. Section 1.3 discusses the feasibility experiments that were performed, and Section 1.4 is a summary of conclusions.

1.2.0 THEORETICAL AND EXPERIMENTAL DESIGN CONSIDERATIONS

A description of the gas phase optoacoustic effect can be separated into four parts; namely,

- o heat generation arising from collisions between gas constituents (e.g. NO) that become excited by absorbing photon energy (light) and buffer gas molecules
- o pressure waves generated from expansion of the heated volume
- o losses generated by interaction of the expansion wave with unheated molecules, cell walls, and the microphone. A portion of the microphone contribution to these losses provides the detection signal
- o noise. The signal to noise ratio determines the ultimate limit on detectivity.

Each part will be separately discussed and the implication(s) described.

1.2.1 Heat Generation

The maximum output signal will be generated for the largest number of photons absorbed. This maximum occurs when the largest number of gas molecules are illuminated with the most intense photon beam. Because of practical limitations on laser size, a trade off must be made between light intensity, beam size and number of molecules irradiated. This trade off is seen if one notes that as the light intensity increases due to telescoping of the light beam to smaller sizes, a smaller number of gas molecules are irradiated. One method used to maintain the number of molecules irradiated is to increase the path length of the photon beam

through the sample cell. An efficient means of increasing the path length is to design a cell system to accommodate multipass optics. Multipass designs exist which increase path lengths by 10-100 times.[4-8]

One restriction on the light intensity is that it remain below the onset of optical saturation. This is important since no further increases in signal can occur with increased laser intensity once optical saturation has been reached, while interfering signals can continue to increase.

In order to calculate the heat deposition, we shall assume nonsaturation of the molecular absorption which allows a rate equation description of the system. Thus, we wish to describe the time dependent behavior of a molecular excited state, N_1, in the presence of an excess of ground states, N_0. The total number of molecules in the system is $N_t=N_1+N_0$. In the system under consideration, there are two ways to create excited states, photon absorption, R_{01}, and collisional excitation, $k_{01}N_t$. The three ways to convert from an excited state into a ground state are stimulated emission, R_{10}, spontaneous emission, A_{10}, and collisional relaxation, $k_{10}Nt$. Descriptively, we can write

$$dN_1/dt = -N_1 (R_{10} + A_{10} + k_{10}Nt) + N_o (R_{01} + k_{01}N_t) \quad (1)$$

In Equation (1), R_{01} and R_{10} are time dependent variables. This makes direct integration of Equation (1) difficult.

Maximum detectivity occurs when ROl approaches the saturation limit. The relationship,

$$R_{10} = 0.1 (A_{10} + k_{10}N_t) \quad (2)$$

determines the onset of saturation. R_{01} and R_{10} are related through the degeneracy of state 1 and state 0. Also, the excited state relaxation rate, C, where

$$C = A_{10} + k_{10}N_t \simeq k_{10}N_t \qquad (3)$$

must be at least five times faster than the chopping frequency of the laser. Thus, for a pulse width, W, of a chopped laser beam, CW>5. For NO-Argon mixtures, k_{10} in pressure related units, has been measured[9] as 2×10^5 $atm^{-1}s^{-1}$. Thus, at atmospheric pressure, the pulse width of the laser is restricted to 25 μs or longer.

Under the conditions just discussed, the solution to Equation (1) is a periodic function given by,

$$N_1(t) = (N_0R_{01}/C)\{1-e^{-C(t-2nW)}\} \qquad 2nW<t<(2n+1)W \qquad (4a)$$

$$N_1(t) = (N_0R_{01}/C)(e^{CW}-1)\{e^{-C(t-2nW)}\} \qquad (2n+1)W<t<2(n+1)W \qquad (4b)$$

where n is the period number (1,2,3....).

From these equations, we note that the population difference during one laser pulse is given by

$$N_1\{(2n+1)W\}-N_1(2nW)=N_0R_{01}/C \qquad (5)$$

The heat generated, H, is calculated from

$$H = (N_0R_{01}/C)C(h\nu)V_LW \qquad (6)$$

where hν is the photon energy or the quantity of energy released by each excited molecule and V_L is the volume of gas swept out by the laser beam. Assuming one ppb NO in one atmosphere of argon with $N_o = 2.46 \times 10^{10}$ molecules/cm^3, $R_{01}=1.95 \times 10^4 s^{-1}$, $C=2 \times 10^5 s^{-1}$, $h\nu=3.7 \times 10^{-13}$ ergs, $V_L=0.124$ cm^3 and W#1/2x6150 Hz, the heat generated is calculated as $H=8.58 \times 10^{-3}$ ergs. At the cell wall, where the microphone is located, the energy density in the pressure wave, is calculated as,

$$\rho = H/V \tag{7}$$

where V is the cell volume. For a cell volume of 201 cm^3. the energy density is 1.78×10^{-5} ergs/cm^3 or 1.34×10^{-8} torr/cm^2.

1.2.2 Pressure Wave

As noted earlier, the heat produced acts as the source for a pressure wave which expands from the locally heated volume at the speed of sound, V_s. The differential equation that describes sound production is given by[10],

$$\nabla^2 P - (v_s^{-2}) \delta^2 P / \delta t^2 = -\{(\gamma-1)/v_s^2\} \delta H / \delta t \tag{8}$$

where $\gamma=C_p/C_v$ is the ratio of the constant pressure heat capacity to the constant volume heat capacity. Equation (8) ignores acoustic losses. These losses can be added as perturbations (see Section 1.2.3). The plane cylindrical wave solution to the homogeneous part of Equation (8) ($\delta H/\delta t=0$) is

$$p(r) = \Sigma_{kmn} J_m(\alpha_{mn} r/R) \cos(k\pi z/L) \begin{Bmatrix} \sin(m\phi) \\ \cos(m\phi) \end{Bmatrix} \tag{9}$$

The choice of sin or cos is dependent on the positioning of the microphones and the excitation beam and our definition of axis coordinates.

The frequency at which a resonance occurs is given by

$$\omega_{kmn} = v_s \left[\left(\frac{\alpha_{mn}}{R} \right)^2 + \left(\frac{k\pi}{L} \right)^2 \right]^{1/2} \qquad (10a)$$

$$\nu_{kmn} = \frac{v_s}{2\pi} \left[\left(\frac{\alpha_{mn}}{R} \right)^2 + \left(\frac{k\pi}{L} \right)^2 \right]^{1/2} \qquad (10b)$$

Note that care must be taken when comparing nomenclature in different literature references. Some authors use the boundary condition $J'(\pi\alpha_{mn})=0$ at r=R and use tables for which $J'(\pi\alpha_{mn})=0$ at r=R and use tables for which α_{mn} is divided by π. Thus, their equation is written as,

$$\nu_{kmn} = \frac{v_s}{2} \left[\left(\frac{\alpha_{mn}}{R} \right)^2 + \left(\frac{k}{L} \right)^2 \right]^{1/2} \qquad (10c)$$

To determine the resonance frequencies, we shall use Equation (10b) and the tables in Reference 11. The ordering of the subscripts is not sacrosanct, it appears in all permutations in the literature.

A physical description of the resonance modes defined by Equation 9 provides guidance in determining microphone placement and mode intensity. The product of the r, ϕ, and z distributions

defines the pressure distribution for a specific kmn mode. Plots of the three functions and schematic pictures appear in Figure 1-1, (J_m); Figure 1-2, (cos $m\phi$) and Figure 1-3, (cos $k\pi z/L$). Figure 1-1 and Figure 1-2 are related because of value of m in cosmϕ specifies which Bessel function describes the radial dependence. Note that the cell walls must occur at minimum or maximum points of the J_m plots due to the vanishing of the acoustic velocity at the walls. These minimum and maximum points are numbered as to the value of n in the plots of Figure 1-1.

The azimuthal angle, ϕ, dependence is doubly degenerate for M>1 because either a cos or sin function satisfies Equation 8. However, the degeneracy disappears upon placement of the first microphone and choice of coordinate zero. Once this microphone is positioned the m solutions are restricted to cos terms since the pressure wave must be a maximum at the microphone and we define 0° to be in the vertical direction. The choice of mode and excitation beam position then determines optimum placement for any additional microphones. For example, a second microphone should be placed opposite the first when detecting the m=1 mode with on-axis excitation.

The generalized solution to the Equation 8 can be written as

$$P(r,\omega)=\Sigma_{kmn}A_{kmn}(\omega)\cdot P_{kmn}(r) \qquad (11)$$

where $A_{kmn}(\omega)$ are the mode amplitudes (related to intensity) and $P_{kmn}(r)$ describes the spatial distribution of the pressure wave. To insure that the mode amplitudes remain finite, loss terms, expressed as damping factors, are included as perturbation terms in Equation 8. When these losses are included, the mathematical form of the mode amplitudes is

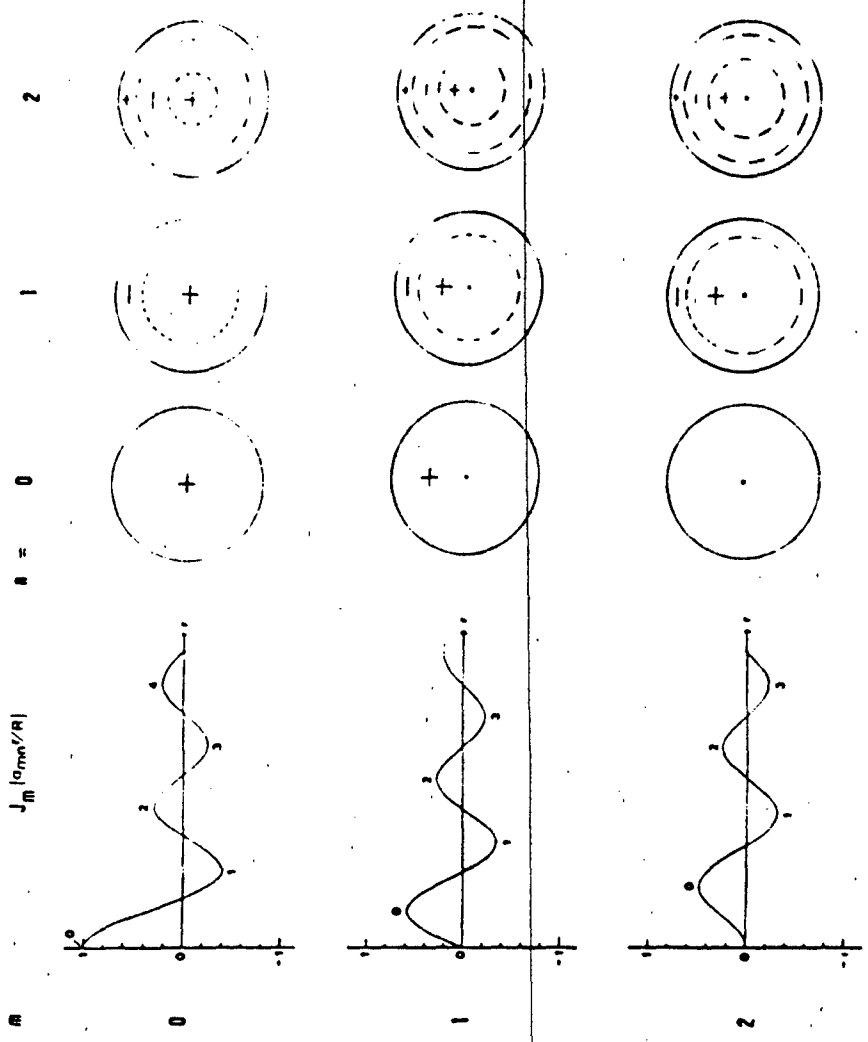

Figure 1-1. A pictorial representation of the radial variation of several standing pressure waves in a cylindrical cell. The standing wave amplitudes at any radial point (r) are proportional to a Bessel function evaluated at α_{mn} r/R when the value of R is set by the cylinder radius. α_{mn} is the n^{th} zero of the derivative of the Bessel function J_m. These zeros must occur at the cylinder wall. The value of r=R for the lowest four values of n is designated on each Bessel function plot. Note that for m 0 there exists a node along the cylinder axis. This is represented by a black dot. The complete standing wave amplitude pattern is given by the product of the radial (Figure 1-1), azimuthal (Figure 1-2), and longitudinal (Figure 1-3) descriptions.

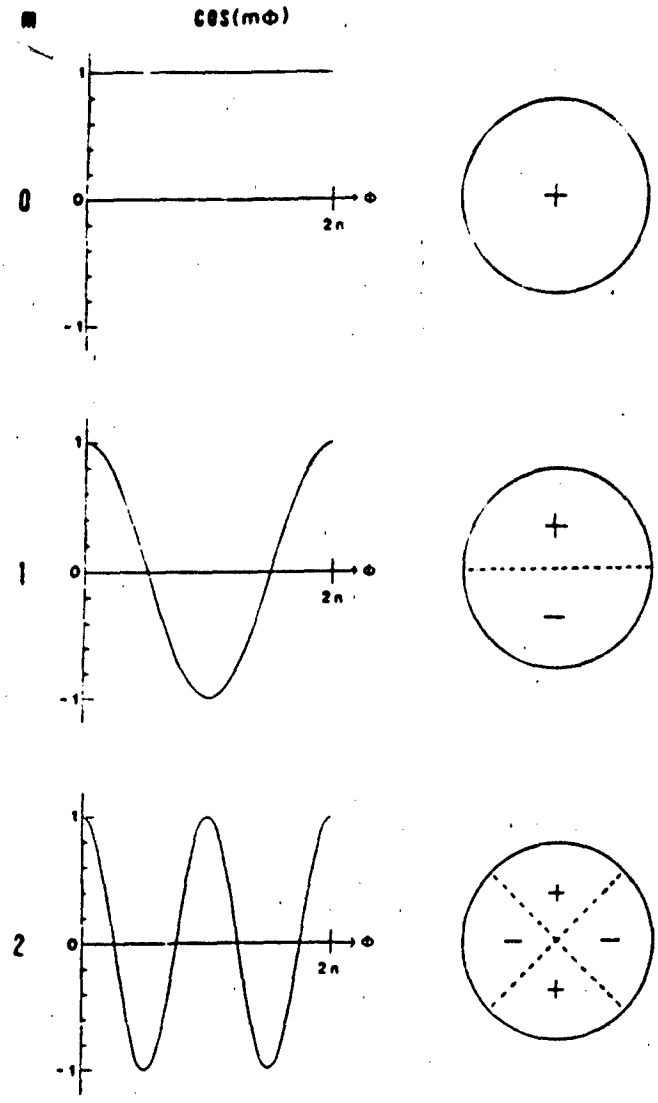

Figure 1-2. A pictorial representation of three azimuthal standing wave patterns. We have chosen the cosing function to represent our experiment and defined zero degrees as a vertical direction. Note that the azimuthal eigenvalue m determines which Bessel function J_m represents the radial distribution of standing wave amplitudes depicted in Figure 1-1. The complete standing wave amplitude patter is given by the product of the radial (Figure 1-1), azimuthal (Figure 1-2), and longitudinal (Figure 1-3) descriptions.

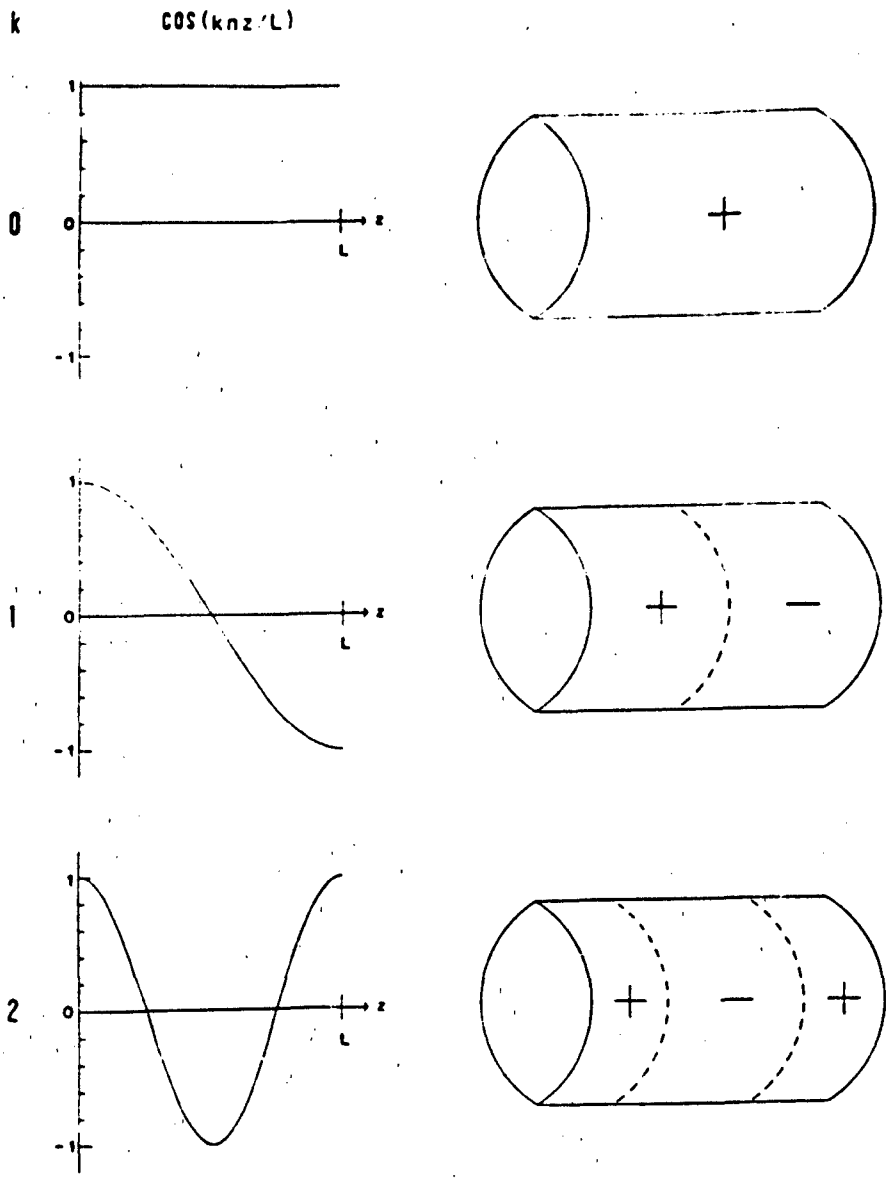

Figure 1-3. A pictorial representation of three longitudinal modes for k=0,1,2. For small absorptions most of the acoustic energy is deposited into the k=0 mode. The complete standing wave amplitude pattern is given by the product of the radial (Figure 1-1), azimuthal (Figure 1-2), and longitudinal (Figure 1-3) descriptions.

$$A_{kmn}(\omega) = \frac{-i\omega(\gamma-1)\int p_{kmn} H \, dr}{(\omega_{kmn})^2 V\{-1(\omega/\omega_{kmn})^2-(i\omega/\omega_{kmn}Q_{lmn})\}} \qquad (12)$$

where Q_{kmn} represents the sum of the losses. Losses due to viscosity, thermal conductivity, cell material, wall roughness, etc., determine the magnitude of Q. These losses are discussed further in Section 1.2.3.

We see from Equation (12) that setting k=0 and $\omega=\omega_{kmn}$ gives A_{kmn} $1/(\omega V)$. From Equation (10b), ω 1/R and V R2. Overall A_{kmn} 1/R. Thus, the minimum cell radius provides the maximum mode amplitude (signal). However, other limitations include the frequency response and physical size of the microphone and the restriction that CW>5. For the case of NO-Argon at one atmosphere, we have already calculated a lower limit on the pulse width of 25μs which translates into a ceiling on the chopping frequency (50% duty cycle) of 20 kHz. Use of Equation (10b) sets a lower limit on R of 0.9 cm.

1.2.3 Losses

Energy dissipation from an acoustic wave is characterized as either from volumetric losses or as due to surface effects. Volumetric losses, which arise because the sound wave departs from equilibrium, include viscous and thermal dissipation and collisional relaxation. Viscous and thermal dissipation, known collectively as Stokes-Kirchoff losses[10], occur when the sound wave has a portion of its energy converted into dispersed heat (thermal lors) or a portion of its directed motion converted into random motion (viscous loss). Stokes-Kirchoff losses, Q_{SK}, are calculated from

$$Q_{SK}^{-1} = \frac{\omega}{\gamma P_0}\left(\frac{4}{3}\eta + (\gamma-1)\frac{\kappa}{C_p}\right) \qquad (13)$$

where PO is the total system pressure, n is the viscosity and κ is the thermal conductivity.

Relaxation losses occur because thermally excited molecules release their energy into vibrational or rotational excitation of a collision partner. Such a loss mechanism is frequency and pressure dependent, but can readily be calculated.[12,13] As long as one uses a monatomic buffer gas and high dilution (>10^3), collisional relaxation losses do not contribute to the volumetric loss term.

Surface effects usually dominate the loss terms. Wave scattering into random directions by surface imperfections, viscous and thermal dissipation at the walls, energy extraction by the microphone(s) and energy absorption due to wall compliance all contribute to surface effect losses. Theory is presently not available to calculate the degree of smoothness, ripple, planarity, etc., which chamber walls must have. However, based on optical principles, imperfections less than 1/10 the sound wavelength can be neglected. Since all other losses are calculable, scattering losses can be determined by comparing experimental and theoretical values of Q.

Viscous and thermal dissipation at the walls arises because the gas away from the walls behaves adiabatically, while the walls are isothermal. Losses occur across the boundary isothermal layer. The theory for the fractional loss per cycle has been developed for on-axis excitation in a cylindrical chamber. The result in terms of Q, is [14]

$$Q_{sur}^{-1} = \frac{1}{L}\, d_v + (\gamma-1) d_h (1+L/R) \qquad (14)$$

where d_v, the viscous boundary layer is given by $(2\eta/\rho_0 M\omega)^{1/2}$ d_h, the thermal boundary layer is given by $(2\kappa/\rho_0 MC_p\omega)^{1/2}$, ρ_0 is the density of the gas and M is the gram atomic weight of the gas.

Wall compliance or reflection losses are also readily calculable. They are a function of the wall stiffness, gas density and sound velocity.[10] However, for a rigid nonporous wall, reflecting at normal incidence, essentially no energy is absorbed by the wall.

The microphone(s) removes energy from the standing wave in both usable (signal) and non-usable (loss) form. Thus, a more sensitive microphone or greater numbers of microphones extract an ever increasing portion of the sound wave's energy. This decreases the Q factor which appears in Equation (12) which also decreases the mode amplitude (signal). At greater than 50% energy extraction, the summed energy output from the microphones begins to decline due to the non-usable losses each microphone introduces.

For trace amounts of NO mixed with a rare gas such as Argon or Xenon, Stokes-Kirchoff, surface scattering and boundary layer effects constitute the primary loss factors. Table 1-1 lists the parameters needed to calculate these losses. Substituting the appropriate values from Table 1-1 into equation (13) gives $1/Q^{sk} = 1.16\times10^{-5}$ and 4.72×10^{-6} for Argon and Xenon, respectively. Substitution into Equation (14) gives $1/Q_{sur} = 1.41\times10^{-3}$ an 7.32×10^{-4} for Argon and Xenon. Summing $1/Q_{sk}$ and $1/Q_{sur}$ for Argon and Xenon

TABLE 1-1

Buffer gas parameters necessary in the calculation of resonant acoustic wave losses as predicted by Equation 13 and Equation 14. The definitions of the various parameters appear in the text.

Parameter	Value[a]		Units
	Ar	Xe	
P_o (1 atm)	1.01×10^6		dyne cm^{-2}
	2.46×10^{19}		molecules cm^{-3}
M	6.64×10^{-23}	2.18×10^{-22}	g $molecule^{-1}$
ω_{001}	3.86×10^4	2.12×10^4	rad s^{-1}
η	2.27×10^{-4}	2.31×10^{-4}	g cm^{-1} K^{-1}
κ	1.63×10^3	5.15×10^2	erg cm^{-1} s^{-1} K^{-1}
Cp	5.2×10^6		erg g^{-1} K^{-1}
$L = 2 \cdot R$	R=3.175		cm

a Thermodynamic values are obtained from Reference 15.

yields Q=704 and 1360, respectively. These loss values will be compared with experimental values in Section 1.3.

1.2.4 Noise

Two classes of noise occur for signals being processed with phase sensitive detection; namely, coherent and incoherent noise. Coherent or in-phase noise appears at the detector input with a constant phase relationship to the signal. Incoherent or random noise appears at the detector input with varying phases. Since the detector cannot distinguish between coherent noise and signal, any in-phase noise (i.e. interfering signal) must be smaller than the minimum detectable signal. The most important feature of our experimental design is that it shifts the coherent noise away from the detection frequency by employing a double modulation technique. In single modulation schemes, heat deposited into the sample cell due to window absorption and absorption by species other than NO will occur in-phase with any NO absorption. When only Zeeman modulation of the NO resonant frequency is used, pickup induced in the microphone and its leads by the alternating magnetic field will appear in-phase. With double modulation, all these noise sources are shifted away from the detection frequency. Consequently, any sources of coherent noise at the detection frequency must be due to molecules that absorb the CO laser radiation and Zeeman modulate at the same rate as the NO.

There are many sources of incoherent noise. These sources include room pickup, Johnson noise, turbulence, Brownian motion, and 1/f noise. Minimizing turbulence and 1/f noise were considerations in selecting the size of the sample cell. A relatively small cell boosts the detection frequency into the kilohertz regime where the 1/f noise is small. Turbulence noise is kept

small at the higher frequencies by slowing the gas flow rate through the cell and locating the gas ports at positions where nodes occur in the acoustic standing wave.

Noise (pressure) from Brownian motion (thermal noise) P_T, can be calculated from [16]

$$PT(\text{torr}/\sqrt{\text{Hz}}) = [4\gamma P_0 k_B T Q/(v\omega)]^{1/2} \quad (15)$$

where k_B is Boltzmann's constant. For the cell used in our experiment, Q=410, P_0=700 torr, V=201cm^3, ω=6150 Hz and γ=5/3. P_T is calculated as 7.02 x 10-9 torr/$\sqrt{\text{Hz}}$ which provides 9.3 nV/$\sqrt{\text{Hz}}$ of thermal noise (V_T) from our microphone.

Johnson noise can be calculated from[17]

$$VJ = (4k_B T R_S \Delta f)^{1/2} \quad (16)$$

where R_S is the equivalent source resistance connected across the amplifier inputs. The Knowles microphones used in our experiments have a maximum output impedance of 2.5 kΩ. Therefore Johnson noise contributes 21nV/$\sqrt{\text{Hz}}$, a factor two greater than the thermal noise.

The final noise sources to be considered are pickup of acoustic noise and electromagnetic (e/m) noise from the room. Isolation of the cell from mechanical vibrations is accomplished by using alternate layers of stiff, dense material and soft, flexible material and by vibration isolation tables. Acoustic isolation is achieved by employing layers of lead and foam and surrounding the cell with a vacuum chamber. Electromagnetic noise is reduced

through careful but straightforward shielding techniques. Experience with phase sensitive detection indicates that signals can be detected at signal to incoherent noise ratios (S/N) of 1/100.

1.3.0 EXPERIMENTAL

Optoacoustic sensing of NO at the parts-per-trillion (ppt) level represents a need for sensitivity improvement of two orders of magnitude relative to the present state-of-the-art limit. This level of improvement requires that the detector be optimized with respect to all parameters that can either increase signal or decrease noise. For the present phase of the work, a number of the parameters that influence signal and/or noise were investigated using two different experimental setups. The parameters investigated with each apparatus are listed in Table 1-2. The two setups allow independent examination and optimization of the sample cell design and the gas composition and noise sources.

1.3.1 Cell Design

Figure 1-4 depicts the experimental apparatus used to examine the first five items listed in Table 1-2. The laser employed is a continuous wave CO_2 laser capable of being line tuned with a diffraction grating throughout the 9.5μm band (00°2)-(02°0) P branch. We chose the P(16) line at 9.52 μm because it provides the highest output power. The laser beam is mechanically chopped in a frequency range between 5 Hz and 17 KHz. The optoacoustic cells are Plexiglas cylinders (0.64 cm thick) with 2.54 cm thick Plexiglas end plates. Sodium chloride windows are mounted into the end plates such that the inner surface of the window is flush with the inner surface of the Plexiglas end plate. Thus, only a small annular grove around the window can cause acoustic wave scattering losses. The microphone(s) is mounted as flush as possible with the cylinder wall. Since the microphone surface is flat, even

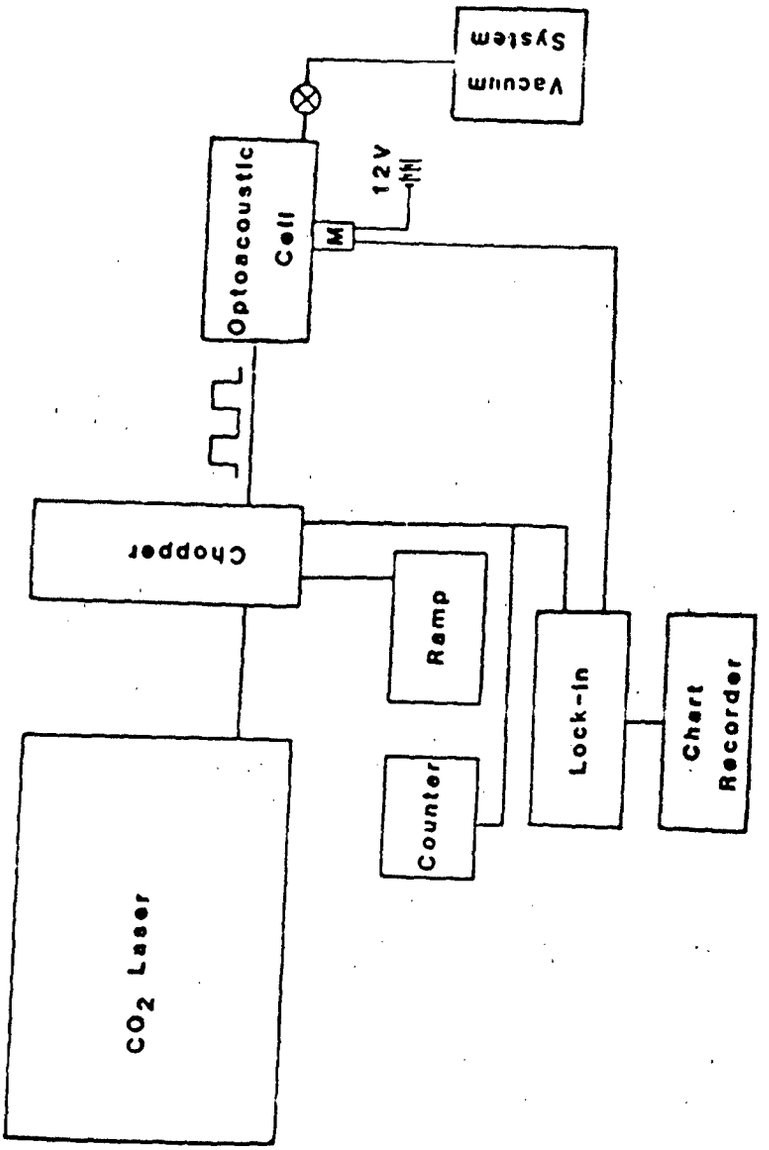

Figure 1-4. A schematic diagram of the apparatus used to measure cell design characteristics. The equipment consists of a continuous wave CO_2 laser which is grating tunable, a mechanical chopper operating between 5Hz and 17kHz, a plexiglas optoacoustic cell with a Knowles CA-1832 microphone flush mounted in the cell wall and signal processing electronics.

TABLE 1-2

Parameters Investigated with a Given Experimental Set-up

Cell Design
Cell Size
Surface Roughness
Mode Intensity
Excitation Position
Multiple Microphones
Gas Composition and Noise Sources
Total Gas Pressure
NO Partial Pressure
Buffer Gas Composition
Magnetic Field
Acoustic Isolation
Electromagnetic Field Isolation

0.64 cm diameter microphones protrude 1 to 2 mm beyond the cylindrical cell walls at microphone center. A small hole is left beside the microphone and the microphone cavity is sealed to allow for pressure equalization. The first microphone is placed at the midpoint of the cylinder's length. Additional microphones positions are dictated by the choice of excitation position and selection of the resonant acoustic mode. Knowles CA-1832 microphones are chosen because they are small in size, battery powered, have good sensitivity (1.32 mV/mTorr) and low noise. The output of the microphone is connected to a phase sensitive detector (Princeton Applied Research, Model 124) capable of band-pass filtering at Q_{PSD}=100 and with a maximum sensitivity of ~10nV. A function generator (Hewlett Packard 3010B) capable of ramp generation sweeps the mechanical chopping rate. The electrical output from the chopper is used as a reference for the phase sensitive detector system. With this apparatus, one atmosphere of neat SF_6 was employed. The low speed of sound in SF_6 allows the monitoring of the greatest number of acoustic resonances for a given cell size. The parameters investigated allow the signal to be maximized with respect to the various cell characteristics.

1.3.1.1 Cell Size

In resonant optoacoustic detection, the cell radius determines the modulation frequency as long as we work with radial and azimuthal modes. A minimum radius (R=0.9cm) is set by the collisional relaxation rate, C. The two main loss mechanisms exhibit frequency dependence: however, their effects are minimized for a given radius, L=2R. The other restriction on cell size derives from conservation of energy in the pressure wave. As it expands, the total energy remains constant. However, the surface area of the expanding cylindrical wave increases with R^2. This lowers the

energy density by a factor of R^{-2}, thus driving R toward its minimum value (maximum ω). Eventually the cell becomes so small that energy is lost from the standing wave by scattering from the microphone surface as that surface becomes a major perturbation to the cell wall.

Experimentally we monitor the intensity of the 001 and 002 modes for cells of various lengths having radii of 9.52, 6.98, 3.81, and 3.17 cm. Varying L at fixed R results in 10-20% signal losses for 60% changes in L away from the L=2R signal maximum. Each decrease in R for L=2R results in an ~15% increase in signal except that the 3.81 and 3.17 cm radius cells showed no change in signal.

1.3.1.2 Surface Roughness

Since the detection scheme relies on a modulated magnetic field, the cell materials are restricted to non-magnetic and non-conductive ones. This limits the choice of materials to glass, ceramic, or plastic. We test the effects of surface roughness on signal strength using Plexiglas cells which are easy to machine and bond.

In one experiment a coil of nichrome wire was inserted into the cell and allowed to expand until it pressed firmly against the cell walls. The sound wavelength is 6 cm. The wire diameter is 0.4 mm and the spacing between loops is 7 mm. Under these conditions we observed a maximum 10% decrease in signal. With the sound-wavelength to roughness-width ratio of 150, minimal signal loss is expected. Later measurements bear out these results. The close correspondence between the measured loss in the original

cell (Q=685) and the predicted value (Q=704) indicates that "off-the-shelf" surface preparation is adequate for Plexiglas cells.

1.3.1.3. Mode Intensity

The mode amplitude predicted by Equation (12) has an inverse frequency dependence; thus, the 010 or 001 mode should provide the largest signals. We have experimentally verified the strengths of the various modes. Figure 1-5 shows the signal strength measured as the frequency of the chopper is varied from 700 Hz to 7 kHz. The strongest modes are the OOn modes followed by the Oln modes. The modes are identified by comparing the measured frequencies with those calculated using Equation (10b).

The intensity difference between the OOn progression and the Oln progression can be understood by referring to the Bessel function plots in Figure 1-1. The overlap integral can be pictured as the product of a thin vertical rectangle, the laser beam, and the appropriate Bessel function. When the laser beam coincides with the cell's longitudinal axis it can be pictured as surrounding the r=O region of these plots. Clearly the overlap with JO is nearly 100% while the overlap with J1 is nearly zero.

The two small peaks at 729 and 1336 Hz arise from the square wave beam modulation employed. The Fourier component of the chopper frequency at 3ω excites the acoustic resonances at 2189 and 4010 respectively. The fact that the intensity ratio is not the expected 3:1 gives some feeling for the degree to which our excitation function deviates from being a square wave.

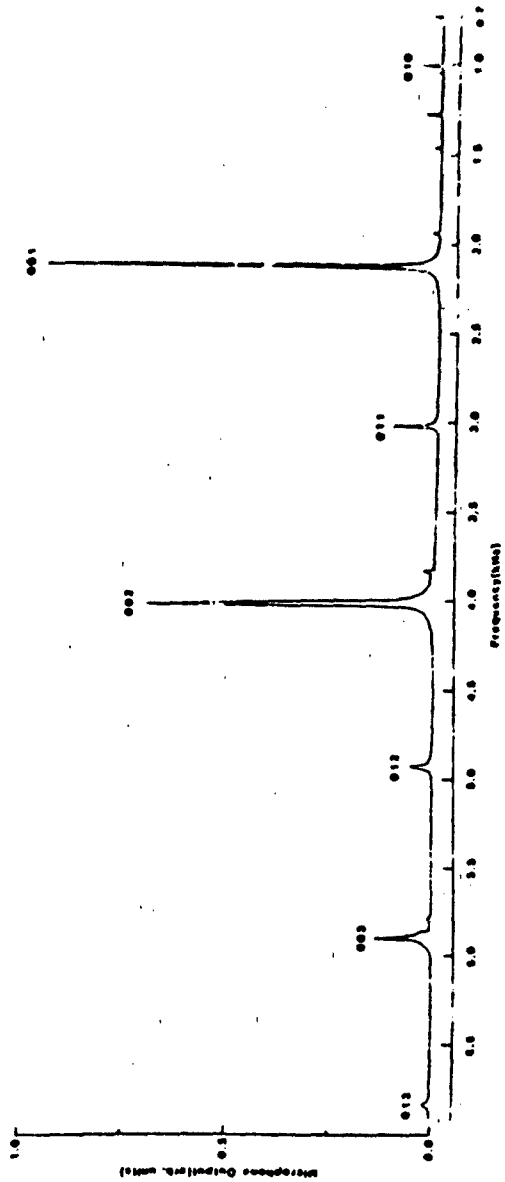

Figure 1-5. Acoustic resonant mode structure measured with cn-axis excitation. The cell is a cylinder 7.62cm long and 7.62cm i.d. Experimental conditions are 700 torr of neat SF_6 irradiated at 9.52μm with 2W of laser power. The vertical scale is the same as in Figure 1-6.

1.3.1.4 Excitation Position

The overlap integral, $\int P_{kmn}{}^{H}\, dr$, determines the coupling of the heat input into the standing wave. From the pictorial description of the radial portion of the standing wave (Figure 1-1), we see that on-axis excitation couples mainly with m=0 modes. At least 60% of the input energy cannot be transferred to the microphone since $|J_0(0)|=1.0$ while $|J_0(3.83)|=0.4$. As an alternative, one might try coupling to the m=1 modes by passing the laser beam along one cell wall and listening at the opposite wall. In this case, the heat coupling is decreased from $|J_0(0)|=1.0$ to $|J_1(1.8)|=0.6$. However, the pressure at the microphone is also given by $|J_1(1.8)|=0.6$. The result of an on- axis excitation appears in Figure 1-5. Contrast that spectrum with the opposite wall excitation spectrum given in Figure 1-6. Notice that the mode strengths change dramatically. The most intense mode in the on-axis excitation is 001 while the off axis excitation deposits the most energy into 010. Comparison of the strengths shows that the 001 mode provides ~10% more signal than its 010 counterpart.

1.3.1.5 Multiple Microphones

Maximum sensitivity coincides with the optimum energy extracted from the standing wave by the microphone(s). This goal can be achieved by two methods; namely, increased microphone sensitivity or increased number of microphones. In the case of resonant optoacoustic detection, there is a limit to the amount of energy which can be usefully be removed.

More sensitive microphones tend to have larger diaphragms which extract more energy because of the larger area. However, the noise pickup also increases. Employing several less sensitive

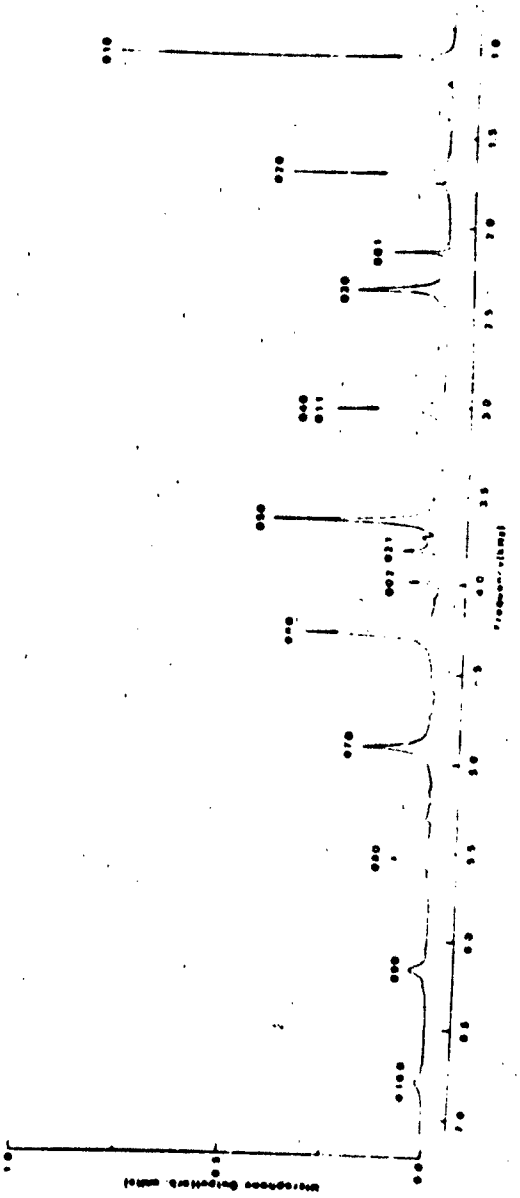

Figure 1-6. Acoustic resonant mode structure measured with excitation along the wall opposite to the microphone. The cell and experimental conditions are identical to Figure 1-5. The vertical scale is also the same as in Figure 1-5.

microphones can produce total signal levels equivalent to the more sensitive microphone while reducing the noise by the square root of the number of microphones. Working with a small diameter cell, less pressure wave scattering is expected with the smaller area microphones because they better approximate the arc of the cell wall.

A prototype cell was tested by monitoring Q as 1 to 4 microphones were embedded into the cell walls. The results of measuring Q as a function of the number of microphones is plotted in Figure 1-7. Each microphone introduces a loss of ~9% in Q. Optimum energy extraction at $Q_0/2$ corresponds to five microphones.

Q has also been measured using the apparatus described in Section 1.3.2 for a cell containing four microphones. The cell was charged with one atmosphere of Argon containing 9 ppm NO or one atmosphere of Xenon containing 1 ppm NO. The measured Q's were 410±40 and 790±80 respectively.

For a monatomic buffer gas, a plot such as Figure 1-7 can be extrapolated to zero microphones to yield Q_0. Q_0 can be compared with the Q calculated from Equations (13) and (14). The difference between Q_0 and Q represents the signal lost due to surface scattering when the cell has no microphones. A measurement of Q=410 for 4 microphones and a pressure of 1 atmosphere Argon extrapolates to Q_0=685. The calculated Q for Argon is 704. This implies that there is a 3% scattering loss. With Xenon/NO, Q_0 is 1320 while the calculated Q is 1360. This also represents a 3% scattering loss.

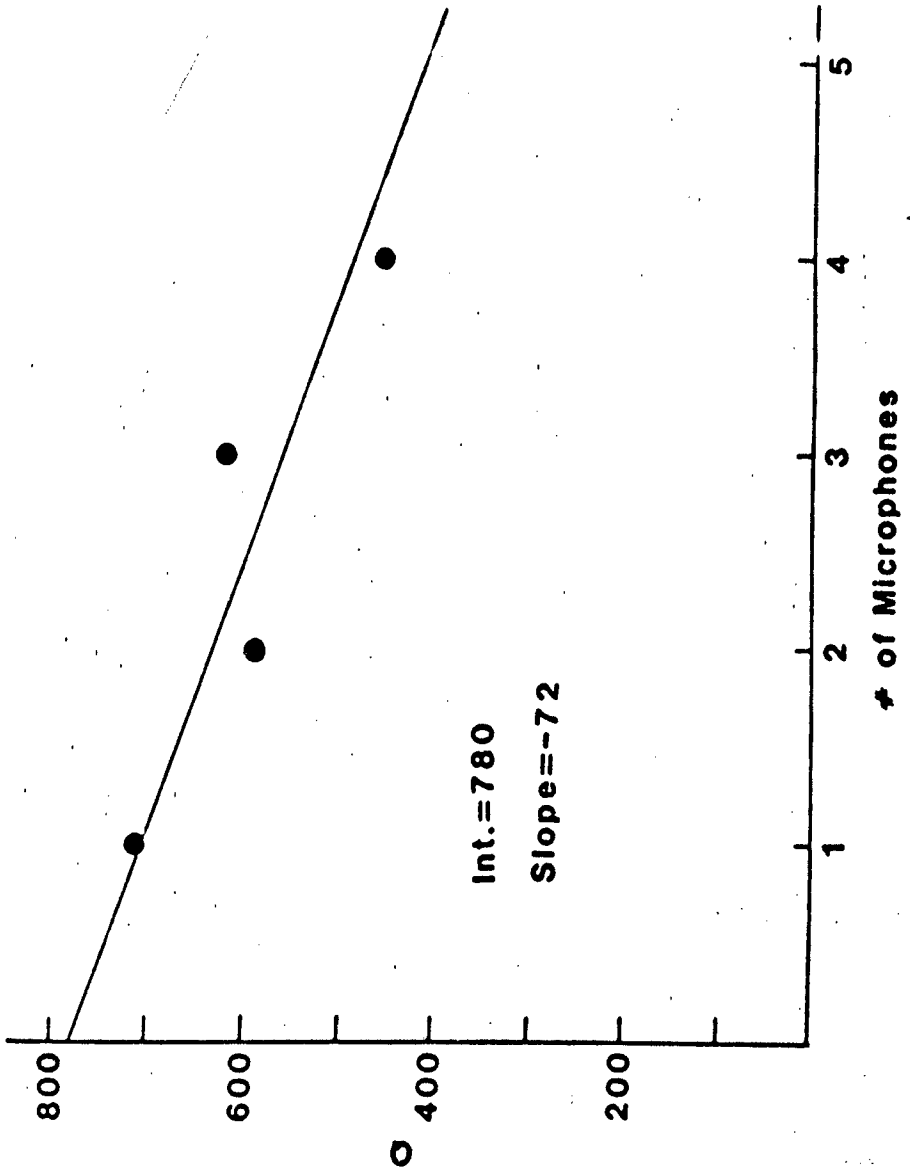

Figure 1-7. A plot of the acoustic gain factor Q versus number of microphones added to the cell. Optimum energy extraction occurs when one-half the energy is removed from the standing wave. For Q_o=Intercept the optimum extraction point $Q=Q_o/2$ in this plot falls near five microphones.

GEO-CENTERS, INC.

1.3.2 Gas Composition and Noise Sources

Figure 1-8 depicts the apparatus used to examine the remaining six items listed in Table 1-2. The laser used for these experiments is a continuous wave CO laser constructed to minimize both intensity and frequency fluctuations of the output beam. The laser is line tunable from 5.1 to 6.1μm. The best laser line for NO Zeeman shifting experiments lies at 5.307μm (P(13), v=9-->8). The maximum output power of this line is 1.5W. A pair of 15 cm focal length lenses, collimate the output beam. The chopper wheel located near the focus between the two lenses is positioned to insure complete blockage of the laser beam, since deviations from complete blockage reduce the signals from the optoacoustic cell. Two mirrors are used to direct the collimated laser beam to the cell and to provide steering capability for fine tuning the passage of the beam through the cell.

The optacoustic cell employed was a Plexiglas chamber 6.35 cm id. and 6.35 cm. long (cylinder length) with four microphones mounted at 0°, 90°, 180° and 270° halfway (3.17 cm) along the cell axis. The cell dimensions and microphone mounting positions were chosen based on the experiments described in Section 1.3.1. Compressed closed-cell foam holds the detector centered within a vacuum chamber. The vacuum jacket is wrapped with grounded carbon cloth which provides an electrical shield. The two chambers and the carbon cloth are located within the poles of a pair of Helmholtz coils capable of producing dc fields up to 1.3 kgauss which are slowly sweepable. The output from the microphones is fed into the same signal processing system as the one described in Section 1.3.1.

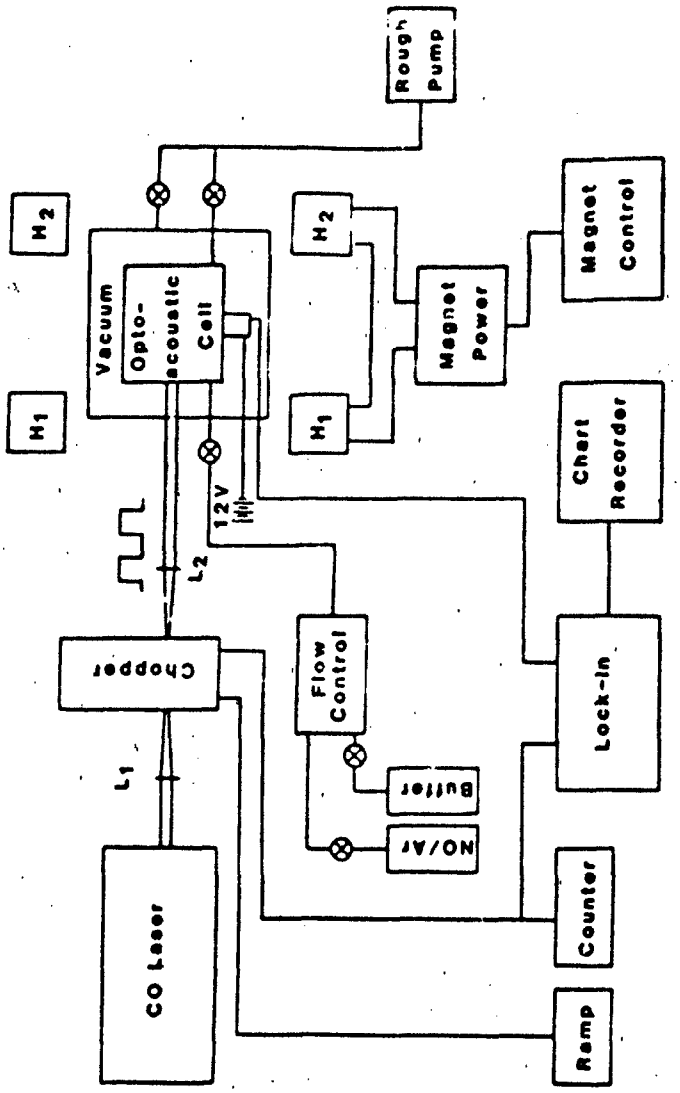

Figure 1-8. A schematic diagram of the apparatus used to measure various gas composition and noise sources. The laser is a cw CO laser operating at 5.307 m. The chopper, microphone and signal processing electronics are the same as in Figure 1-4. The optoacoustic cell is a plexiglas cylinder 6.35cm long and 6.35cm i.d. It is surrounded by a vacuum jacket for acoustic isolation purposes. The vacuum jacked is mounted inside a pair of Helmholtz coils, H_1 and H_2, which are energized by a power supply capable of producing 1.3 kgauss magnetic fields within the coils. The power supply is capable of slowly varying the magnetic field from 0-1.3 kgauss.

1.3.2.1 Total Gas Pressure

The total pressure is a major contribution to the collisional transfer of energy from the NO vibrational motion into translational motion of the buffer gas and the determination of the pressure wave amplitude via Q_{sur}. Minor contributions appear as small frequency shifts with pressure and in Q_{SK}.

Collisional changes cease to exist at Argon pressures exceeding approximately 200 torr. Similar predictions for Xenon are unavailable since the NO-Xenon relaxation rate is not known. Thus, the signal dependence versus total pressure at pressure greater than 200 torr is governed by the Q of the cell which is dominated by Q_{sur}. Combining Equation (14) and the fact that $_0 P_O$ leads us to conclude that there is a $(P_0/\omega)^{1/2}$ dependence on the signal.

Figure 1-9 summarizes the experimental results. For these experiments, 20 torr of a 10^{-3} NO/Argon mixture was admitted to the cell, and Argon added until a total pressure between 20 torr and 700 torr was achieved. Pressures between 120 torr $(P_0/\omega)^{1/2}$ = 0.14 and 700 torr $(P_0/\omega)^{1/2}$=0.335 display the expected square root dependence. At pressures less than 120 torr, an elbow occurs as incomplete collisional relaxation effects appear. Comparison of the observed slope with a calculated slope is not possible due to the presence of other factors (see Equation (12)).

1.3.2.2. NO Partial Pressure

Use of Equations (6) and (12) allows prediction of a linear relationship between the signal (mode amplitude) and the quantity of NO (via heat production) present in the system. We have found this relationship to be valid for NO/Argon mixtures ranging from

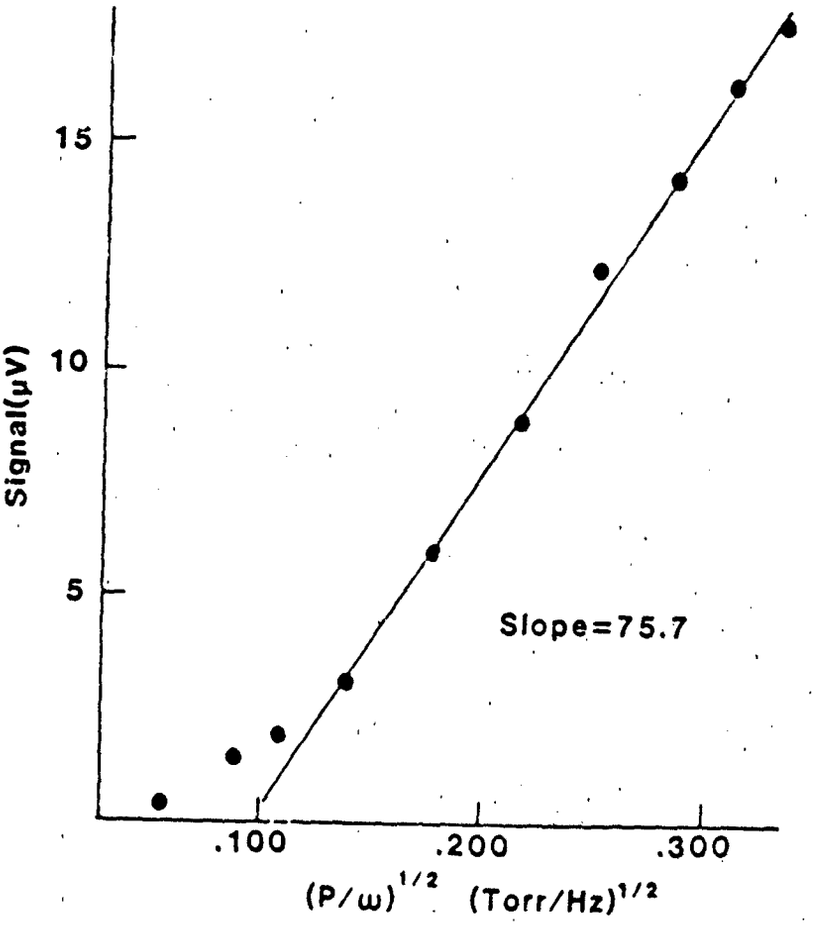

Figure 1-9. A plot of microphone signal versus total pressure using Ar as the buffer gas. 20 torr of a 10^{-3} NO/Ar mixture is admitted to the cell and Ar added to bring the total pressure to 20-700 torr. The elbow near .13 (~120 torr) arises from incomplete energy transfer as is explained in the text. Eqn 12 predicts a linear dependence of signal on the ratio $(P/\omega)^{1/2}$. Such a dependence is clearly observed at higher pressures.

1000 to 0.1 ppm NO. The lower limit occurs in the ppb range when the signal cannot be differentiated from the background noise in the test cell. At 1.4 ppm NO, 1 μvolt of signal is measured at a total pressure of 700 torr and a laser power of 600 mW.

Based on the 1 μvolt measured signal at 1.4 ppm and a linear extrapolation of signal with NO concentration, we predict a signal strength of one picovolt at 1.4 ppt NO. Presently, such a signal is undetectable. However, multipass optics should provide at least a signal increase of 10-20 times. Experiments indicate a signal increase of 40 times when Xenon replaces Argon as the buffer gas. Therefore, in an optimized multipass system we expect signals around 100-300 pV from 1 ppt NO/Xenon. This signal should be detectable with an optimized, low noise system. Thus, the anticipated detection limit of 1 ppt appears reasonable.

In our most recent and most sensitive experiments to date we have observed ~100 nV of signal from 5 ppb of NO in 700 torr of Xenon in a single pass system. The extrapolated signal based on this measurement of 20 pV at 1 ppt NO/Xe again agrees with the previous signal level expectations.

1.3.2.3 Buffer Gas

The initial choice of buffer gas was dictated by three constraints; namely the buffer gas must convert the maximum percentage of NO vibrational energy into translational motion, it must be non-absorbing and it must be readily available, relatively inexpensive, and non-toxic. Monatomic noble gases fulfill some or all of these constraints. Helium is an extremely inefficient collisional partner and has a very large sound velocity. Xenon is the most efficient collision partner but is more expensive than

Argon. On the basis of cost and performance, Argon appears to be the buffer gas of choice at the present time and has been used primarily in our present experiments. A search has started for a polyatomic collisional relaxer to increase the overall efficiency of the NO-Argon energy transfer. To date, a suitable candidate has not been found.

A series of experiments were performed to test the efficiency of Xenon as a collision partner. These results are given in Figure 1-10. In this series of experiments, 1.1 torr of a 10^{-3} NO/Argon mixture is introduced into the cell and Xenon added to bring the total pressure up to its measured value. This plot exhibits a shoulder at approximately 300 torr. We expect the shoulder to appear at pressures below the 120 torr limit for Argon. As yet we cannot explain the Xenon result. Note that ~3 times the signal amplitude is produced at 700 torr by approximately 1/13 the quantity of NO compared with NO/Argon at 700 torr (Figure 1-9).

1.3.2.4 Magnetic Field

The presence of an unpaired electron in the NO molecule accounts for the shift in energy (wavelength) when an external magnetic field is applied. The strength of the magnetic field determines the magnitude of the wavelength shift (Zeeman shift). Thus, sufficient displacement must exist between a CO laser line and an NO absorption line, to allow significant shift of the absorption line compared to its width by increasing the magnetic field strength. For our purposes, there must be sufficient magnetic field strength to shift the NO line into resonance with the CO laser line.

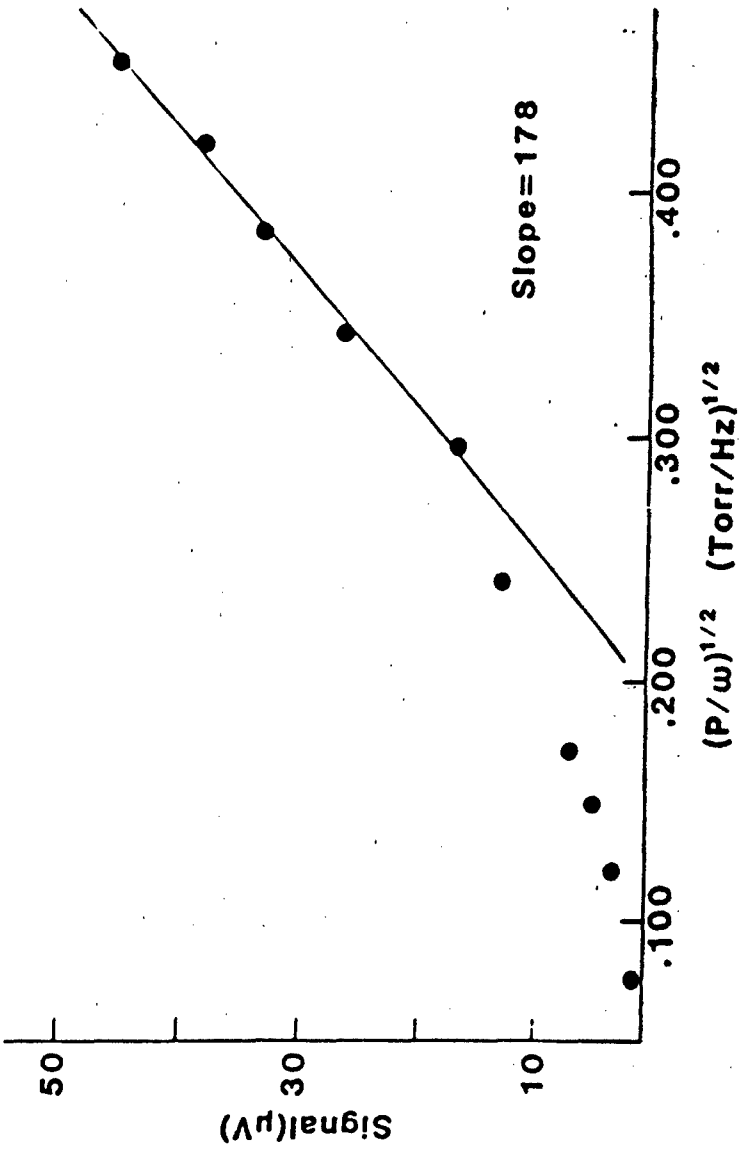

Figure 1-10. A plot of microphone signal versus total pressure when Xe is used as a buffer gas. 1.5 torr of a 10^{-3} NO/AR mixture is admitted to the cell and Xe added to bring the total pressure into the 20-700 torr range. The elbow occurs near .30 (~300 torr). We do not understand why the elbow occurs at such high pressure in this instance. The expected $(P/\omega)^{1/2}$ dependence is again seen at the highest pressures. Note that at 700 torr nearly 3 times the signal is seen for 1/13 the amount of NO present when Xenon replaces Argon as the buffer gas (see Figure 1-9 for the Ar results).

For the CO laser line P(13), 9-->8 and the NO $^2\Pi_{3/2}$ (1<--0) R(3/2) absorption line, the spacing is sufficient at pressures below ~50 torr to map two Zeeman line profiles for magnetic fields less than 1.3 kgauss. Figure 1-11 depicts the results of sweeping the magnetic field from 0 to ~1.3 kgauss with 20 torr of a 10^{-3} NO/Argon mixture in the cell. At a maximum field strength of 1.3 kgauss, two of the NO Zeeman components shift through the CO laser line. These two Zeeman transitions are the M_J = 1/2 <--3/2 line at ~ 620 gauss and the M_J = -1/2 <--1/2 line at 1.14 kgauss. These $\Delta MJ = \pm 1$ transitions are spectroscopically allowed for light polarized perpendicular to the magnetic field. Other possible M_J transitions for this NO-CO line pair are listed, along with their absorption strengths and field strengths, as determined by Kaldor et al.[18]

For pressures exceeding approximately 300 torr Argon, the NO line has broadened to the point that no magnetic field dependence can be seen at field strengths less than 1.3 kgauss. This results agrees with the pressure broadening parameter for NO/Argon, ΓAr ~0.065 $cm^{-1}atm^{-1}$, which leads to prediction of a line width of 0.025 cm^{-1} at 300 torr. The Zeeman tuning rate of the R(3/2) NO line is ~2.5 x 10^{-3} cm^{-1} $kgauss^{-1}$. Using the line width and tuning rate values, we deduce that a 10 kgauss field should enable us to Zeeman shift from the absorption maximum to almost zero absorption.

1.3.2.5 Acoustic Isolation

The prediction that 1 ppt NO in an atmosphere of Xenon produces ~200 pV of signal sets the acoustic isolation requirement at less than 20 nV broadband noise within the pass-band of our lock-in amplifier. However, we note from our present preliminary

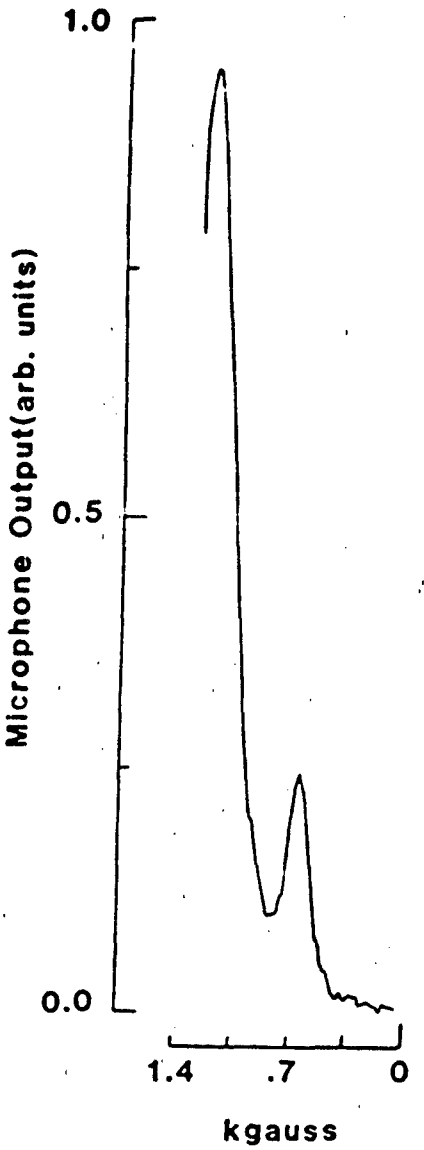

Figure 1-11. The magnetic field dependece of the NO $^2\Pi 3/2$, v=<--0, R(3/2) transition. In this experiment the magnetic field is swept from 0-1.3 kgauss with 20 torr of a 10^{-3} NO/Ar mixture in the cell. The peak near 620 gauss corresponds to the M_J=-1/2 <---M_J=3/2 Zeeman component while the peak near 1.1 kgauss corresponds to the M_J=-1/2 <-- M_J=1/2 Zeeman transition. Both transitions are allowed when the laser beam is polarized perpendicular to the magnetic field.

set-up for testing feasibility that acoustic noise voltages in the 50 μV range occur (0 to 50 kHz). Low frequency floor vibrations appear to dominate as our noise source (< 150 Hz). The large low frequency content means that only a small percentage of this noise should appear at kilohertz detection frequencies. Improved vibration isolation and reduced mechanical coupling between the optoacoustic cell and the walls of the vacuum jacket can be expected to reduce acoustic noise by at least two orders of magnitude.

1.3.2.6 Electromagnetic Field Isolation

Electromagnetic pickup must also be less than 20nV since the total noise from all sources (e.g. acoustic, electromagnetic, etc.). must be less than this value. In the present test apparatus (Figure 1-8), the total e/m noise is approximately 100 μV (0 to 50 KHz). Only a minimum amount of shielding and e/m filtering has been used. A two order of magnitude reduction in e/m noise can be accomplished by using triply shielded signal leads and 1 Hz low pass filters on the microphone power leads.

The expected reduction in both acoustic and e/m noise should be sufficient to reduce the noise pickup from the room to less than the 20 nV level required. The present total noise level of 150 #V reduces to 200 nV of noise within the 600 Hz band-pass we presently use. A reduction of the experimental band-pass to 6 Hz will decrease this value to 20 nV. A two orders-of-magnitude reduction in noise and a two orders-of-magnitude reduction in bandwidth should reduce the incoherent noise level to approximately 1 nV.

1.4.0 CONCLUSIONS

The influence of and interaction between components of an optoacoustic detection system for ultimately detecting explosives at the 1 ppt level have been examined from the theoretical and experimental system design aspect and feasibility experiments carried out. Particular attention has been paid to examining the behavior of the parameters that influence either signal or noise levels. Theoretical predictions relating signal levels to various parameters exhibit good agreement with experimental results. We conclude that 1 ppt detection of NO is achievable using only modest and straightforward extrapolation of the present experimental results.

Nitric oxide, the gaseous component to be detected, should be isolated in a buffer gas in a cell that takes advantage of signal gains derived from multiple pass optics and optoacoustic resonances. The detection system relies on careful acoustic and electromagnetic isolation (incoherent noise sources), and the ability to shift coherent noise sources away from the detection frequency. Double modulation, by a mechanically chopped laser beam and a Zeeman modulated NO absorption, provides the mechanism to accomplish such a shift.

Investigation of the individual parameters that influence signal and/or noise levels place design limits or restrictions on the components used for the measurements and detection. A cylindrical cell needs a radius between 2.5 and 3.7 cm (5.0 and 7.4 cm diameter) and the length of the cell should be equal to twice the radius. Additional machining of commercial plastics (e.g.

Plexiglas, etc.) to produce ultrasmooth inner walls is not necessary.

The largest signals arise at a frequency set by the lowest order radial-only acoustic resonance when on-axis excitation is used. Maximum signal extraction occurs when half of the energy in the acoustic standing wave is extracted by the microphone(s). With the Knowles CA-1832 microphones used in our experiments, this Q0/2 point is attained with 5 microphones.

Monatomic buffer gases are required and Xenon appears to represent the best collision partner for NO, supplying 40 times more signal than Argon. Signal enhancement using Argon/Xenon mixtures or other collisional relaxers for Argon needs further investigation. The dependence of signal on total pressure requires cell operation at or above atmospheric pressure. Collisional line broadening by the buffer gas at such pressures complicates the Zeeman modulation.

Further investigations would be necessary to isolate and eliminate/minimize both coherent and incoherent noise sources including acoustic and electromagnetic noise sources. Filtering and band-pass restrictions appear able to help achieve the low noise levels that are necessary for successful detection of the signal levels present at 1 ppt.

References

1. "Proceedings of the New Concepts Symposium and Workshop on Detection and Identification of Explosives Held at Reston, Virginia on October 30, 31, and November 1, 1978," Aerospace Corp., Washington, DC, sponsored by the U.S. Departments of Treasury, Energy, Justice and Transportation.

2. J. Hobbs, "Explosive Vapor Detection Summary", FAA Aviation Security R&D Workshop, April 18-19, 1983, U.S. Dept. of Transportation, Transportation Systems Center, Cambridge, MA 02142.

3. F.H. Jarke, S.M. Gordon, "Explosives Vapors Characterization", Report No. DOT/FAA/CT-82/65, IIT Research Institute, Chicago, Illinois, 1982.

4. D.L. Hartley and R.A. Hall, J. Appl. Phys. 43 (1972) 4134.

5. J.U. White, J. Opt. Soc. Am. 32 (1942) 285.

6. J.U. White, J. Opt. Soc. Am. 41 (1951) 732.

7. J.U. White, N.L. Alpert, and A.G. DeBell, J. Opt. Soc. Am. 45 (1955) 154.

8. H.J. Bernstein and G. Herzberg, J. Chem. Phys. 16 (1948) 30.

9. H.O. Kneser, H.J. Bauer, and H. Kosche, J. Acoustic. Soc. Am. 41 (1967) 1029.

10. P.M. Morse and K.V. Ingard, "Theoretical Acoustics", (McGraw-Hill, New York 1968).

11. M. Abramowitz and I.A. Stegun, "Handbook of Mathematical Functions", NBS Applied Mathematics Series 55, 1964.

12. R.H. Johnson, R. Gerlach, L.J. Thomas III, and N.M. Amer, Appl. Opt. 21 (1982) 81.

13. A. Karbach, J. Roper, and P. Hess, Chem. Phy#. 82 (1983) 427.

14. R.D. Kamm, J. Appl. Phys. 47 (1976) 3550.

15. J.O. Hirschfelder, C.F. Curtiss, and R.B. Bird, "Molecular Theory of Gases and Liquids", (Wiley, New York, 1954).

16. L.B. Kreuzer in "Optoacoustic Spectroscopy and Detection", Y.H. Pao ed., (Academic Press, New York, 1977).

17. H.V. Malmstadt, C.G. Enke, S.R. Crouch, and G. Horlik, "Optimization of Electronic Measurements" Module 4, (W.A. Benjamin, Inc., Menlo Park, California, 1974).

18. A. Kaldor, W.B. Olson, and A.G. Maki, Science 176 (1972) 508.

19. B.P. Lathi, "Signals, Systems, and Communications", (John Wiley and Sons, New York, 1965).

20. L.L. Abels and J.H. Shaw, J. Mol. Spec. 20 (1966) 11.

21. J.I. Steinfeld, "Molecules and Radiation", (Harper and Row, New York, 1974).

22. D.A. McQuarrie, "Statistical Thermodynamics" (Harper and Row, New York, 1973).

23. G.D.T. Tejwani, B.M. Golden, and E.S. Yeung, J. Chem. Phys. 65 (1976) 5110.

SECTION 2

SURFACE TOWED ORDNANCE LOCATOR SYSTEM

TABLE OF CONTENTS

TABLE OF CONTENTS (cont.)

GEO-CENTERS, INC.

LIST OF FIGURES

LIST OF TABLES

GEO-CENTERS, INC.

2.1.0 INTRODUCTION

The overall goal of the Surface Towed Ordnance Locator System (STOLS) program is to detect, locate, and identify buried ordnance. STOLS technology is based on the science of magnetostatics. The main body of most ordnance is constructed of iron or steel, materials with high magnetic permeabilities. In the Earth's magnetic field, the ordnance acquires an induced magnetic moment, which from a distance resembles a magnetic dipole. The induced moment is the source of a magnetic field which, when added to the Earth's field, creates a magnetic anomaly in the vicinity of the object. It is this magnetic anomaly which is used for detection of buried ordnance.

The overall objective of STOLS is to detect and locate several categories of buried projectiles, shells and bombs. These range from small projectiles, such as the MK60 rocket propelled grenade and the MK80 mortar round, to medium sized shells like the 155 mm, and larger size bombs, of which the MK81 (250 pound) and MK82 (500 pound) are representative. The depth to which the classes of ordnance penetrate the ground varies according to the type of ordnance, and can range from fractions of a foot for the smaller sizes to 20-30 feet for the larger ones.

Previous investigations into state of the art technology for ordnance detection have concluded that magnetic and electromagnetic methods are the most effective for range clearance. Magnetic methods are favored over electromagnetic methods both because of fewer false alarms and better detection of deeply buried ordnance.

The current field technology utilizes a man-portable magnetometer with 1 gamma accuracy. Under ideal conditions, a trained operator can perform range clearance operations for a few hours at a time and can reliably detect magnetic anomalies of 20 gammas or more. Thus, for example, a trained operator can be expected to detect MK81 bombs buried up to 10 feet.

STOLS technology utilizes an array of multiple magnetometers linked to a mobile computer-based data acquisition system. When operational, STOLS will accomplish faster and more thorough range clearance than currently possible with trained personnel.

The goals of the effort reported here were: 1) to field test STOLS components and evaluate their performance, 2) to collect baseline data of actual ordnance items and catalog magnetic signatures, and 3) to develop data processing algorithms for ordnance detection and location.

This report starts with a description of magnetic models and sensors. The platform system is then described. The data acquisition system and data processing are discussed followed by a description of field experiments.

2.2.0 MAGNETIC MODELS

For the purpose of locating and identifying buried ordnance, it is important to know the magnetic properties of ordnance and the interaction with the Earth's magnetic field. Magnetic models serve to simulate magnetic field anomalies and can be used to predict the source of observed magnetic field anomalies. One model for STOLS calculates the induced dipole moment of a magnetically permeable, solid spheroid. A second model generates the magnetic field anomaly for a magnetic dipole with given location, strength and orientation.

2.2.1 Induced Moment of Spheroid

Magnetically, ordnance items are essentially hollow, spheroidal shells of iron or steel. The induced dipole moment of an item is a complex function of its composition, geometrical shape and orientation to the main magnetic field. While the exact modeling of an item is a formidable task in mathematical physics, simplifying assumptions modify the problem so that the solution is both practical and useful.

In our model the ordnance item is represented by a solid, magnetically permeable spheroid. The mass of the spheroid is given by the metallic mass of the item. The major and minor axes of the spheroid are proportional to the length and diameter of the item. The magnetic permeability is given a value typical for the item's composition. The Fortran computer program to calculate the induced moments is based on a mathematical analysis contained in Reference 1.

The model approximation appears valid for most classes of ordnance items. Section 2.7.3 discusses the field experiment to determine the magnitude of permanent moments associated with the large items.

2.2.2 Induced Magnetic Field Anomaly

A buried ferromagnetic object distorts the ambient magnetic field of the Earth. At the surface this distortion manifests itself as a localized magnetic field anomaly. The variations that comprise the anomaly are a function of the source dipole (its orientation and depth), and the Earth's magnetic field. When mapped on a plane and contoured, the anomalies assume shapes and sizes which are characteristic of the source.

Our model facilitates the rapid generation of magnetic anomaly maps over a specified area for these source dipole parameters: magnetic moment, inclination, azimuth, and depth; and these Earth magnetic field parameters: inclination and intensity. The mathematics of the model is presented in Appendix B. Comparisons of the anomalies measured in the Indian Head, Maryland, MTR field tests, described in Section 2.7.2 of this report, with anomalies given by the model show close agreement. An example is shown in Figure 2-1, which compares very favorably with the contour map of an anomaly measured at the MTR, given later in this report as Figure 2-12.

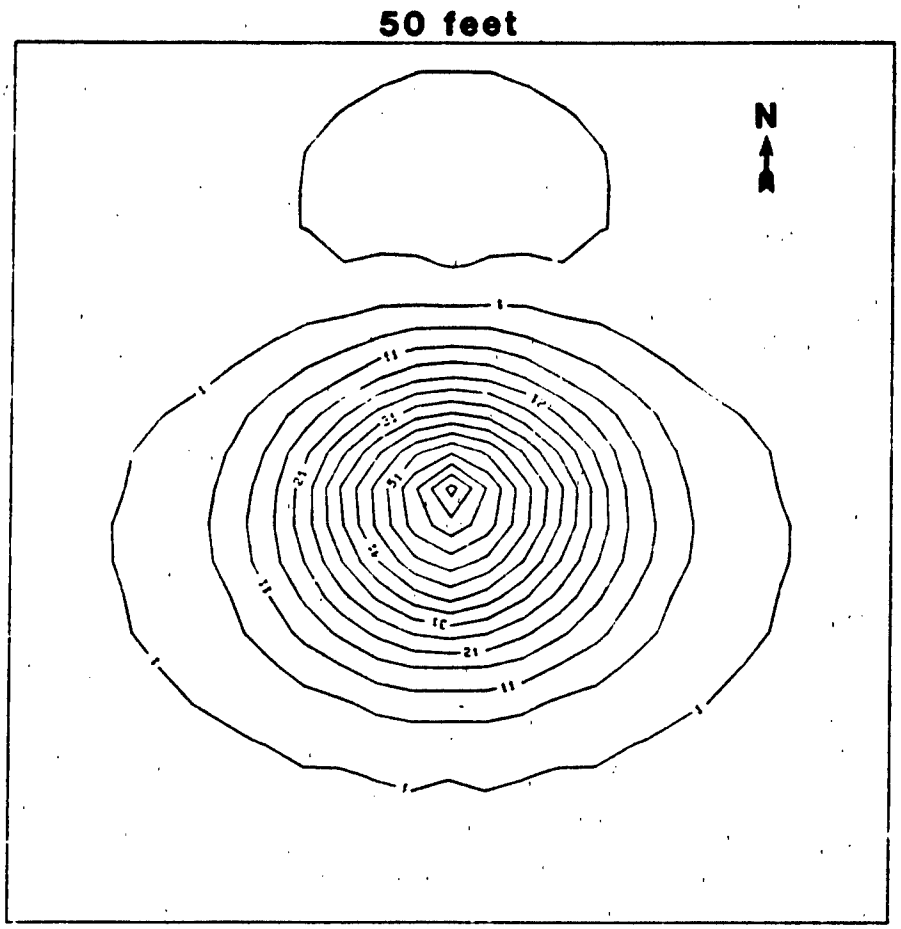

Model Fit to Item B2

Figure 2-i. Model magnetic anomaly.

GEO-CENTERS, INC.

Conclusion

The development of accurate models is important in order to achieve the overall goals of this program. The emphasis on location and recognition of buried ordnance requires a predictive capability which can be realized only through the use of computer models. Computer models developed under this program have been demonstrated to be useful tools for predicting the interaction of ordnance items with the Earth's magnetic field, and therefore have the potential for being successfully utilized for ordnance detection.

2.3.0 MAGNETIC SENSORS

Fundamentally, the sensors used with STOLS must make quantitative measurements of the Earth's magnetic field with spatial resolution sufficient to detect and identify anomalies due to buried ordnance. The measurements have to be sufficiently accurate for reliable computer analysis, and the number of measurements over an area has to be sufficient to guarantee full coverage. Since the number of measurements over an area depends on measurement rate and platform velocity, fast sensor readings allow for high platform velocity.

Many types of magnetic field sensors are available commercially, and others are at various stages of development. Of those available, it is necessary to select the sensor which best meets the program goals. The conclusions of an evaluation of sensor technology are presented along with conclusions of how these sensors are best utilized on the STOLS platform.

2.3.1 Evaluation

Magnetic field sensors are evaluated according to the following criteria, given in the order of precedence:

Accuracy:	+/- 1 gamma
Sensitivity:	+/- 1 gamma
Heading Error:	+/- 5 gamma
Measurement Rate:	>10 readings/second
Magnetic Self-signature:	nil
MTBF:	>1000 hours
Cost:	low
Power Consumption:	low

The sensor technologies include: fluxgate, proton precession, optical pumping, SQUID, thin film, Hall effect, and fiber optic. Thin film, Hall effect, and fiber optic technologies are currently in the research stage, but are considered for possible future incorporation into STOLS. Flexibility in the design of STOLS instrumentation makes it possible to utilize new technologies as they become available.

Based upon a full evaluation of available technology cesium vapor sensors are presently employed. These sensors have the required accuracy and sensitivity, exhibit low heading errors, provide continuous output, possess low magnetic self-signatures, and with proper handling operate without adjustment for long periods of time. However, the cesium vapor magnetometers lack the desired ruggedness and as such are not ideally suited to field use.

Fiber optic magnetometers have been identified as promising sensors for future use on the STOLS platform based on the demonstrated feasibility of a concept that promises to yield a fieldable fiber optic magnetometer. This fiber optic magnetometer experimentation has been done by GEO-CENTERS, INC. personnel in the Washington laboratories of NRL under another contract.

Since the lead time on many of the components needed for this development effort are long (6-8 months on some items), an effort to acquire the materials for the first phase of the magnetometer program was undertaken during this STOLS program. The long lead time items, sources, fiber optics, bulk optics, and feedback electronics have been purchased and are available for use in GEO-CENTERS Boston Laboratories. This will allow meaningful work

to be done on the fiber optic magnetometer within the first weeks of the start of development.

The current STOLS will be based on the cesium vapor sensor but will give background consideration to the potential use of a fiber optic magnetometer.

2.3.2 Configuration

The important factors for a sensor configuration are: minimum sensor spacing, number of sensors, layout, and mode of operation. The minimum sensor spacing is dictated by the spatial resolution needed to detect the smallest ordnance item. The number of sensors determines the size of the sweep area. The layout of the sensors may be horizontal or vertical, perpendicular to the direction of travel. The mode of operation can be one or a combination of single point, horizontal differential or vertical differential measurements. Computer simulations using the magnetic anomaly model have shown that a minimum sensor spacing of 0.5 meter is required to assure detection of shallow, small ordnance. Figure 2-2 compares simulated data from a linear array of 1.0 and 0.5 meter sensor spacing over a dipole moment equivalent to a 60 mm round. The larger spacing missed the central peak of the anomaly field. Investigation of various possible layouts and modes of operation of the array of sensors confirms that the simplest configuration, a horizontal linear array, satisfies all the requirements.

Conclusion

Comparison of the advantages and disadvantages offered by currently available magnetometers led to the selection of the

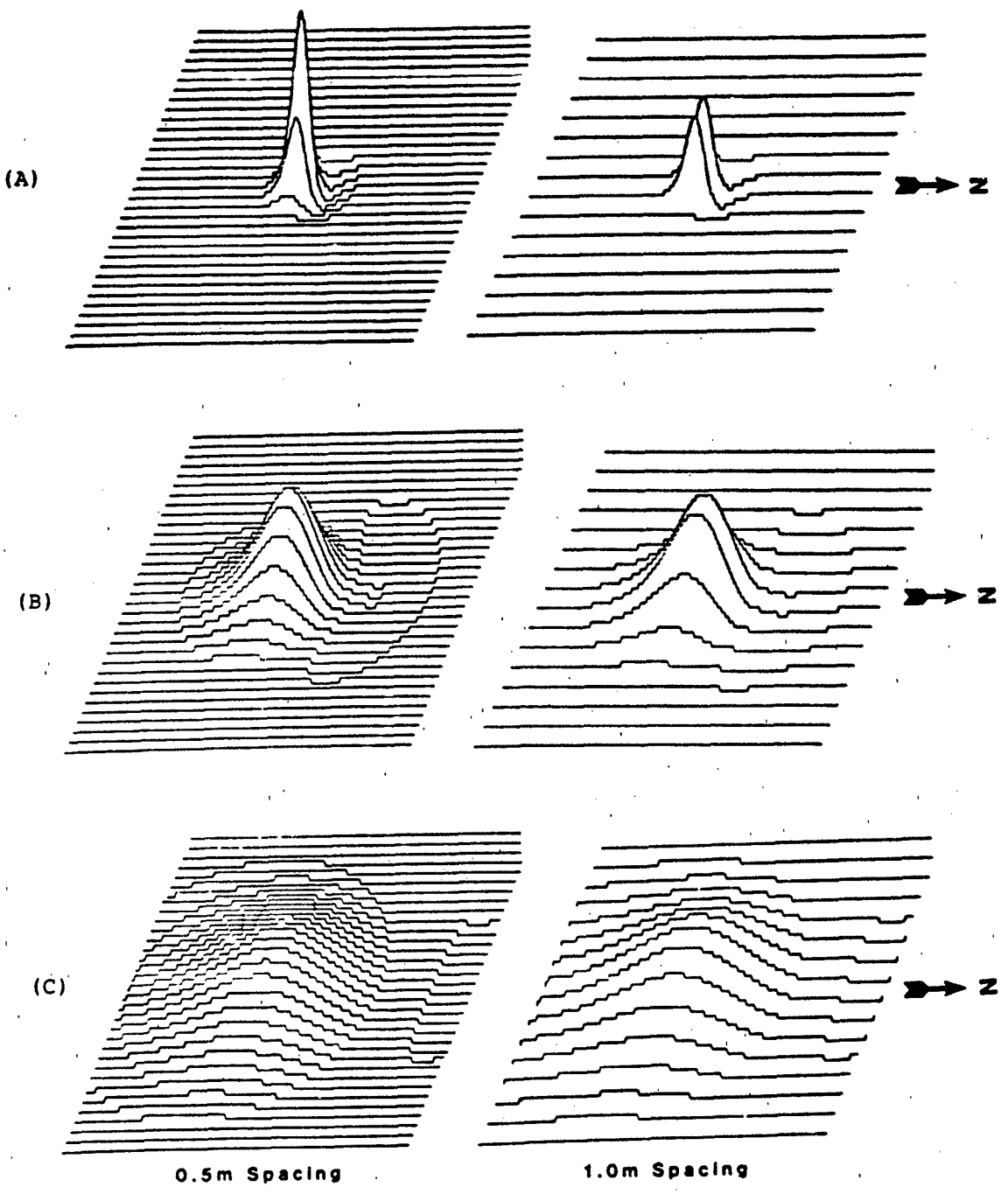

Figure 2-2. Effect of sensor spacing on measured magnetic anomalies. computer model simulation of 0.5 and 1.0 meter spacing over a 50 foot square area for:

A) Small dipole moment, shallow depth
B) Medium dipole moment, medium depth
C) Large dipole moment, deep depth

cesium vapor sensor for the current STOLS. Studies of possible sensor configurations concluded with the selection of the horizontal, equal spaced array with sensors 0.5 meter apart. Consequently, the present STOLS platform uses seven cesium vapor magnetometers spaced 0.5 meter apart on a three meter boom.

2.4.0 PLATFORM SYSTEM

The STOLS platform consists of a non-magnetic chassis supporting the boom of sensors, navigation system, and associated electronics. The platform will be towed over the surface by a motor vehicle during range clearance operations. The vehicle will carry the power system, front end electronics, telemetry, and computer data acquisition system.

The main topics covered in this section are: the evolution of platform design, the appraisal of candidate tow vehicles, and the evaluation of candidate navigation systems.

2.4.1 Platform

The platform designed for data acquisition at Fort Polk, LA was constructed entirely of wood. Frame members in this simple cart design were held together with dowels and glue. Five sensors were mounted one meter apart on a 12-foot long wood two-by-four. A track made up of five 4-foot by 8-foot plywood sheets guided the cart over the location of the ordnance items. Details of the test site and field methodology are contained in the April, 1986 Progress Report [2] and are summarized in Section 2.7.1 of this report. Figure 2-3 is a picture in the field of this platform, which served its limited purpose satisfactorily.

The Mark III platform uses the same four wheeled cart design of its predecessor, but is constructed of more advanced materials, primarily fiberglass and brass hardware. A three meter tiltable boom accepts seven sensor holders spaced 0.5 meter apart. A second boom supports the magnetometer sensor electronics. Pneu-

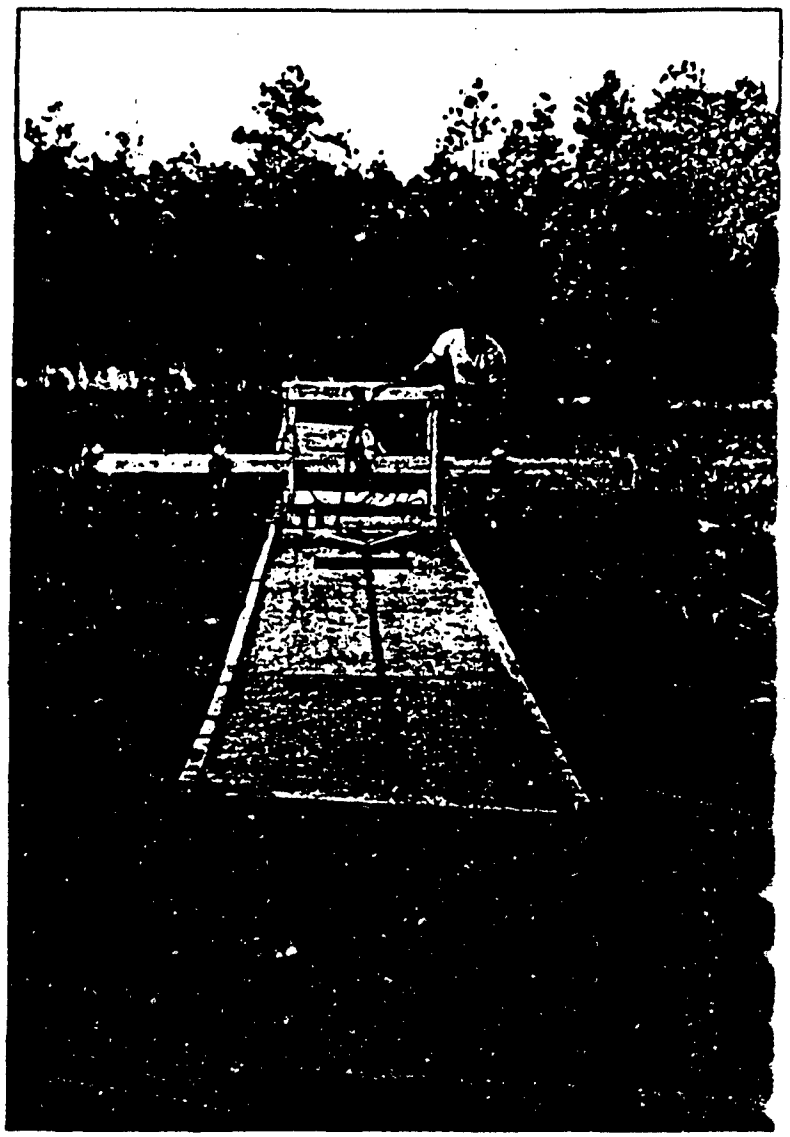

Figure 2-3. STOLS Platform used at Fort Polk.

matic tires allow unrestricted travel over range area. Disassembled, the platform fits into a 2 x 2 x 5 foot shipping crate. Figure 2-4 shows the platform in use.

This platform has been used successfully in the field to collect data at Indian Head, MD and Yuma, AZ. A detailed description of the field test at Indian Head, Maryland is contained in the Progress Report for May, 1986 [3]. A summary of these tests is presented in Section 2-7 of this report.

The STOLS design goals call for a non-magnetic, durable, stable, and portable platform. In the effort to meet these goals, the structural design and material composition of the STOLS platform undergo frequent assessments. Preliminary engineering drawings for a steerable, towed platform are reproduced in Figure 2-5. The proposed design adds a tow bar, shortens the wheel base and mounts a single boom off the rear end. While the design can re-use structural members from the existing platform, it is also amenable to alternative structural materials, such as stainless steel and aluminum.

Uneven terrain causes the platform to roll, deflecting the sensor boom from horizontal. This has the effect of changing sensor elevation. A simple method of compensating for this effect is to attach electronic sensors on the platform to detect tilt and transmit this data to the computer to calculate elevation corrections for individual sensors.

Two commercially available sensors that performs this measurement are the Sperry AccuStar Electronic Clinometer and the Watson Industries Inclinometer. These devices have a linear range of +/- 45 degrees in a total range of +/- 60 degrees. They

Figure 2-4. Mark III platform in use.

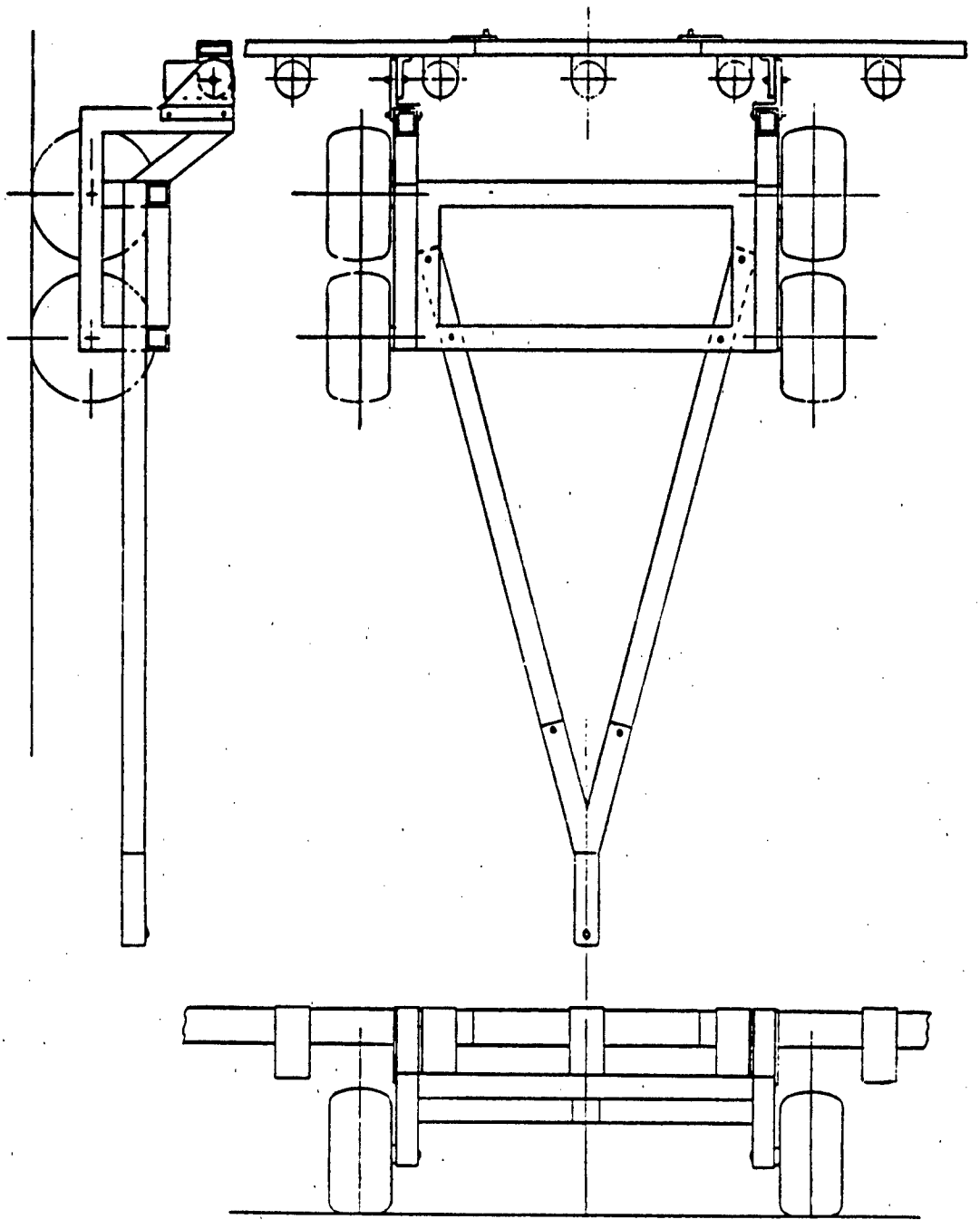

Figure 2-5. Preliminary drawing of Mark IV platform.

run off of a +/- 15 volt DC power supply, and either analog or digital outputs are available. These units will be further evaluated in tests of the towed platform.

A means of sensing forward motion is required, primarily to supply the data acquisition system with fiducial information, and secondarily to provide information on the instantaneous direction of travel. A limitation of the recommended navigation system is the position update rate. With the Racal system, a fix is obtained every 0.25 to 5 seconds. At a speed of 5 miles per hour, the platform travels approximately 7 feet per second. In the time between positional fixes, the platform may travel a significant distance (up to 35 feet) and change direction.

The present platform utilizes a tick marker operating on one wheel, which is satisfactory for straight line traverses. For unguided travel, two devices are identified which potentially satisfy this need: wheel shaft encoders and ultrasonic motion detectors.

A wheel shaft encoder outputs a discrete signal for an incremental rotation of the wheel shaft. A complete rotation results in a preset integral number of signals. The use of shaft encoders on opposing wheels yields data on the differential motion that results when the platform is turning. Suitable shaft encoders are widely available and will be procured as needed for platform testing.

Ultrasonic motion detectors rely on the doppler principle to determine the velocity of the platform relative to the ground. An ultrasonic transducer attached to the platform emits a wavetrain of fixed frequency, which reflects off the ground. Due to the

relative motion of the platform to the ground and the constant velocity of the sound wavetrain through the air, the frequency of the reflected wavetrain, as picked up by the transducer, is shifted an amount directly proportional to the velocity of the platform. Small devices of this type are commercially available, and will be procured as needed for testing.

Because the Mark II platform was confined to a wooden track, only straight line paths were possible. The Mark III platform avoids this limitation by rolling on four fixed pneumatic tires. Differential motion between the tires enables the platform to make wide angle turns. The design for the towed platform, as discussed above, will be capable of executing short radius turns.

2.4.2 Vehicle Magnetic Signatures

A prime consideration in the selection of a tow vehicle for the STOLS platform is the magnitude of its magnetic self-signature. This parameter defines the magnetic influence of the tow vehicle on the magnetic field sensors at the rear of the platform. Field tests have been conducted to determine the self-signatures of candidate tow vehicles. These tests examined the following vehicles: Jeep, HMMWV, CUCV, M113 APC, CUCV Pickup, Polaris ATV, Honda ATC, and the Buffalo Max II.

A magnetically clean test area for each vehicle prevented contamination of the data by ground clutter or environmental noise. Background surveys accounted for local gradients in the ambient field. The data include measurements of the vehicles at orientations of 0, 90, 180, and 270 degrees to magnetic north. These data were collected because the induced magnetic moment of a

structurally complex object, such as a motor vehicle, depends on orientation to the Earth's magnetic field.

Measurements were collected at fixed intervals from proton precession magnetometers, which have an accuracy of 0.1 gamma. Base station readings were subtracted from station readings to yield the total field anomaly. A detailed discussion of the field experiments is contained in the Progress Reports for July and November, 1985 [1,5].

The ranking of test vehicles according to the field measurements is given in Table 2-1. The magnetic self-signature of the Buffalo Max II is significantly less than the signatures of other vehicles tested that had similar terrain handling capabilities. The Buffalo Max II emerges as the principal candidate for the STOLS vehicle. It offers a minimum of magnetic interference and an ability to traverse difficult terrain. The remainder of the vehicles tested possess self-signatures of such magnitude that they can be utilized only with a very long tow bar (approximately 5 meters) or with elaborate schemes to correct for their magnetic influence.

The data supporting these conclusions are contained in the Technical Report GC-TR-536-003 [6].

2.4.3 Navigation

The Mark II platform traveled on a fixed 40-foot long track, and fiducial marks were recorded in the data at 13.25 inch intervals. A dent in one of the wooden wheels tripped a microswitch mounted on the axle support. A wheel on the Mark III platform has five equally spaced cams on the hub which trip a microswitch

TABLE 2-1

Radial distance (in feet) from the center of the test area to a point along the -5 gamma anomaly level directly behind and along the major axis of the vehicle. Distances were measured with each vehicle facing west, northwest, north, northeast, and east respectively.

Vehicle	W	NW	N	NE	E	Mean	Standard Deviation
CUCV	81	67	63	85	77	74.6	9.3
HMMWV	60	65	60	106	78	73.8	19.4
Jeep	39	34	47	75	77	54.4	20.3
M113	76	--	>80	--	>80	--	--
Polaris	13	16	11	22	23	17.0	5.3
Honda	25	22	40	27	--	28.5	7.4
Max II	29	--	28	--	35	30.7	3.8

mounted on the frame. Fiducial marks are recorded at approximately 10 inch intervals. This simple mechanism performs satisfactorily for straight traverses, such as those made at the Indian Head, MD and Yuma, AZ test sites. For non-linear travel paths a more sophisticated position marking system is required. Section 2.4.1.2 discusses motion detectors that satisfy this requirement.

A free-roving STOLS platform must incorporate a navigation system capable of locating the sensors in the search area with 1 meter accuracy. Applicable technology includes: inertial guidance, satellite positioning, laser rangefinding, and radio positioning. Inertial guidance creates difficult problems for onboard instrumentation, and is cost ineffective. Satellite positioning is accurate only to 5 meters for a moving platform, insufficient for STOLS. The two technologies with potential application are laser rangefinding and radio positioning. Progress Reports for March, 1986 [7] and June, 1986 [8] contain assessments of commercially available equipment based on field demonstration tests.

The Hydropac Positioning System is a laser tracking and ranging system manufactured by Geodimeter, Inc. The field demonstration performed at Indian Head, MD in April, 1985, confirmed its accuracy. However, the system is strictly line of sight with a limited vertical tracking angle. Its limited usefulness in areas of high topographical relief disqualifies this type of system for STOLS navigation.

Radio positioning systems are represented commercially by Motorola, Del Norte and Racal, described below. They all operate on the same principle of measuring the elapsed two-way travel time of a transmitted microwave signal from a master transmitter to remote repeaters. The differences between the systems are mainly

in the engineering and the degree of automation reached through the use of microprocessor technology.

The Motorola Mini Ranger III has been utilized by NAVEOD-TECHCEN on in-house projects. Because of its low accuracy (± 2 meters) this model is not the prime choice.

The Del Norte Trisponder Radio Location System was demonstrated by factory representatives at Indian Head, MD in March, 1986. The system performed satisfactorily. Details of the field test are covered in the Progress Report for March, 1986 [7].

The Racal Micro-Fix positioning system was field tested at a test site in Dover, MA in June, 1986. The system performed satisfactorily. Details of the field demonstration are contained in the July, 1986 Progress Report [9].

Of the units tested and inspected the Racal system offers superior performance. It provides the necessary accuracy combined with rugged engineering, advanced microprocessor control, automatic calibration, and interchangeable master and remote transceivers. Table 2-2 offers a summary of all the positioning systems evaluated.

Conclusion

The STOLS platform has evolved to meet overall program goals. With the addition of on-board navigation and linkage to a tow vehicle, the platform design will be finalized. Preliminary designs have been drafted for this platform.

Manufacturer	System	Technology	Positional Accuracy	Distance Range	Standard Frequency of Operation	Unit	Dimensions
RACAL Positioning Systems Limitted Surrey, England	Micro-Fix Microwave Positioning	microwave ranging (range/range)	± 1 meter line-of-sight	10 m - 5 km line-of-sight using 90610 or 90612 T/R units	5.0 GHz	90600 CMU 90601 T/R (w/omni ant) 90602 T/R (w/sector ant)	6.0"x14.7"x11.2", 14.6 lbs 10.2"x13.2"x8.3", 16.3 lbs 10.2"x13/2"x8.3", 16.3 lbs
Del Norte Technology, Inc. Euless, Texas (817)267-3541	TRISPONDER Radio-Location System	microwave ranging (range/range)	± 1 meter line-of-sight	10 m - 5 km line-of-sight using 261 MTR	9.4 GHz	542 DDMU 261 MTR (w/omni ant) 261 RTR (w sector ant)	7.0"x17.0"x15.3", 31.5 lbs 9.0"x4.5"x8.5", 8.5 lbs 14.0"x4.5"x8.5", 7.0 lbs
Motorola, Inc. Position Determining System Tempe, AZ (602)897-4115	MINI RANGER III Positioning System	high frequency radio waves (range/range)	± 2.0 meters line-of-sight	10 m - 27 km line-of-sight	5.4 GHz to 5.6 GHz	Range Console Control T/R Remote T/R	17.0"x18.0"x5.5", 31.0 lbs 6.0"x8.0"x12.0", 9.[illegible] lbs 6.0"x8.0"x12.0", 9.[illegible] lbs
Del Norte Technology, Inc. Euless, Texas (817)267-3541	UHF TRISPONDER Systems	UHF ranging (range/range)	± 2 meters line-of-sight accuracy beyond line-of-sight is dependent upon propagation characteristics	approximately 2-1 times line-of-sight distance	435 MHz	547 DDMU 435 T/R	7.0"x17.0"x15.3", 31.5 lbs 28.4"x6.0"x9.0", 25 lbs
Motorola, Inc. Position Determining System Tempe, AZ (602)897-4115	MINI RANGER Satellite Survey System	satellite Doppler positioning (GPS)	0.5 m to 1.5 m for 8 to 10 satellite passes in the translocation mode	unlimited	150 MHz and 400 MHz	Rec/Proc Antenna	13.8"x20.5"x9.5", 45 lbs 164" high, 27 lbs

TABLE 2-2. Comparison of Commercial Navigation Systems

Input Voltage	Power Consumption	Beamwidth Azimuth	Beamwidth Elevation	Positional Update Rate	Real Time Operation	Computer Interface	On Board Guidance	Comments	Cost
16 to 32 VDC powered via CMU	40 W	360°	20°	adjustable from 1/4 sec to 5 sec	yes	RS-232C, RS-422 IEEE-488 GPIB	standard	-CMU automatically selects best values each positional fix -MTR has low mag mig antennae circularly polarized	$66,000
16 to 30 VDC	12 W	90°	6°						
22 to 27 VDC powered via DDMU	45.6 W	360°	19°	adjustable from 1/4 sec to 5 sec	yes	RS-232C	standard	-DDMU automatically selects best range values for each positional fix	$55,806
12 to 15 VDC	5.4 W	110°	7°						
12 to 32 VDC powered via range console	57.0 W	360°	25°	adjustable from 1 sec to 10 sec	yes	RS-232C IEEE-488 GPIB	optional		$44,842
22 to 28 VDC	45.6 W	unknown		unknown	yes	RS-232C	standard		unknown
22 to 32 VDC	50 W peak								
10 to 16 VDC	7.0 W	---		2 minutes per satellite pass	no	RS-232C	not avail.	-compatible with JMR and Magnavox data tapes -requires line-of-sight contact with satellite	unknown

	Manufacturer	System	Technology	Positional Accuracy	Distance Range	Standard Frequency of Operation	Unit	Dimensions
GPS	JMR Instruments, Inc. Chatsworth, CA (213)882-2800	JMR4 Scaland Surveyor	satellite Doppler positioning (GPS)	± 2 meters for 5 to 50 satellite passes in translocation mode	---	150 MHz and 400 MHz	Rec/Proc Antenna	17.4"x10.5"x25.2", 57 lbs
GPS	Magnavox Marine Surveys Systems Division Torrance, CA (213)618-1200	MX4102	satellite Doppler positioning (GPS)	unknown	---	400 MHz	unknown	unknown
Laser Tracking	KRUPP ATLAS Elektronik Bremen Bremen, W. Germany	Atlas Polarfix Range/Azimuth Position Fixing System	laser tracking (range/azimuth)	± 0.1 to ±0.2 meter per 1000 meters of measured range	0-5 km line-of-sight	InfraRed	Sensing Head Control Unit Reflector Telemetry Ant Interface Unit	42 lbs 44 lbs 22 lbs 2 lbs 22 lbs
Laser Tracking	GEODIMETER, INC. Novato, CA	Hydropac Positioning System	laser tracking (range/azimuth)	± 10 to 20 mm in fast track mode	0.5 m - 5.5 km line-of-sight	InfraRed	140H Control Unit	9.1"x11"x13.8", 20.9 lbs
Laser Tracking	ODOM Hydrographic Systems, Inc. Baton Rouge, LA	AZTRAC Range/Azimuth Positioning System	directional theodolite	± 0.01° (36 arc sec)	26 m - 1 km	---	Control Unit Receiver Unit	15.8"x9.1"x15.8", 16 lbs 5.9"x19.7"x15.8", 20.5 lbs

	Input Voltage	Power Consumption	Beamwidth Azimuth	Beamwidth Elevation	Positional Update Rate	Real Time Operation	Computer Interface	On Board Guidance	Comments	Cost
GPS	12 VDC	12.0 W	---		Doppler Interval is 4.6 seconds	no	RS-232C	not avail.	-requires line-of-sight contact with satellite	unknown
GPS	unknown	unknown	---		unknown	no	RS-232C	not avail.	-requires line-of-sight contact with satellite	unknown
Laser Tracking	12 VDC	45 W	0.01°	0.23°	2.5 positional updates/second	no	RS-232C	no	-affected by fog + dust -tracks automatically -dead reckoning mode engaged when line-of-sight contact interupted -power supply not required at target	~ $90,000
Laser Tracking	12 VDC	12 W	0.14°	0.14°	4 positional updates/second	yes	RS-232C	no	-affected by fog + dust -tracks automatically -power supply not required at target -wide measuring beam	Big Time
Laser Tracking	12 VDC 24 VDC 12 VDC	12 W 10.5 W optional	---		transmits 10 angles per second via RF data link	yes	RS-232C	no	-used in conjunction with DM-80 -receiver + control unit on STOLS cart and data converter transmits range angles combined with range distances	$18,750 $256 for data converter

Misc. ---------- Inertial ---------- Laser Tracking

Manufacturer	System	Technology	Positional Accuracy	Distance Range	Standard Frequency of Operation	Unit	Dimensions
CUBIC Precision Tullahoma, TN	DM-80 Electronic Distance Module	laser distance measuring unit	± 5.0 mm	0-750 meters to single prism 0-1300 meters to triple prism	7.492 MHz	DM-80	3.5"x4.0"x7.1", 3.0 lbs
Litton Guidance and Control Systems Woodland Hills, CA	Auto Surveyor III Inertial Navigation System	inertial navigation	horrizontal error (RMS) 0.15 m + D/10,000 vertical error (RMS) 0.12 m + D/20,000 where D is transverse distance	unlimitted	---	---	25.8"x30.5"x19.5", 210 lbs
Sailcomp Industries, Inc. Middletown, RI	PCI01 Digital Compass	digital flux-gate compass	± 1.0 degree	unlimitted	---	---	4"-5" diameter 4" height 33 ounces

Input Voltage	Power Consumption	Beamwidth Azimuth	Beamwidth Elevation	Positional Update Rate	Real Time Operation	Computer Interface	On Board Guidance	Comments	Cost
Misc.----------Inertial----Laser Tracking									
7.2 VDC NiCad Battery	---	---		1 positional update/second	yes	RS-232C and HP-IL interface for HP-41 calculator	no	-requires operator at station -interfaces with theolites such as Lietz, Nicon, etc.	$2,950
24 VDC	---	---		---	yes	unknown	yes	-requires large magnetic unit on STOLS cart -can not be used within 15° latitudes of of poles	Big Time
12 VDC	---	---		---	yes	RS-232C	yes	-electronic sensor with no moving parts -square Hemholtz coil corrects for local magnetic field anomalies and declination of earth's magnetic field	$795 + $200 for coupler

2.5.0 DATA ACQUISITION SYSTEM

The data acquisition system controls the flow of information from the transducers on the STOLS platform to the STOLS computer system. The transducers include, but are not limited to: magnetic field sensors, motion and attitude sensors, positioning instruments, and diagnostic sensors. The data acquisition system is composed of hardware, in the form of the various sensor interfaces and the computer; and software, which controls, directs, and processes the stream of information originating at the sensors. A block diagram of the data acquisition system is shown in Figure 2-6.

This sections summarizes development work on computer systems, sensor interfaces, and software programs.

2.5.1 Computer Systems

The original breadboard computer system was used successfully to acquire data at the test site at Fort Polk, LA. It is described in the Progress Report of February, 1985 [10] and in Section 2.7 of this report. This system has since been converted to an image processor for analysis of STOLS data. A more powerful computer has since replaced the original for field data acquisition and storage.

The data acquisition system fielded at Fort Polk, LA was based on an IBM PC/XT, consisting of the computer, 360 KByte 5-1/4 floppy disk drive, 10 MByte hard disk, a monochrome monitor, and an Epson FX80 printer. The computer performed flawlessly in the field even during inclement weather. Precaution was taken to level

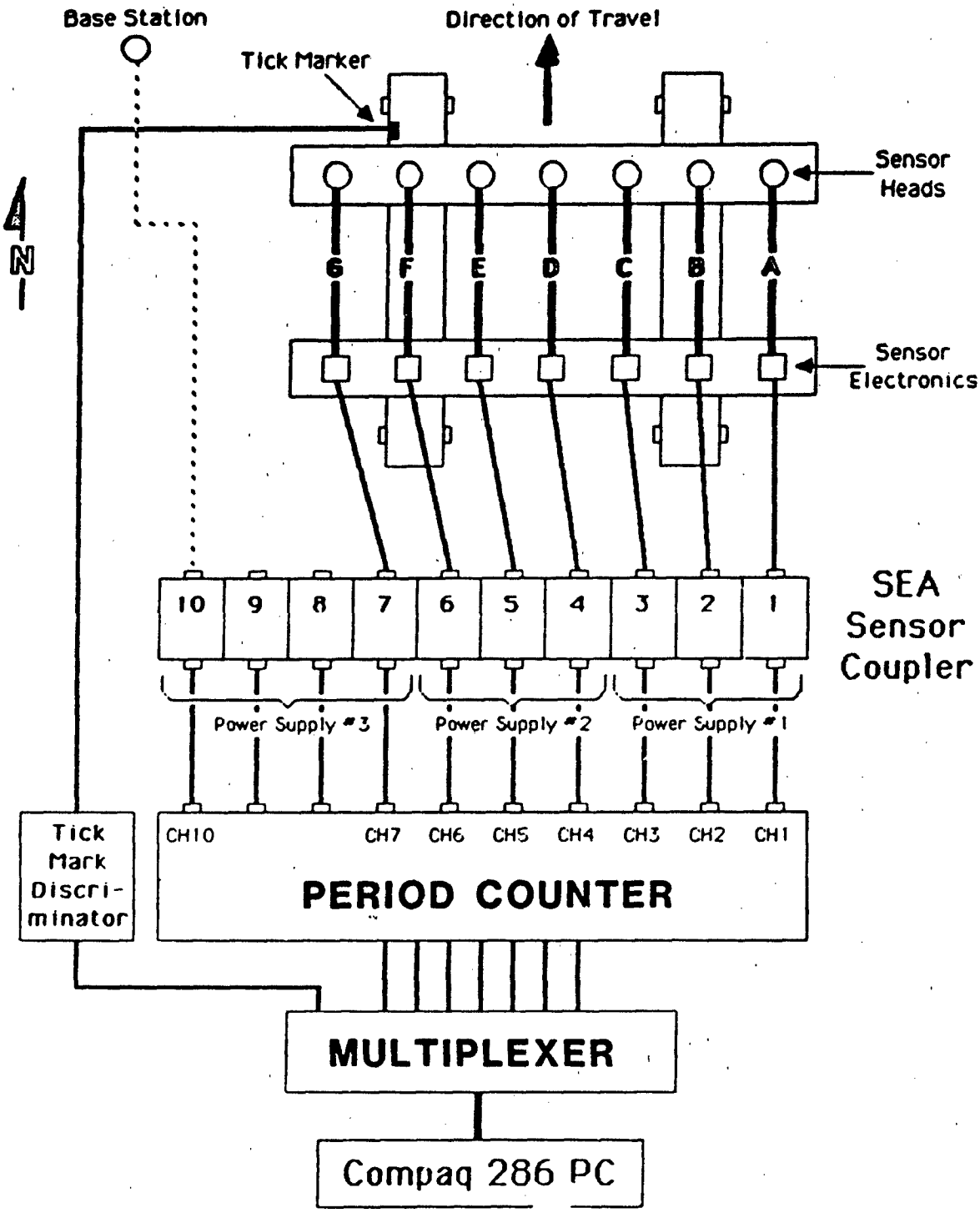

Figure 2-6. Data acquisition system block diagram.

GEO-CENTERS, INC.

the computer, since the hard disk drive was engineered for an office environment.

An I/O card, the "Six Pack" manufactured by AST, Inc., was added to the system to supply a real-time clock and additional input/output ports.

A ten channel analog/digital digitizer board, manufactured by Quatech, was added to the system to convert the analog data from the sensors to 12 bit digital numbers for computer processing.

The image processing system is based on the IBM PC/XT. It consists of an IBM Expansion Box, a PCVision card, an RGB color display, and ImageAction software. The PCVision card is made by Imaging Technologies. The color display is manufactured by BARCO Industries.

This system displays STOLS data in high resolution grayscale and color. Computer programs have been developed on this machine to locate and estimate depths of ordnance from characteristic patterns appearing in the magnetic field images.

The STOLS field computer is based on an IBM compatible Compaq 286 with math co-processor. This computer has 640 KByte of main memory and built-in monitor, a 360 KByte 5-1/4 inch floppy drive, and 20 MByte hard disk. A Hewlett-Packard ThinkJet printer provides hardcopy of the field data. The mother board provides three full slots and one half-slot for expansion boards. The field computer is used in conjunction with custom designed peripheral boards that connect the computer to the sensor interface electronics. These are: an X-BUS converter, a digitizer and a multiplexer. This computer has performed flawlessly at different test

sites under weather extremes. It is more portable and rugged than the original IBM PC/XT based system.

An IBM bus to X-bus converter was designed and built by GEO-CENTERS. This board plugs in one of the slots in the mother board and channels digital data from the digitizer board to the microprocessor. The schematic diagram and theory of operation are included in the Progress Report for July, 1986 [9].

A 15-bit parallel A/D converter of was designed and built by GEO-CENTERS that is X-bus compatible. It converts the analog signals from the PLL interface to high resolution digital data. Schematic diagrams and theory of operation are included in the Progress Report for July, 1986 [9].

A 16:1 analog multiplexer was designed and built by GEO-CENTERS. This circuit switches from the 16 input channels to one output channel that is connected to the digitizer. Any number and sequence of channels can be selected with the host computer software. Schematic diagrams and theory of operation are included in the Progress Report for July, 1986 [9].

The multiplexer board and digitizer board are housed together in a single enclosure external to the Compaq computer. Digital signals and power run over a single ribbon cable plugged into to the X-BUS card. Panel mount BNC connectors feed external analog signals to the multiplexer board.

STOLSAQ and STOLSPC are menu driven software programs for data acquisition with the field computer. STOLSAQ is used with

the Phase Lock Loop (PLL) interface. It provides for autocalibration of the PLL channels. STOLSPC is used with the Period Counter interface, which requires no calibration.

2.5.2 Sensor Interface

A portable gasoline powered generator supplies 115 volts AC to the field computer and DC power supplies. The AC also powers field instruments, such as: oscilloscope, frequency counter, soldering iron, etc.

Three separate 30-volt DC supplies, operating off 115 volts AC, are used to power the magnetometers and the sensor coupler. Three 12-volt lead-acid batteries have been purchased for tests of DC-only operation.

The sensor coupler passes DC power to the magnetometers. The high frequency signal from the magnetometers travels over the power lines to the coupler, which isolates and amplifies the signal for output to a frequency measuring device. Three types of coupler have been used in the field: the Varian sensor coupler, the NCSL (Naval Coastal Systems Laboratory) sensor coupler, and the SEA sensor coupler. All require 26-32 volts DC.

The Varian sensor coupler is original equipment for use with the Varian 2321 series magnetometer. Each coupler has built in ampmeter, on/off switch, indicator light, and fuse. One separate unit is required for each sensor employed.

The NCSL sensor coupler has features similar to the Varian and mounts in a standard 19 inch instrument rack.

The SEA sensor coupler is a single unit that accommodates up to 10 magnetometers. However, it lacks the ammeter, on/off switch, indicator light, and fuse featured by the Varian and NCSL couplers. Engineering changes were made by GEO-CENTERS to adapt the unit for field use.

A Hewlett Packard 1314A with IEEE instrumentation bus is operated in the field as a test instrument to calibrate individual magnetometers

The Phase Lock Loop (PLL) interface, designed and built by GEO-CENTERS, functions as a linear frequency-to-voltage converter. Two PLL circuits are contained on a single printed circuit board. The transfer function for each PLL is shown in the Progress Report for February, 1986 [11]. The PLL cards, along with power supplies, multiplexers, differential amplifiers, and the autocalibration card, are mounted in a standard 19 inch card cage. The interface operates off either AC or DC power.

The interface has performed without failure at Fort Polk, Louisiana, and Indian Head, Maryland.

Due to long-term drift of the analog PLL circuit, it is necessary to calibrate each PLL channel frequently during a survey. This operation is automated by an autocalibration card of GEO-CENTERS' design. Three crystal controlled frequencies are simultaneously miltiplexed to the PLL channels in a computer controlled sequence. In the autocalibration cycle, output voltages are obtained from each PLL circuit for each reference frequency. The computer calculates the frequency-to-voltage transfer function for each channel, from which the magnetic field strength, in gammas, is derived.

The period counter interface, designed by GEO-CENTERS, is X-bus compatible and gives readings of the magnetometers up to 20 times per second to 1 gamma accuracy. The electronics are all digital, which eliminates drift inherent to analog circuitry. The self-contained temperature controlled crystal oscillator (TCXO) regulates the frequency accuracy to 1 part per million. Two circuits fit on a two inch by six inch printed circuit board. Five boards in a single enclosure provide for 10 channels. This interface was used successfully at Yuma, AZ and, based upon its trouble-free performance, now replaces the PLL interface.

2.5.3 Telemetry

Telemetry is required for STOLS development. In the present system the platform sensors are tethered to the remote data acquisition system with a bundle of coaxial cables, restricting the search area within a circle of radius equal to the length of the tether. Wider ranging surveys require mounting the data acquisition system on the tow vehicle, and telemetering magnetometer base station and position data to the system. Furthermore, it is advantageous to transmit STOLS data in real-time to a support vehicle that monitors system functions, processes data, and relays operation commands.

A technical study by SEA, completed in November, 1985, details the system requirements for a multichannel radio telemetry system. Such systems are commercially available from manufacturers like Motorola and General Electric. After field demonstrations and technical evaluations, a system will be procured for STOLS development.

2.5.4 Data Handling

Computer software routines have been written that control the flow, formatting, storage, and retrieval of information as part of the data acquisition system. These are incorporated into a master data acquisition program. Because of hardware differences, separate programs were written for use with the PLL and the period counter interfaces.

An assembly language program, STOLSAQ, controls the acquisition of data with the PLL interface. The program is menu-driven, where the user sets the operation by entering parameters into prepared lines on the computer screen. The parameters include: digitization rate, channels to digitize, channels to display, autoranging display, and separation between channels. The program has been thoroughly tested and successfully used in the field.

An assembly language program, STOLSPC, controls the acquisition of data with the period counters. Like STOLSAQ, the program is menu-driven with similar options. The program has been tested and was used to collect data at Yuma, AZ.

Conclusion

A data acquisition system has been developed and successfully used in the field to obtain high quality data of magnetic anomalies over known ordnance items. A rugged computer and sensor interface have been field proven at test sites under weather extremes. Equipment and instrumentation have been identified as the prototypes for the next generation, free-roving STOLS platform.

2.6.0 DATA PROCESSING

This section discusses computer algorithms that have been developed to reduce and analyze data obtained with the STOLS field system.

2.6.1 Offset Correction

Field data is converted from digitized voltage to gammas through the PLL transfer functions. The transfer functions give the linear relation between Larmor frequency and DC voltage. The magnetometers output a sinusoidal frequency that is 3.49853 Hz per gamma of magnetic field strength. Because the analog PLL circuits tend to drift with time, calibration data is collected regularly at the start of each scan during a survey. The procedure records the PLL output voltage for three reference input frequencies.

We have found that, in a uniform magnetic field, the cesium vapor sensors exhibit fixed offset frequencies which may range from ± 20 Hz. This offset shows up in the data as a shift from ± 6 gammas,and must be removed to achieve the ± 1 gamma accuracy specification. In practice the offset has been determined empirically from stationary readings in a magnetically clean area. It is later subtracted from the data prior to interpolation. An example of data before and after offset correction is shown in Figure 2-7.

2.6.2 Interpolation

Because STOLS data is essentially a limited sampling of the Earth's magnetic field at the surface, which itself may be very

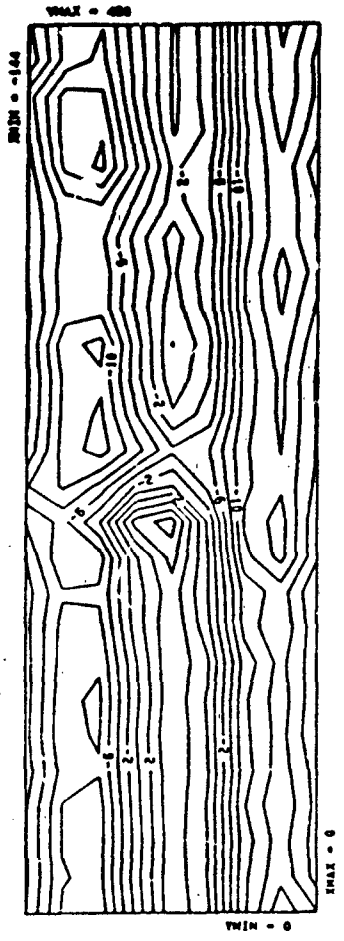

G4 - Cardinal Series

(a)

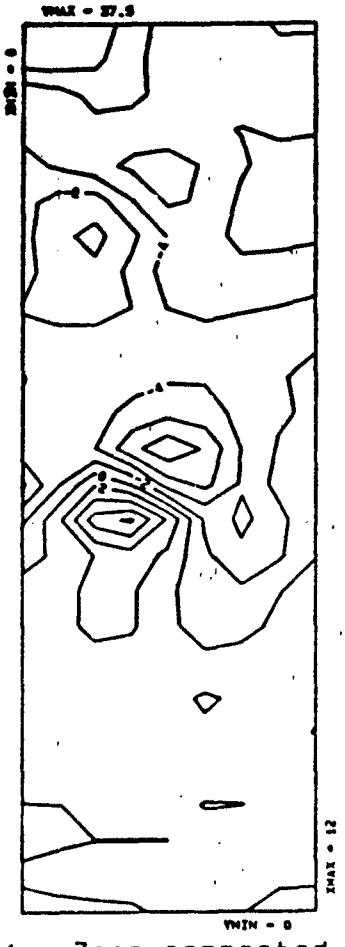

G4 - Zero corrected

(b)

Figure 2-7. Data before (a) and after (b) offset correction.

GEO-CENTERS, INC.

irregular, certain interpolation schemes are required to generate the magnetic image maps used for target location and identification.

Inverse Distance Squared (IDS) is an algorithm commonly used to interpolate points to fill in between evenly or randomly spaced data points. Interpolated points are assigned values weighted by the magnitude and distance to neighboring data points. A radius of interpolation restricts the set of points which may be used in the weighting function. IDS is useful for enlarging a STOLS image for better viewing on the monitor. The resulting image is slightly blocky, as can be seen in Figure 2-8, but can be smoothed out with a pillbox-type blurring algorithm.

A pillbox blur is a convolution that is very useful in eliminating the blockiness induced by enlarging images with IDS interpolation. An example is shown in Figure 2-9.

Cardinal Series Interpolation is an algorithm used to interpolate additional points in a gridded data set, where the data are equally spaced independently in both directions, but are much more densely packed in one direction than the other. This is the case in STOLS data, where readings are spaced very closely (centimeters) along the direction of travel, but are separated from the neighboring sensor readings by half a meter. The absolute magnitudes of the original data points are preserved through the interpolation process. The weighting function is a sinc function of the form $\sin(x)/x$. While this algorithm produces the best interpolation of a STOLS data set, it is numerically intensive and takes the most time. An example of this interpolation scheme is presented in Figure 2-10.

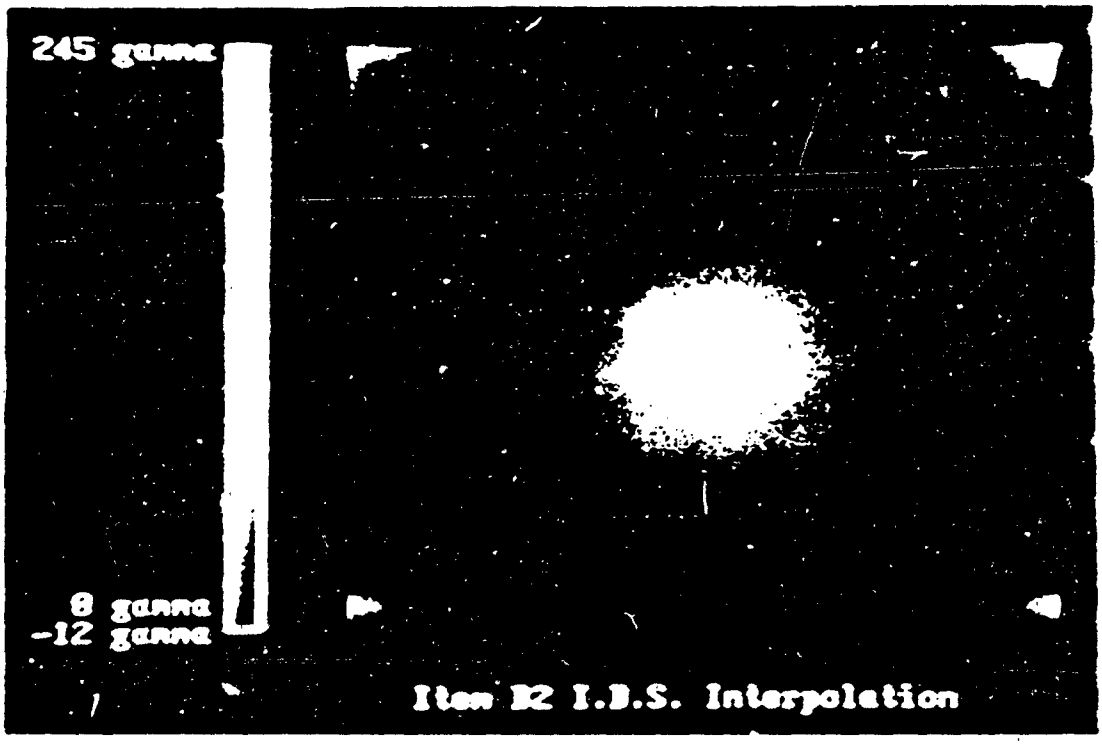

Figure 2-8. Inverse distance squared image.

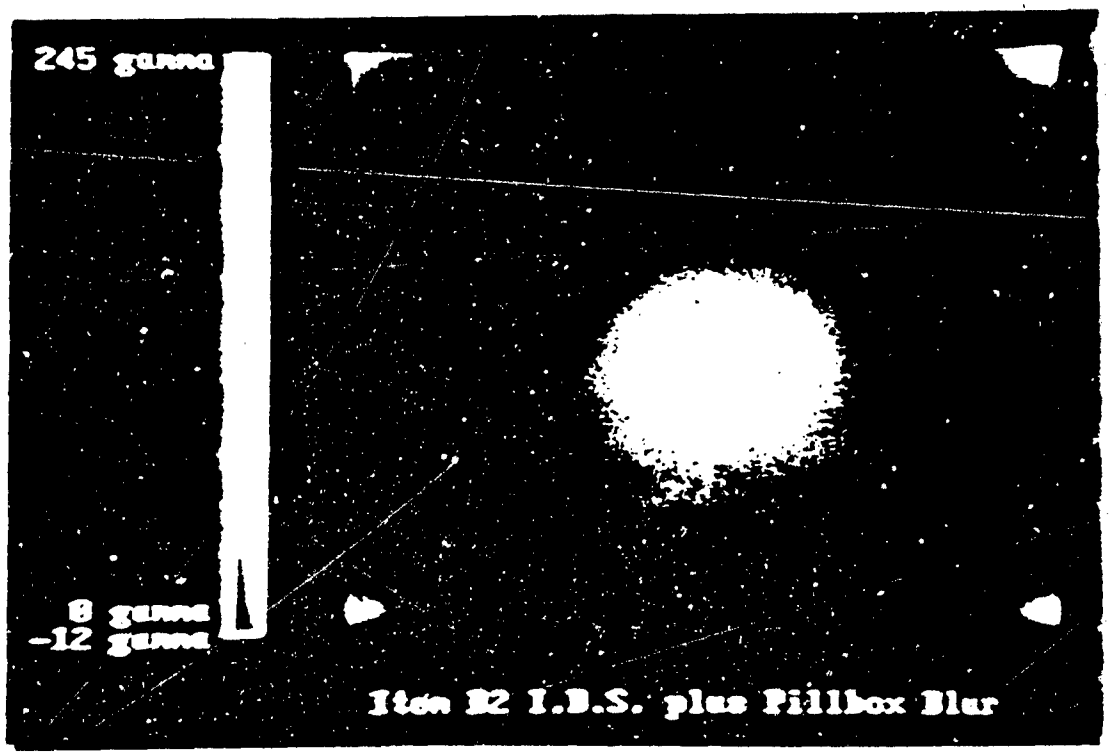

Figure 2-9. Pillbox blur image.

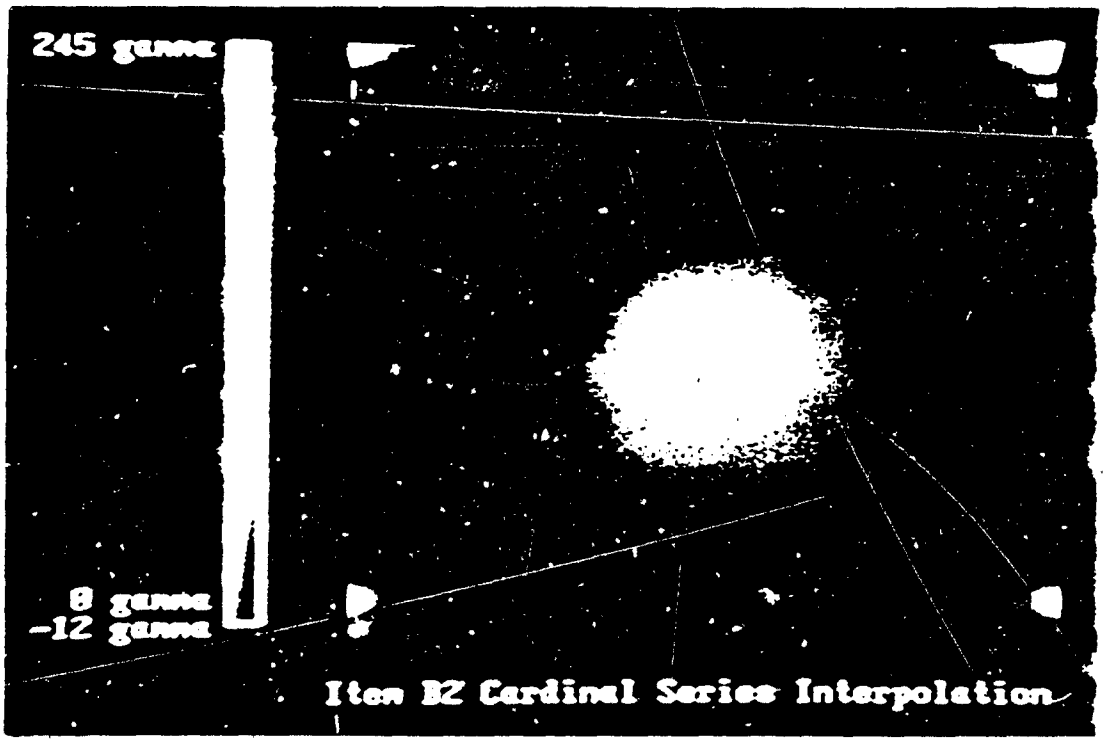

Figure 2-10. Cardinal series interpolation image.

GEO-CENTERS, INC.

2.6.3 Image Processing

Interpolated data is presented as grayscale or pseudocolor images for sophisticated image processing routines. An example from the data set from the MTR site at Indian Head, MD is shown in Figure 2-11.

The contouring of magnetic field data is a universally recognized and understood practice. A contour map is generated from the interpolated data with the use of a gridding program that interconnects points with the same amplitude. GEO-CENTERS uses a generalized contouring program developed by Golden Software in Golden, CO., as well as in-house software developed to extract contours, display them as images, and extract shape information. This software is used extensively in the analysis of STOLS data. An example of contoured data from the MTR site is shown in Figure 2-12.

The interpolated data is stored in computer memory, then normalized, scaled and stored in image memory for direct display on a color monitor. The contents of the image memory are mapped by a device called a look-up table (LUT), which determines how the image is actually displayed. The LUT assigns grayscale or color to the data in image memory, depending on the user's preference. Thus, to change how the image is displayed, one needs only to change the LUT, not the data in memory.

Preliminary work on shape specifiers has aimed at developing simple schemes to parameterize contour lines in terms of the angle and radial distance of locus points from the geometrical moment of the image. Progress Report from April, 1986 [2], discusses the results of this preliminary work. Another approach to shape speci-

Figure 2-11. Pseudocolor image of MTR data.

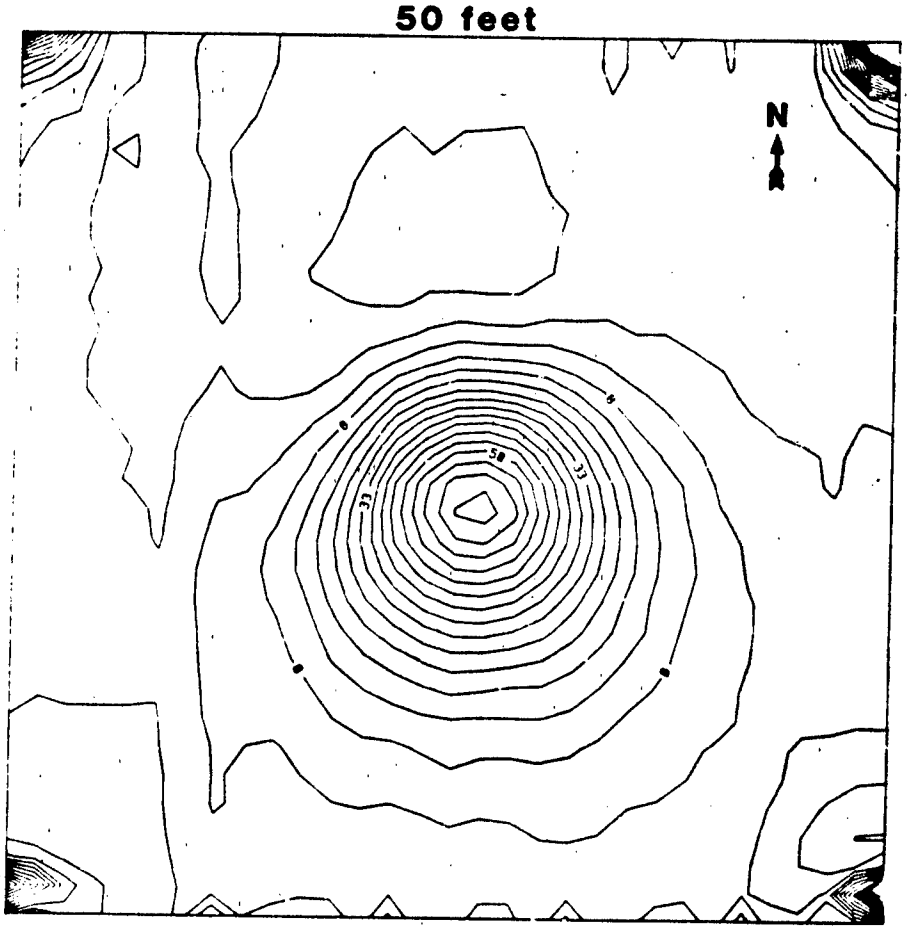

Item B2

Figure 2-12. Contoured MTR data of MK81.

GEO-CENTERS, INC.

fiers involves taking the two-dimensional Fourier transform of an image. An example is shown in Figure 2-13. Spatial amplitude and frequency are determining characteristics of a magnetic field anomaly. Transforming the data from the spatial domain to the frequency domain provides a method of condensing the data into a form that is readily cataloged and used in direct comparisons.

2.6.4 Location and Recognition

The full-width-half-maximum (FWHM) algorithm is an automated version of the traditional method of estimating the depth and location of buried magnetized bodies. Simply stated, the depth of the object is approximately equal to the distance between the half-maximum values along a line connecting the maximum and minimum peaks of a magnetic anomaly. The location is approximated by an offset distance added to the zero crossing point in the direction of the positive anomaly peak. Reasonable success is obtained in most cases. Table 2-3 was generated from this algorithm, which is now automated and operates on an area of interest drawn on the image screen by the user.

Inversion refers to determining the source of a magnetic field anomaly from a set of field data. This method is computationally intensive and requires high quality data for accurate estimates. We have received a computer program on magnetic tape from two investigators at DRES, Das and McFee. Efforts are underway to adapt this program to run on the MicroVAX.

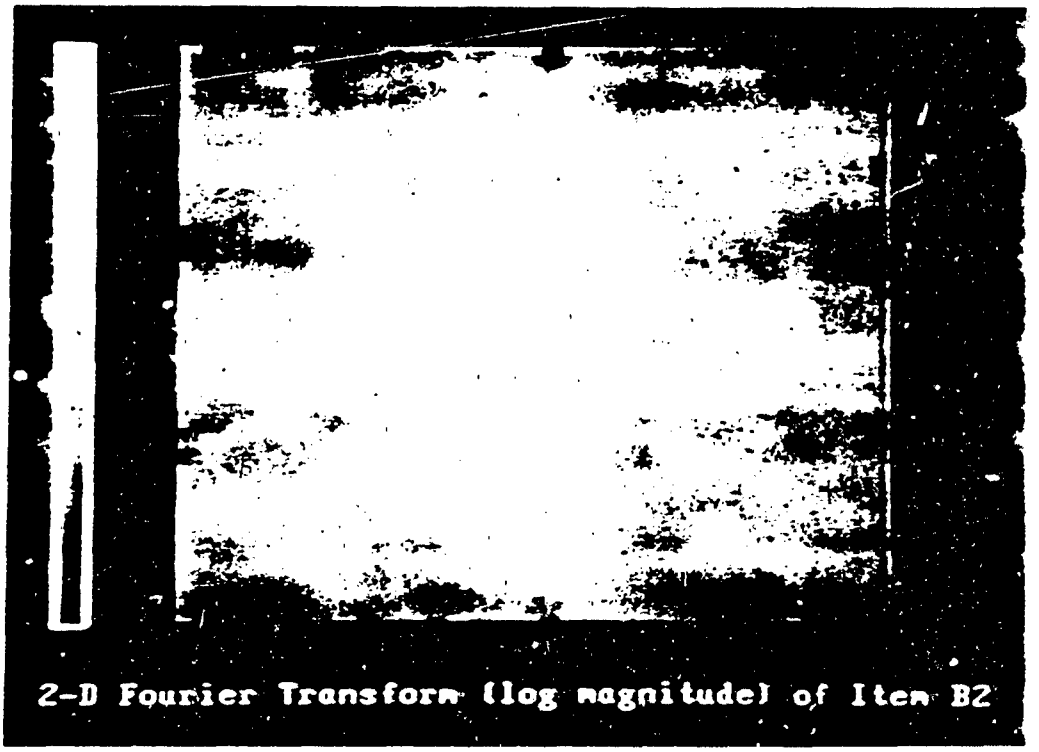

Figure 2-13. Two-dimensional Fourier transform image of MK81.

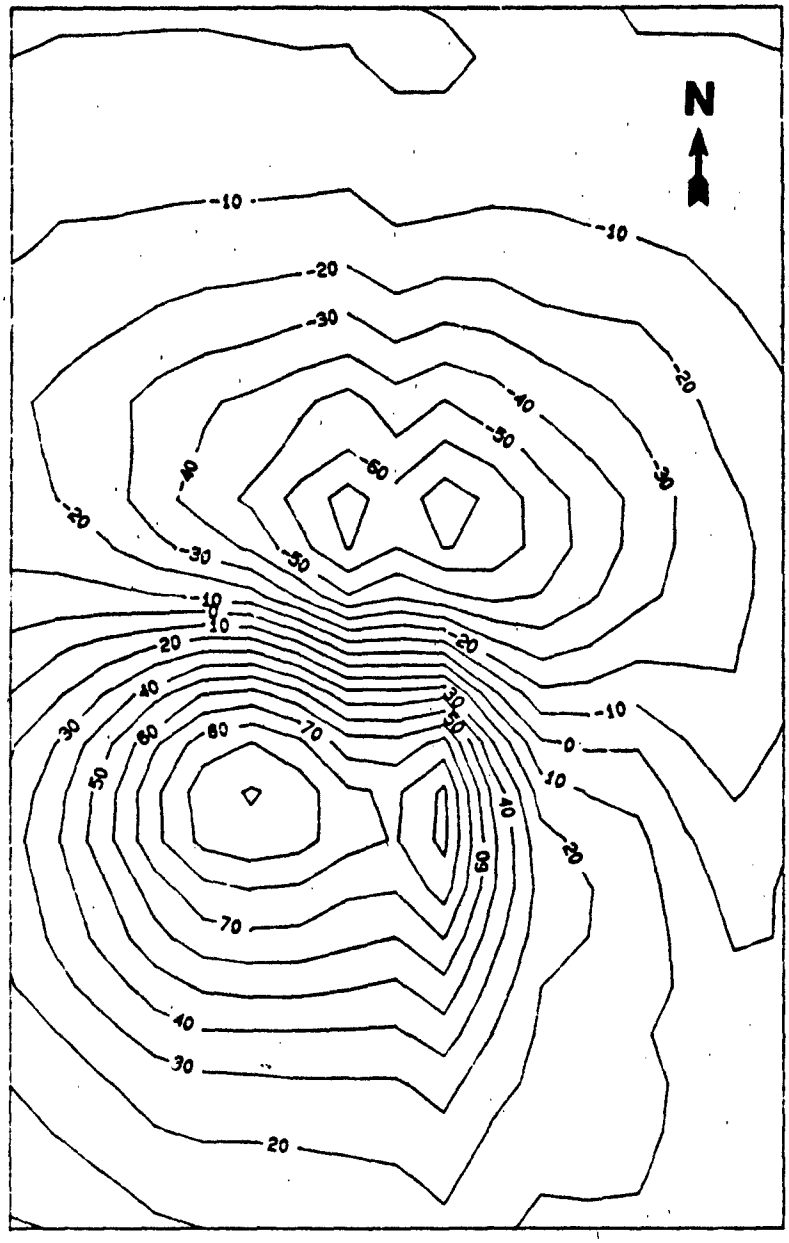

Figure 2-14. Contour map of Fort Polk, Louisiana, data of 500 lb. bomb.

TABLE 2-3

Location and Depth Estimations

Item	Ordnance Item	Ground Truth Depth (ft)	Ground Truth Location (N,E in ft)		Computer Estimation Depth (ft)	Computer Estimation Location (N,E in ft)	
A1	MK82 (500 lb)	14.4	125	125	10.9	121	124
A2	MK82 (500 lb)	15.0	78	76	16.8	78	74
B1	MK81 (250 lb)	10.1	175	125	9.1	174	125
B2	MK81 (250 lb)	9.5	124	76	11.8	126	75
C1	155 mm	4.6	188	62	6.4	189	60
C2	155 mm	4.0	75	123	6.8	76	123
D1	81 mm mortar	1.9	163	87	3.7	161	86
D2	81 mm mortar	1.4	212	78	3.6	212	87
D3	81 mm mortar	0.4	213	138	2.2	213	136
D4	81 mm mortar	1.4	237	111	2.8	238	111
E1	60 mm mortar	2.0	188	88	4.6	185	86
E2	60 mm mortar	0.7	163	62	3.5	164	64
E3	60 mm mortar	1.0	240	136	2.6	240	136
P1	practice bomb	1.3	212	111	3.8	211	111

Conclusion

We have developed powerful software tools to process raw STOLS data for interpolation, contouring, imaging, and automatic location finding. Investigations into methods of recognition and identification have uncovered several promising approaches. When implemented, these methods should be sufficient to predict automatically the type of ordnance buried at an identified location.

2.7.0 FIELD EXPERIMENTS

Field tests are a necessary part of STOLS development. The principal objectives of field tests are to catalog magnetic signatures of real ordnance items and to evaluate prototype STOLS hardware. Field tests have been performed at three test sites, each with different geological and geomagnetic characteristics. This section discusses the test sites and the measurement programs conducted at each.

2.7.1 Fort Polk, Louisiana

The site at Fort Polk, Louisiana, is situated in the Gulf coastal geological province. The soil is composed mainly of sand with a small percentage of clay and organic material. A variety of ordnance items were buried on-site at predefined locations and orientations. The site was used in training EOD personnel. The ordnance items were located at the center of 50 foot square areas. Corners of the grid areas were marked with steel stakes and the center of each area was determined from these corners. Field operations occurred in November, 1984, and preceeded the decommissioning of the site as a training ground. All known ordnance items were dug up and removed after the survey. A detailed map of the test site is given in Appendix E.

A reference base station was established in the vicinity of each ordnance item. A wooden track, composed of five 8-foot sections of plywood, was laid down in a north-south direction over each item. The wooden STOLS cart, supporting five cesium vapor magnetometers, was pushed the length of the track.

Field instrumentation consisted of GEO-CENTERS' Phase Lock Loops, as the front end, connected to an IBM PC/XT personal computer. Calibration data were recorded prior to and following each scan. A total of 64 data scans were taken over 32 buried ordnance items. The instrumentation performed flawlessly.

Figure 14 presents a typical contour map of data collected at the site. Detailed results of the Fort Polk, Louisiana, survey are contained in the Progress Report of February, 1985 [10].

2.7.2 Indian Head, Maryland

The magnetic test range (MTR) at NAVEODTECHCEN, Indian Head, Maryland, is designed to test the full capabilities of the STOLS system. Located on a knoll in eastern Maryland, the MTR is 100 feet by 200 feet in extent. The local soil is predominantly clay with intervening layers of coarse gravel. The area is cleared and graded. Fifty foot grids are permanently staked out with short steel rods for rapid detection with a search magnetometer. Within the MTR, 14 ordnance items are buried with accurately defined locations and orientations.

The Progress Report of April, 1986 [2], and Appendix E of this report give a full description of the site layout.

In the May 1986 field tests, the Mark III platform was used with seven sensors. The instrumentation consisted of the Compaq 286 field computer with the PLL interface. South to north trending scan lines spaced 10 feet across allowed complete coverage of the site. Following the south-north scans, experimental east-west scans, southwest-northeast scans, arc scans, fast scans, and south-north scans with shrapnel ground clutter were performed. A

Figure 2-15. Magnetic image map of MTR.

GEO-CENTERS, INC.

total of 89 scans were taken over 14 ordnance items. A full interpolated magnetic image map obtained over the area is presented in Figure 2-15.

The Progress Report of June, .1986 [8], gives exact details of field methods used and preliminary results obtained at the May tests.

2.7.3 Yuma, Arizona

The test site at Yuma, Arizona, was designed to obtain maximal magnetic signatures of known ordnance items. The site measured 20 feet wide by 40 feet long in the north-south direction. A 15-inch diameter PVC tube served to hold and align the ordnance items in the Earth's magnetic field. A 10-foot length was buried in the sand inclined 60 degrees to magnetic north. The site was level and clean of all metallic objects.

The data consist of magnetic field measurements from four cesium vapor sensors mounted on the STOLS Mark III platform, one stationary cesium vapor sensor mounted on an upright wooden post, and tick marks from the microswitch mounted on the platform. Field instrumentation consisted of the Compaq 286 field computer and the period counter interface. Data was acquired by pushing the platform from south to north along two parallel lines, one east and one west of the center line over the tube. A picture of field operations is given in Figure 2-16.

Bombs were lowered into the tube by a truck mounted crane. Measurements were taken with the bomb nose down and taildown. Measurements of MK82 bombs were made directly. For measurements of MK81 bombs a wooden spacer was inserted in the tube to hold the

Figure 2-16. Field operations at Yuma, Arizona.

bomb nearer to the ground surface. A total of 148 scans were collected over 37 different bombs. Preliminary analysis of the data indicates that bombs of the same class possess different magnetic signatures. This result confirms that different magnetic moments are produced in the same type of ordnance at the same orientation and depth. We are still in the process of analyzing the data to identify the sources of variation in the observed moments.

2.8.0 CONCLUSION

The goals of the effort reported here were met. STOLS sensors, data acquisition system, wheeled platform, and computer software were designed, constructed, and tested in the field. The performance of these components has met with system requirements. High quality data of magnetic anomalies of ordnance items and system tow vehicles were obtained, and these form an initial catalog of ordnance magnetic signatures for use with computer recognition software. Data processing algorithms have been successfully applied to field data for offset corrections, noise reduction, and automatic location estimation.

References

1. Suffield Report Number 283, "Detection and Identification of Buried Ordnance by Magnetic and Electromagnetic Means (U)", by Y. Das, J.E. McFee and M. Bell, June 1981.

2. GEO-CENTERS, INC. Monthly Progress Report for April, 1986, prepared for NAVEODTECHCEN, Indian Head, Maryland.

3. GEO-CENTERS, INC. Monthly Progress Report for May, 1986, prepared for NAVEODTECHCEN, Indian Head, Maryland.

4. GEO-CENTERS, INC. Monthly Progress Report for July, 1985, prepared for NAVEODTECHCEN, Indian Head, Maryland.

5. GEO-CENTERS, INC. Monthly Progress Report for November, 1985, prepared for NAVEODTECHCEN, Indian Head, Maryland.

6. GEO-CENTERS, INC. Technical Report GC-TR-536-03, February, 19985, prepared for NAVEODTECHCEN, Indian Head, Maryland.

7. GEO-CENTERS, INC. Monthly Progress Report for March, 1986, prepared for NAVEODTECHCEN, Indian Head, Maryland.

8. GEO-CENTERS, INC. Monthly Progress Report for June, 1986, prepared for NAVEODTECHCEN, Indian Head, Maryland.

9. GEO-CENTERS, INC. Monthly Progress Report for July, 1986, prepared for NAVEODTECHCEN, Indian Head, Maryland.

10. GEO-CENTERS, INC. Monthly Progress Report for February, 1985, prepared for NAVEODTECHCEN, Indian Head, Maryland.

11. GEO-CENTERS, INC. Monthly Progress Report for February, 1986, prepared for NAVEODTECHCEN, Indian Head, Maryland.

SECTION 3

BOREHOLE ORDNANCE DETECTION SYSTEM

TABLE OF CONTENTS

TABLE OF CONTENTS (cont.)

LIST OF FIGURES

LIST OF TABLES

3.1.0 INTRODUCTION

The depth to which ordnance becomes buried depends on the ordnance type and local soil mechanics. A streamlined bomb striking a weak, poorly consolidated soil with high kinetic energy may penetrate to 10 meters (30 feet) or more. The overall objective of the borehole ordnance detection system (BODS) is to locate and identify ordnance items buried beyond the detection range of surface sensors. The objective of the effort reported here is to identify practical and effective methods of ordnance location using available subsurface technology.

Surface detection methods are limited in the depth of penetration and resolution. The effectiveness of surface magnetic methods, for example, is limited to approximately five meters (15 feet) depth. This is because the magnetic field due to ferrous objects drops off rapidly in strength with distance. Borehole detection methods overcome the limitations of surface methods by placing the detectors closer to the deeply buried target.

This report summarizes our investigations into current borehole remote sensing technology and presents results of field experiments to test BODS instrumentation and data processing algorithms.

3.2.0 REVIEW OF BOREHOLE SENSING TECHNIQUES

A large body of work on borehole sensing techniques exists, mainly in the field of geophysical exploration for mineral and energy resources. A review of these techniques is presented along with an evaluation of their applicability to the specific problem of locating deeply buried unexploded ordnance. Of the methods reviewed below, magnetometry and ground penetrating radar have potential for remote sensing of buried ordnance. These are described in detail in Sections 3.3 and 3.4.

3.2.1 Magnetic

Magnetic detection techniques have the oldest history of any. The principles are based on the well-understood science of magnetostatics, which relates the ferromagnetic properties of an object to magnetic field effects detectable at a distance. From knowledge of the magnetic field in a region, its source can be inferred. As a general rule, the magnetic field is not attenuated by the intervening earth. The field measured at any point is a simple superposition of the magnetic fields due to individual sources, depending only on their distance from the measurement point. Because the magnetic field exists independently of the observer, purely passive means may be used in detection.

Magnetic field measurements are obtained with either a total field measuring device, or a single axis (or vector) field measuring device. The most commonly used total field magnetometer is the proton precession type, which attains accuracies to 0.1 gamma. Surface, borehole, marine, and airborne versions of this instrument are commercially available. Another type of total field

magnetometer with equivalent accuracy, the cesium vapor, is available, though at considerably greater expense.

The most commonly used single axis magnetometer is the fluxgate type, which will measure 10 gammas with a sensitivity to changes of 1.0 gamma. A wide range of fluxgate magnetometers are commercially available for surface and borehole surveys. The difference in precision means that the proton precession instrument can potentially detect ordnance items at a distance five times greater than the less sensitive fluxgate instrument.

Historically, borehole magnetic detection methods have been used by British and German authorities in very localized searches for unexploded ordnance. They have not been used for widescale range clearance.

3.2.2 Electromagnetic

Electromagnetic borehole techniques are based on the effects that electrical properties of materials have on propagating electromagnetic radiation. The physics that govern the interaction of matter with electromagnetic energy is well defined, and remote sensing technologies based on the physical principles have matured. Because bodies in a state of equilibrium with their surroundings do not radiate, electromagnetic detection methods rely on the response of buried bodies to artificially generated electromagnetic fields and therefore are active methods.

Two techriques are discussed below: ground penetrating radar (GPR) and EM conductivity. Of these, only the GPR is suitable for remote sensing of deeply buried ordnance.

3.2.2.1 Ground Penetrating Radar

A borehole ground penetrating radar (GPR) system transmits pulses of electromagnetic radiation and receives reflections from electrical discontinuities in the earth. A buried bomb represents a very strong electrical contrast to the surrounding earth, because the metal casing is orders of magnitude more conductive than naturally occurring soil constituents. An incident electromagnetic pulse is virtually totally reflected from the metal surface. The effectiveness of GPR depends on the electrical properties of the earth encompassing the radar antenna and target, and on the radar cross-section of the target. These topics are addressed in Section 3.4 below.

A basic GPR system consists of a power supply, an electronic control unit, transmitter/receiver electronics, a pair of antennas, and a graphical output device. A block diagram for a typical surface GPR system is illustrated in Figure 3-1.

Commercially available GPR systems are primarily designed for surface reconnaissance surveys. The systems are complicated and highly skilled operators are required for valid data collection and interpretation. Surface GPR is effective in detecting and locating shallow buried metallic objects, as is demonstrated in the RADAR section of this final report. Borehole antennas are available for mine engineering studies and tunnel detection, which are large scale phenomena. Customized borehole antennas need to be engineered for the specific application of detecting deeply buried ordnance, since this represents smaller scale phenomena.

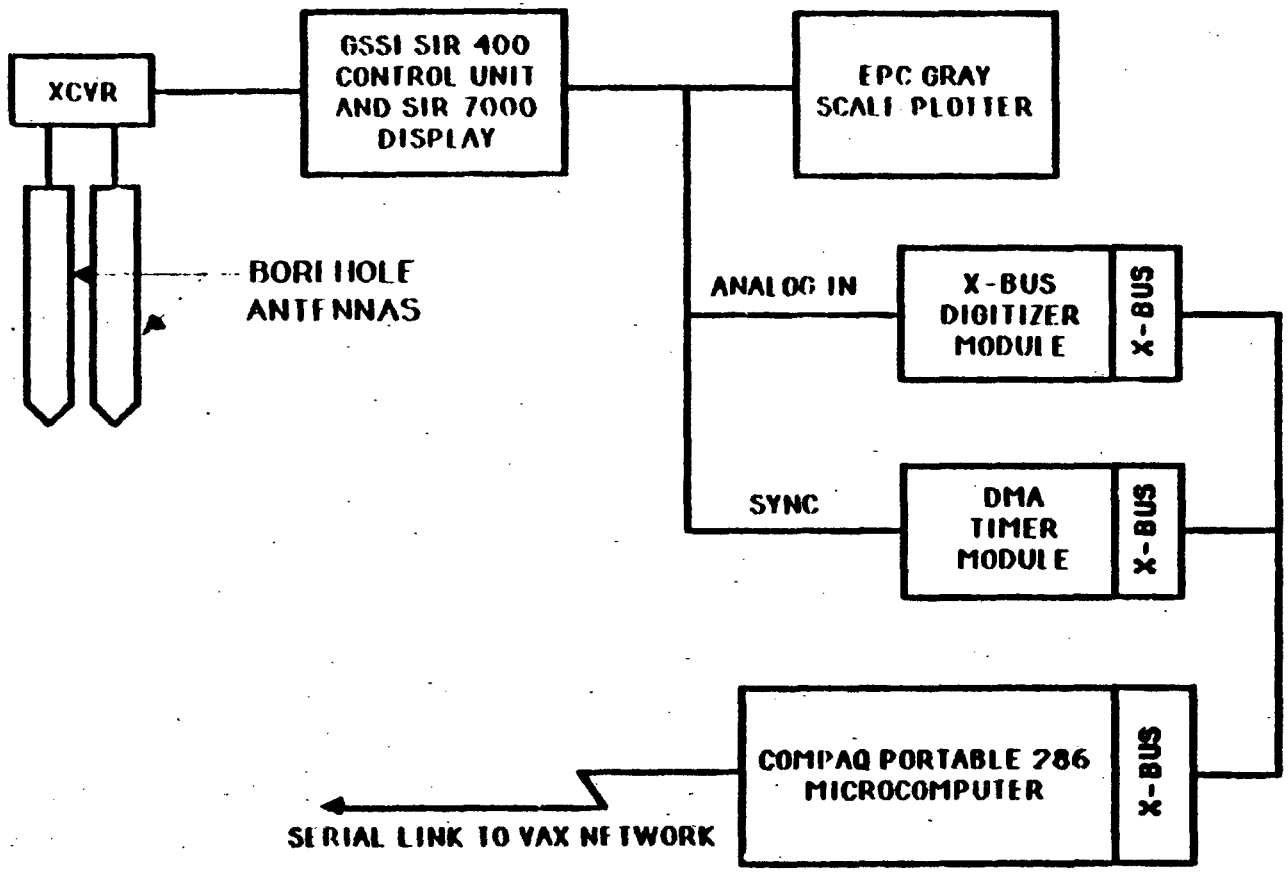

Figure 3-1. Schematic of borehole radar data acquisition system.

3.2.2.2 EM Conductivity

Electromagnetic (EM) conductivity relies on the Faraday induction principle, which relates secondary induction currents to primary induction currents at a distance. The technique operates by generating a time-varying primary magnetic field in a transmitter loop and detecting the secondary magnetic field produced by electric currents at a distance, flowing in response to the primary field. The magnitude of the secondary field is proportional to electrical conductivity within a certain range of the transmitter. The effective range depends on the operating frequency and the electrical properties of the earth. The large metal mass of an ordnance item acts as a very highly conducting region. In principle, this is detectable using EM technology.

Commercially available EM systems, designed for geophysical exploration applications, measure the bulk conductivity of the earth. Borehole EM sensors are engineered to measure the conductivity of the rock immediately surrounding the borehole. None operate beyond a range of one meter. In view of the fact that suitable EM probes are unavailable, no further consideration is given to the EM technique.

3.2.3 Electrical

Electrical techniques measure the electric potential set up in a region by electric currents injected into the ground from controlled sources. In the earth, the currents tend to follow paths of least resistance. In the vicinity of very conductive bodies, such as a bomb, the current concentrates, causing the electric potential to drop. This effect is depicted in Figure 3-2. The exact relationship between the current distribution and

The Effects of a Conducting Body on Electric Field Measurements

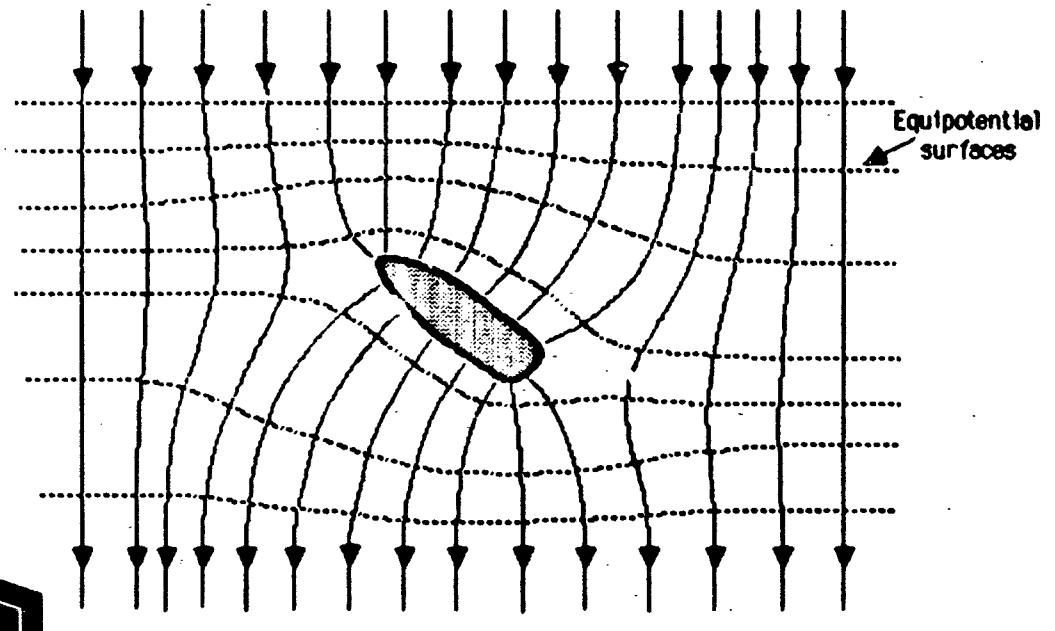

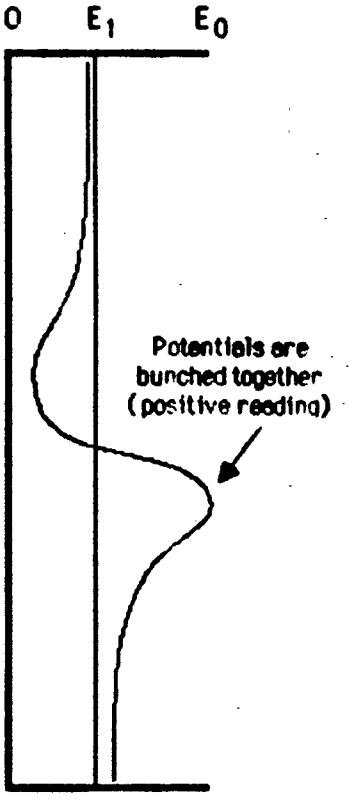

Plot of the Anomaly Field

Figure 3-2. Electric potential in vicinity of a bomb.

the potential field is understood through Maxwell's equations. In general it is extremely complex. Under the best of circumstances, electrical measurements give a qualitative, rather than definitive, representation of the conductivity structure of the earth. Consequently, the technique may have some utility for detection but not for location.

Electrical methods are widely used in geophysical prospecting to characterize the subsurface. The majority of commercially available electrical systems are designed for surface reconnaissance. Specialized borehole tools are manufactured for oil and water well engineering. These have been evaluated for their potential application to ordnance detection. None of the three techniques discussed below are suitable for detection of deeply buried ordnance, but they are included here for completeness.

3.2.3.1 Resistivity

Resistivity measurements require direct contact with the earth. In borehole applications, the voltage electrodes are placed in the borehole. The current electrodes may either be placed in the same borehole, in another borehole, or on the ground surface. A collinear geometry, with the current electrodes at the ends and movable voltage electrodes in-between, is optimal. The measured quantity is the ratio of the measured voltage to the controlled current. The detection radius is a function of current and voltage electrode geometry. A rule-of-thumb for surface (half-space) measurements is two-thirds the current electrode spacing. An estimated rule-of-thumb for borehole resistivity (semi-whole-space) is one-third the current electrode spacing, which is limited by the depth of the hole. The technique is inherently sensitive to near hole electrical variations and rel-

atively insensitive to conductive targets farther from the hole than one-third the current electrode spacing. Therefore, to be effective, very deep boreholes (approximately twice as deep as expected targets) would have to be drilled to allow for a larger electrode spacing. Due to this limitation, no further consideration is given to borehole resistivity.

3.2.3.2 Self-potential

Self-potential (SP) is similar to the resistivity method. Instead of being artificially created, as with the resistivity method, the measured voltages are naturally occurring as a result of regional telluric currents and local electrical anomalies. Observed potentials may result from oxidation/reduction chemical reactions occurring in the soil at the metal surface of an ordnance item, where an electrochemical potential exists at the soil/metal contact. Measurements are made of the electric potential field with movable, non-polarizing voltage electrodes.

The electrode spacing of commercially available SP loggers is very limited. As with resistivity, the detection radius depends on the electrode spacing. Downhole SP measurements are generally extremely sensitive to gross changes in lithology and changes in flow rates of interstitial pore fluids present in the ground. Because of the very low signal levels, the measurements are time-consuming and difficult to interpret. These factors rule out SP as a method for ordnance detection.

3.2.3.3 Induced Polarization

Induced polarization (IP) measures the capacity for chemical charge storage of the ground. A controlled current source charges

electrically active boundary zones in the vicinity of the current electrodes. The presence of oxidation/reduction reaction zones is indicated by the slow decay of the secondary electrical current after the charging current is switched off. The surface of a buried ordnance item may be the site of exchange reactions detectable by this method. This depends on the composition of the soil and the metal casing of the item.

Commercial IP systems are designed primarily for surface geophysical exploration. In borehole tools, the restricted spacing of the electrodes limits the detection zone to very near the borehole. Measurements are slow and interpretation of the data is exceedingly difficult. For these reasons IP is not considered a viable detection method.

In conclusion, electrical borehole methods are not feasible for remote sensing of deeply buried ordnance. The main limitation is the limited detection distance possible with closely spaced electrodes in the borehole. Moreover, all electrical methods require direct electrical contact with the earth, ruling out its use when cased holes are required.

3.2.4 Acoustic

The acoustic reflection technique utilizes a controlled seismic source and one or more seismic detectors. The system detects and records signals reflected off acoustic impedance mismatches.

While there are many systems on the market which utilize acoustic waves for imaging the subsurface, they are all fundamentally low resolution due to the low frequency of operation.

Ultrasonic systems, which operate on frequencies with wavelengths short enough to detect a large ordnance item, are useless because of the rapid attenuation of high frequencies in the earth. Therefore, acoustic methods cannot be used successfully for borehole ordnance detection.

In conclusion, of the borehole sensing techniques reviewed, the ones with potential for remote sensing of deeply buried ordnance are magnetometry and ground penetrating radar. These two methods are discussed in the remainder of this report.

3.3.0 ORDNANCE DETECTION USING BOREHOLE MAGNETOMETERS

Magnetic methods are proven to be effective in locating buried explosive ordnance. Surface measurements, such as obtained with a surface towed ordnance locator system (STOLS), are able to detect large classes of ordnance to a depth of 15 feet. For more deeply buried ordnance the use of borehole magnetometers becomes necessary. Two types of borehole magnetometers have been evaluated for borehole ordnance detection: proton precession and fluxgate. The former makes total field readings while the latter makes single axis, vector field readings or gradiometric readings. Magnetic field theory required for data reduction and analysis is presented in this section, along with details of the data acquisition instruments and methods of data collection in field tests. The minimum spacing adequate for complete detection of buried ordnance is specified, based on the results of computer modeling and field experiments.

3.3.1 Magnetic Models

Predictive magnetic models are essential in analyzing the magnetic field anomalies generated by deeply buried ordnance. One model developed by GEO-CENTERS calculates the induced dipole moment of a magnetically permeable, solid spheroid. A second model generates the three-dimensional magnetic field anomaly for a magnetic dipole with given location, strength and orientation.

3.3.1.1 Induced Moment of Spheroid

We have implemented a computer model which computes the induced magnetic dipole moment of a magnetically permeable, solid

spheroid. The model produces results in close agreement with most classes of ordnance items. We expect that refinements to the model will give better approximations to various ordnance items. This model is described in detail in Section 2.2.1 of the STOLS section of this final report.

3.3.1.2 Induced Magnetic Field Anomaly

A buried ferromagnetic object distorts the ambient magnetic field surrounding it. In boreholes this distortion manifests itself as a localized magnetic field anomaly. The variations that comprise the anomaly are a function of the source dipole (its orientation and depth).

Our model allows the rapid generation of magnetic anomaly maps over three-dimensions for these source dipole parameters: magnetic moment, inclination, azimuth, and depth; and these earth magnetic field parameters: inclination and intensity. The mathematics of the model is presented in Appendix B. An example produced by this model is presented in Figure 3-3.

In conclusion, we have developed computer models that closely approximate the moment induced in deeply buried ordnance, and that generate representations of the three-dimensional magnetic anomalies caused by buried ordnance.

3.3.2 Data Acquisition System

The data acquisition system is a simplified version of the STOLS system, described in Section 2.5.0 of this report. A Compaq 286 portable computer is used in the field for acquiring and storing the data from borehole sensors. The computer contains a

Figure 3-3. Three-dimensional magnetic field model - MK82.

GEO-CENTERS, INC.

GEO-CENTERS' X-BUS Converter to interface with the multichannel digitizer designed and built for the STOLS project. A system block diagram is shown in Figure 3-4a.

Two EG&G G-856 proton precession magnetometers were used for field experiments. Each has the capability to store 1000 station readings. The unit operates in manual or autocycle mode. A special cable plugs directly into the front panel of the magnetometer and into the RS-232 port of the computer. Data is transferred from the magnetometer to a computer data file using a standard ASCII format transfer. A system block diagram is shown in Figure 3-4b.

The Foerster Ferex 4.021 fluxgate magnetometer outputs an analog signal which is proportional to the magnetic field reading. The Foerster probe contains two fluxgate sensors spaced 40 cm apart. Four operating modes are selectable: static absolute (SA), static difference (SD), dynamic absolute (DA), and dynamic difference (DD). The absolute settings measure the field at one sensor, whereas the difference settings measure the difference in the field between the two sensors. The dynamic setting makes the instrument sensitive to time varying changes in the magnetic field. A built-in meter and loudspeaker provides visual and audio indications of magnetic field anomalies. A connector on the side delivers a DC analog signal proportional to the reading.

The DC signal from the Foerster is sent over a coaxial cable to the digitizer unit, where it is converted to a 15-bit number. The digitization rate can be set by the user up to a maximum of 20 samples per second. Details of the borehole ordnance detection system magnetometer data acquisition system can be found in the Borehole Progress Report for April, 1986 [1].

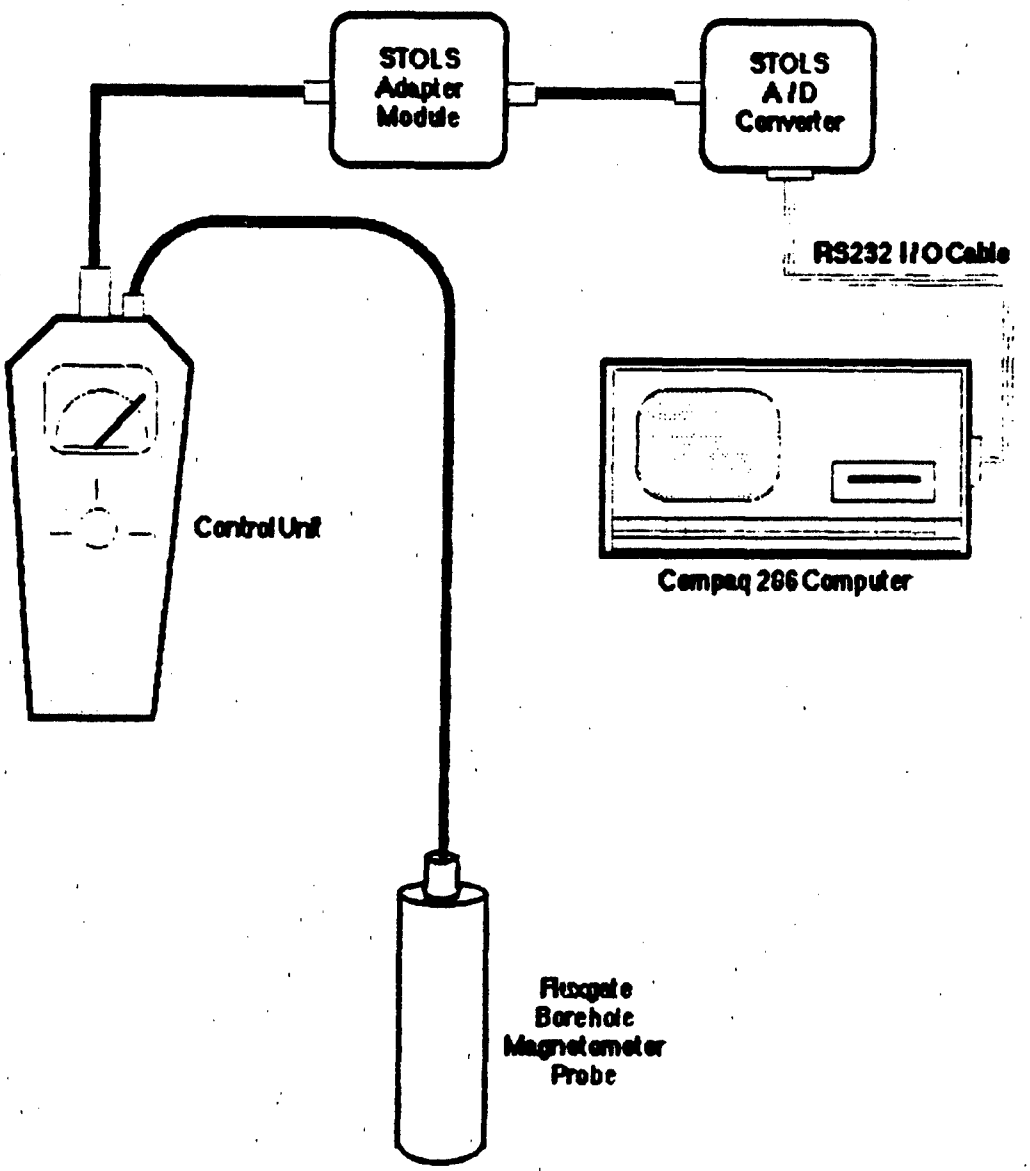

Figure 3-4a. Fluxgate magnetometer data acquisition system.

GEO-CENTERS, INC.

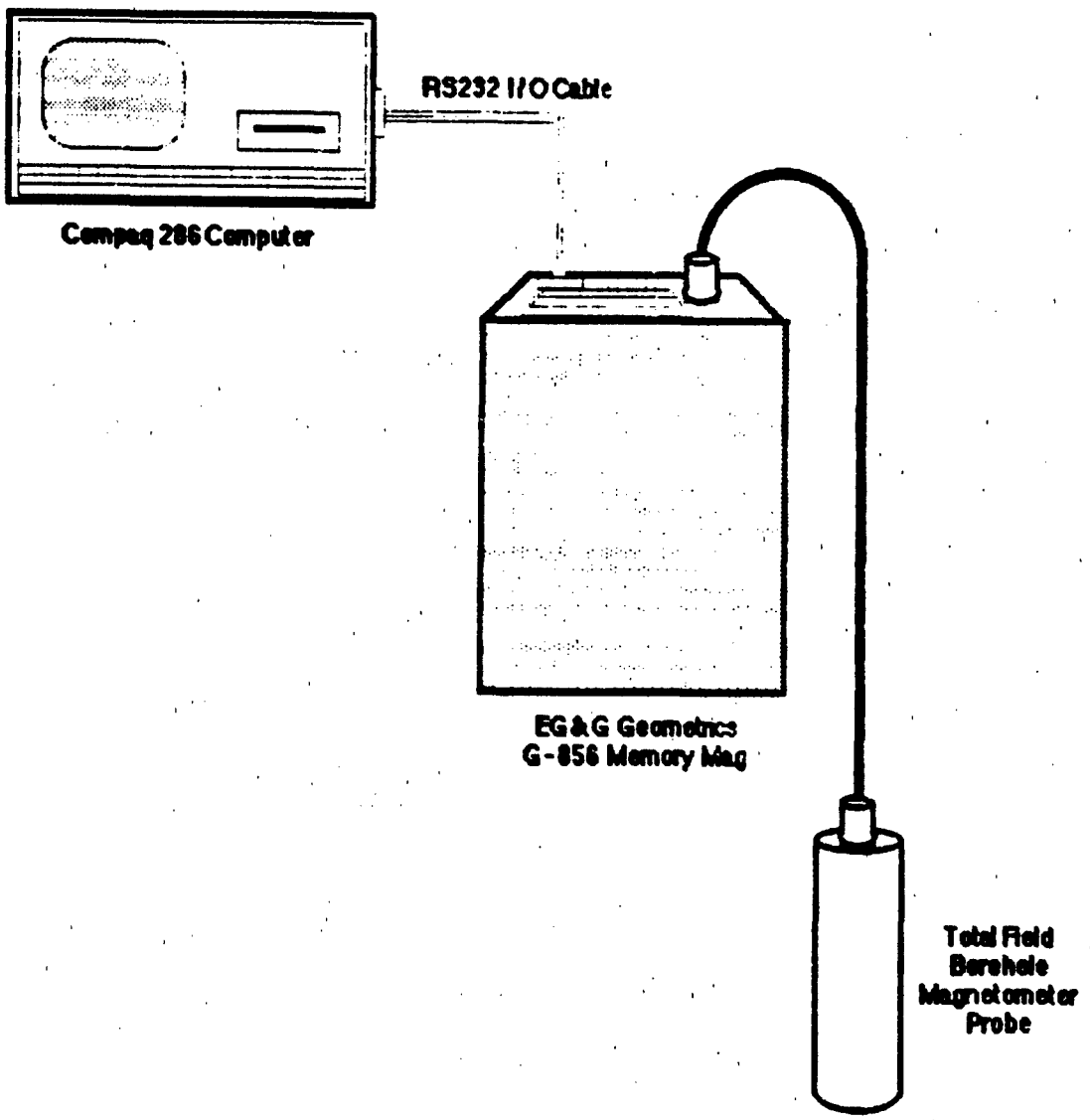

Figure 3-4b. Total field magnetometer data acquisition system.

3.3.3 Field Experiments

Borehole magnetometry data were collected at two control test sites. One site is located at NAVEODTECHCEN in Indian Head, MD. The other site is at the Cold Regions Research and Engineering Laboratory (CRREL) in Fairbanks, Alaska. Field experiments were designed to collect baseline data of the magnetic field anomalies surrounding buried ordnance. The details of these experiments can be found in the Borehole Progress Reports for January [2], February [3], April [1], and June, 1986 [4].

3.3.3.1 Test Sites

The test site at Indian Head consists of 12 4-inch boreholes drilled in a symmetrical pattern about two buried ordnance items: a 500 pound bomb and a 155 mm projectile. The exact location and orientation of the items are known. A site plan is presented in Appendix E of this report.

The test site at CRREL, Alaska, consists of 12 3-inch inside diameter boreholes drilled in a symmetrical pattern about two buried ordnance items: a 500 pound bomb and a 155 mm projectile. The exact location and orientation of the items are known. The site was inadvertently laid out in a different plan than the site at Indian Head. A site plan is presented in Appendix E of this report.

3.3.3.2 Total Field Measurements

Total field measurements were taken down each borehole at 0.5 foot intervals, using an EG&G G-856 proton precession magnetometer with an EG&G borehole sensor. This instrument is accurate to 0.1

gamma. A second G-856 magnetometer was used as a remote base station to record natural variations in the ambient magnetic field. The data was transferred to the computer and stored on floppy disks.

3.3.3.3 Fluxgate Measurements

Measurements were made down each borehole with the Foerster Ferex 4.021 fluxgate magnetometer. Continuous magnetic profiles were obtained by recording the analog output as the probe was continuously lowered. Tick marks were made at every 1 foot interval. At the completion of a profile, a total magnetic field reading was made at the top of the hole for calibration purposes. The instrument was run in two different modes for data collection: the static difference mode and the static absolute mode.

3.3.3.4 Three-dimensional Measurements

Initial magnetic field measurements have been made in three-dimensions around ordnance items at Indian Head, MD., using EG&G G-856 proton precession magnetometers. A non-magnetic tripod stand holds the item at a fixed height, up to 10 feet, and in a fixed orientation. The sensor is supported at fixed heights by a non-magnetic, vertical upright. The sensor is positioned at one foot grid points in a 30 x 20 foot area. The longer dimension is aligned north-south. The measurement space around an object is 30 x 20 x 20 feet, sampled at variable intervals horizontally and vertically. The variable intervals account for the magnetic field gradient around the object. Thus, far from the test item a five

foot spacing is adequate. At intermediate distances a two foot spacing is sufficient, and close to the item, a one foot interval is necessary. A remote base station records diurnal variations to correct for fluctuations in the Earth's field.

3.3.4 Data Processing

3.3.4.1 Total Field Data

Removal of diurnal variations was the first step in processing the total field data. Reference base station data was subtracted from the field data. Evenly spaced grid points were interpolated between the borehole data points to produce a three-dimensional data set. The data was displayed on the image processing system. A comparison between field data and synthetic data generated by the modeling program is presented in Figure 3-5. The two are in excellent agreement. (The model image is for one item, so the effect of the second item in the field data shows up as a second anomaly in the image.)

In order to determine the minimum spacing between boreholes and the minimum spacing between measurements down-hole, anomaly maps were generated using different sets of borehole data. We found that a sample interval of at least one foot is required down the boreholes. Significant information about the smaller item (155 mm projectile) was lost when a z-spacing greater than one foot was analyzed. This effect is seen in the profiles shown in Figure 3-6, which were taken in Borehole C at Indian Head, Maryland. The minimum spacing required between boreholes was determined to be between 10 and 20 feet, depending in the size and orientation of the item.

Figure 3-5. Comparison of model (top) of MK82 to field data collected at Indian Head, Maryland.

GEO-CENTERS, INC.

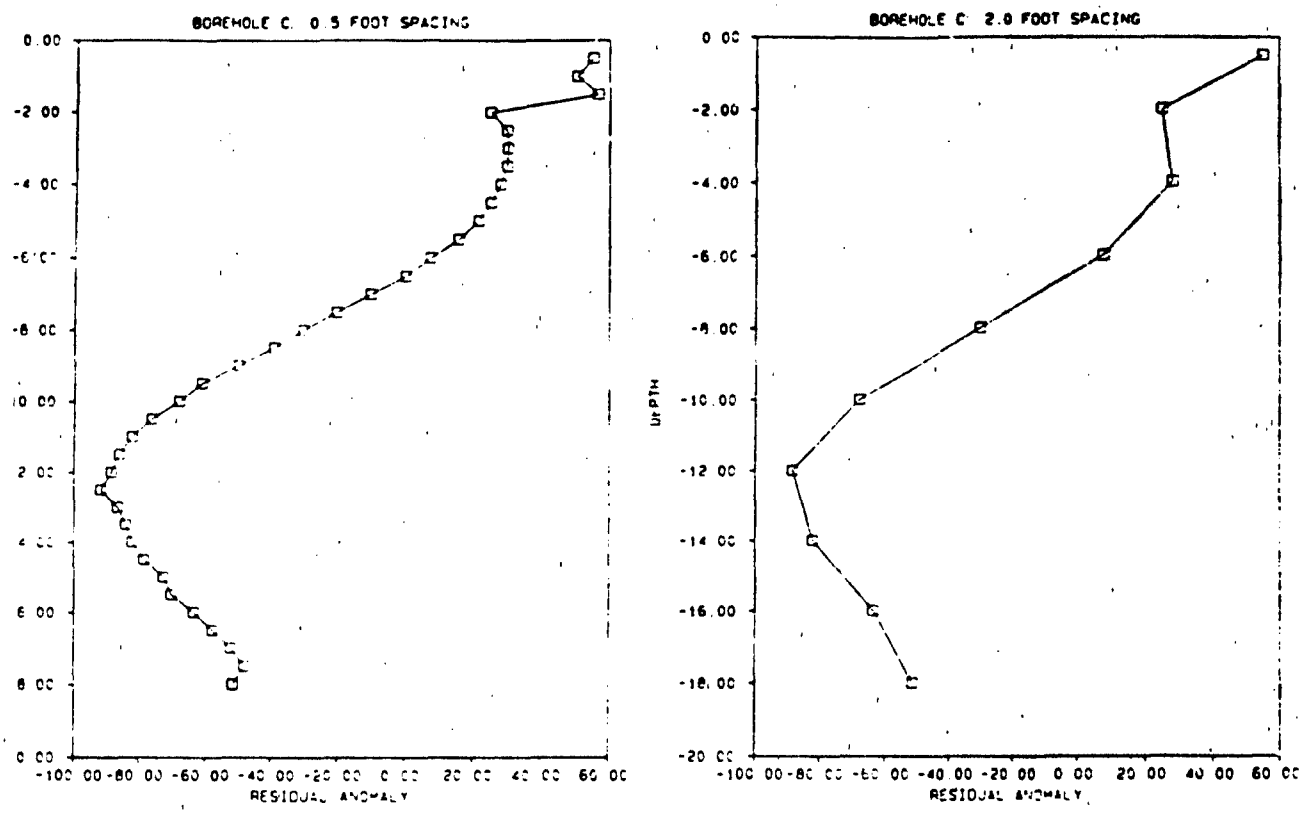

Figure 3-6. Comparison of total magnetic field borehole profiles. Profile A is plotted at 1/2 foot intervals, and Profile F is plotted at 2 foot intervals.

GEO-CENTERS, INC.

3.3.4.2 Fluxgate Data

Problems with calibration of the fluxgate magnetometer prevented computer processing of the data collected at the two test sites. Visual inspection of the records verified that the instrument is capable of detecting the buried ordnance when operating in the SD mode. The magnetic anomalies were more weakly registered in the data taken with the instrument in the SA mode. A comparison of the two types of data, taken in Borehole C at Indian Head, Maryland, is shown in Figure 3-7.

In conclusion, magnetometry is effective at detecting and locating deeply buried ferrous ordnance. Both techniques, the proton precession and the fluxgate, detected the ordnance buried at the two test sites. The proton precession technique is more effective, because it is more accurate (0.1 gamma) and it is not affected by vertical deflections in the borehole. It is slower, however, because readings take two seconds while the sensor is stationary. The fluxgate technique, while essentially instantaneous, is less accurate (10 gammas) and extremely difficult to calibrate. Since the fluxgate measures the component of the magnetic field aligned with the probe, variations in its vertical alignment in the borehole cause changes in the measurements, and therefore this technique is more problematic.

The cesium vapor sensor, the type used in STOLS, would be the optimum borehole magnetic system, considering it is capable of instantaneous, total field readings. A continuous profile could thus be obtained along a borehole. The difficulty in obtaining a commercial borehole version prevented us from testing this type of magnetometer during the scheduled field tests.

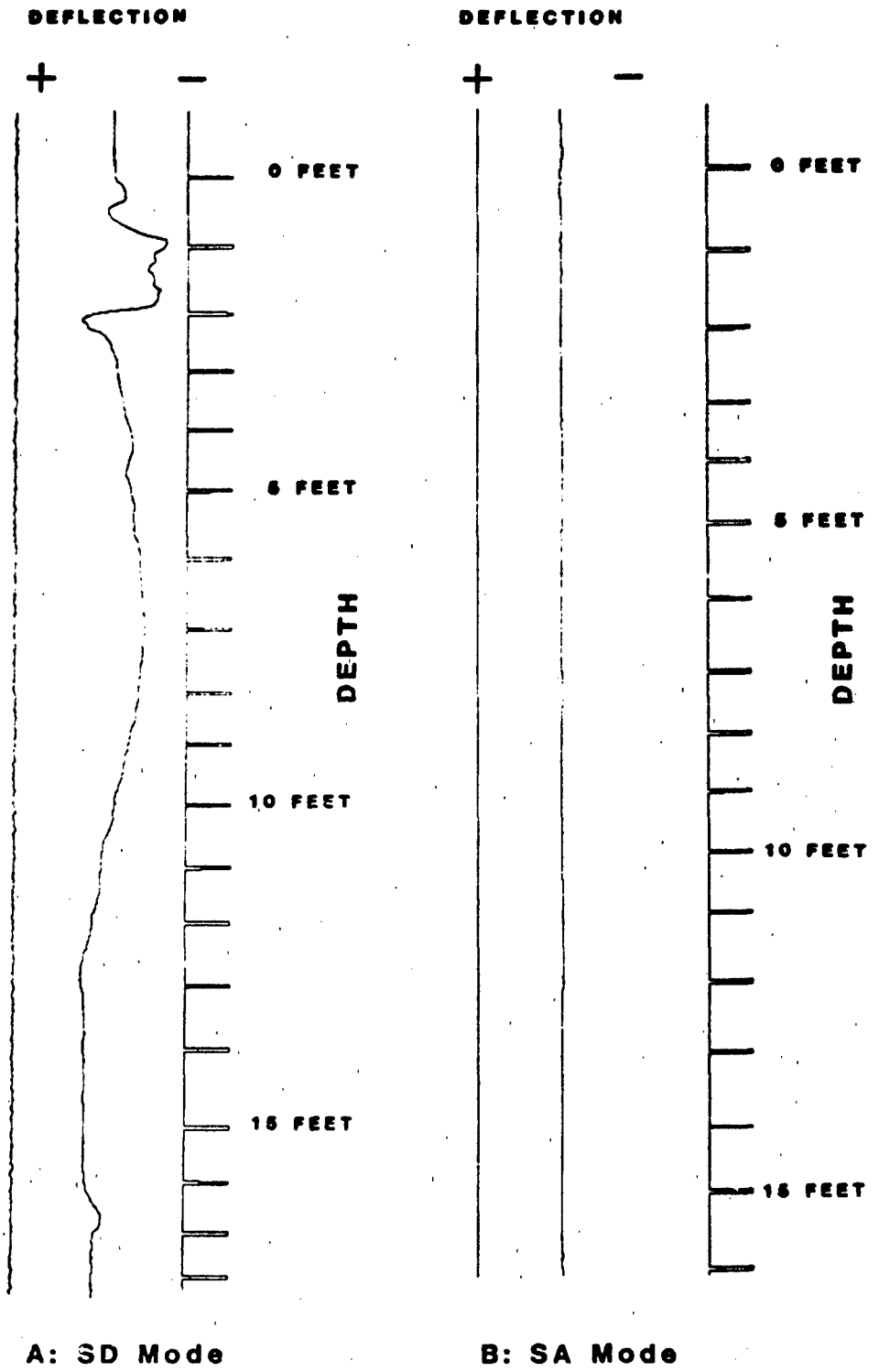

Figure 3-7. SA and SD mode profile recorded in Borehole C, Indian Head, Maryland.

GEO-CENTERS, INC.

3.4.0 ORDNANCE DETECTION USING GROUND PENETRATING RADAR

The application of ground penetrating radar (GPR) to the detection and location of deeply buried ordnance has been investigated. Beginning with the theoretical foundation for this technique, this section covers the development of a GPR data acquisition system, field experiments, and data processing techniques.

3.4.1 Electromagnetic Pulse Propagation

3.4.1.1 Theoretical Background

The principle of ground penetrating radar (GPR) involves the generation of a wavetrain of electromagnetic radiation in the frequency range of 10 to 1000 MHz. In accordance with the laws of classical electromagnetism, the wave propagates through the subsurface with material dependent attenuation. When the wavetrain encounters interfaces between materials of different electromagnetic properties, the wave is partially reflected. This reflected energy is then detected by the surface receiver, and the travel time between transmission and detection is recorded. If the velocity of propagation is known, the time interval measured can be converted into a distance. Appendix C provides a detailed description of electromagnetic pulse propagation through the earth.

A summary of the physical properties of common earth media which affect the propagation and attenuation of electromagnetic signals is shown in Table 3-1. Analysis of reflected radar pulses, combined with a knowledge of the electromagnetic proper-

TABLE 3-1

Approximate VHF Electromagnetic Parameters of Typical Earth Materials

Material	Approximate Conductivity σ (mho/m)	Approximate Dielectric Constant	Depth of Penetration
Air	0	1	Max (km)
Limestone	10^{-9}	7	↓
Granite (dry)	10^{-8}	5	↓
Sand (dry)	10^{-7} to 10^{-3}	4 to 6	↓
Bedded Salt	10^{-5} to 10^{-4}	3 to 6	↓
Freshwater Ice	10^{-5} to 10^{-3}	4	↓
Permafrost	10^{-4} to 10^{-2}	4 to 8	↓
Sand, Saturated	10^{-4} to 10^{-2}	30 to 50	↓
Freshwater	10^{-4} to 3×10^{-2}	81	↓
Silt, Saturated	10^{-3} to 10^{-2}	10	↓
Rich Agricultural Land	10^{-2}	15	↓
Clay, Saturated	10^{-2} to 1	8 to 12	↓
Seawater	4	81	Min (cm)

ties of the soil through which they propagate, provides information regarding location, depth, and composition of buried objects. For example, metallic objects have different electromagnetic properties than soils and give rise to strong reflections. Geologic interfaces give relatively weak reflections by comparison.

3.4.1.2 Radar Pulse Modeling

We have developed a model to analyze a radar pulse as it passes through dissipative media. The model computes the change in the radar pulse shape as a function of depth and varying earth characteristics. Details of the modeling efforts are described in the Borehole Progress Report for April [1] and June, 1986 [4].

The input pulse is assumed to be of a Gaussian shape and to have a pulse width of one nanosecond. Results have shown that the shape of the propagating pulse is directly related to attenuation effects of the media and to the more rapid attenuation of the higher frequency components than the lower frequency components. This causes a decrease of the pulse amplitude with time as well as a faster amplitude decay in wet earth than in dry earth. In addition, this amplitude decay causes the pulse shape to broaden and flatten with depth and it occurs more rapidly in wet earth. The pulse velocity for frequency components above 50 MHz does not change. Thus, the energy in the radar pulse does not appreciably disperse as the pulse propagates through the earth. A detailed description of electromagnetic pulse propagation through a medium is given in Appendix C.

The results obtained so far indicate that there is a high correlation in pulse shapes regardless of travel time. The study

of pulse shape variations assists in efforts to use an adaptive form of deconvolution to locate buried ordnance items.

3.4.2 Data Acquisition System

GEO-CENTERS assembled and fielded a computer-based borehole radar data acquisition system. The main elements of this system are the computer, the GPR electronics and the borehole antennas. A system block diagram is given in Figure 3-8.

3.4.2.1 Computer

The computer system utilized for borehole radar data acquisition is a Compaq Portable 286, which has a built-in monochrome display, 360 KByte 5-1/2 inch floppy drive, 20 MByte hard disk, and RS-232 I/O port. The Compaq has expansion slots to accommodate optional circuit boards. When used for radar data acquisition, the computer runs on a custom disk operating system, P-DOS, developed in-house to overcome limitations in real-time data storage created by MS-DOS file structure. The computer links to the GPR electronics through a GEO-CENTERS' X-BUS installed in one of the expansion slots. A user-selectable, menu-driven computer program, RADARAQ, automates the data acquisition.

3.4.2.2 Electronics

At the heart of the GPR electronics is a commercial system manufactured by Geophysical Survey Systems, Inc. (GSSI): the GSSI System 7 SIR, comprising the SIR 400 Control Unit and SIR 7000 Display, transmit/receive modules, and an EPC gray scale plotter. Two electronic modules were designed and built in-house to interface the GPR with the computer. These are an X-BUS/Digitizer,

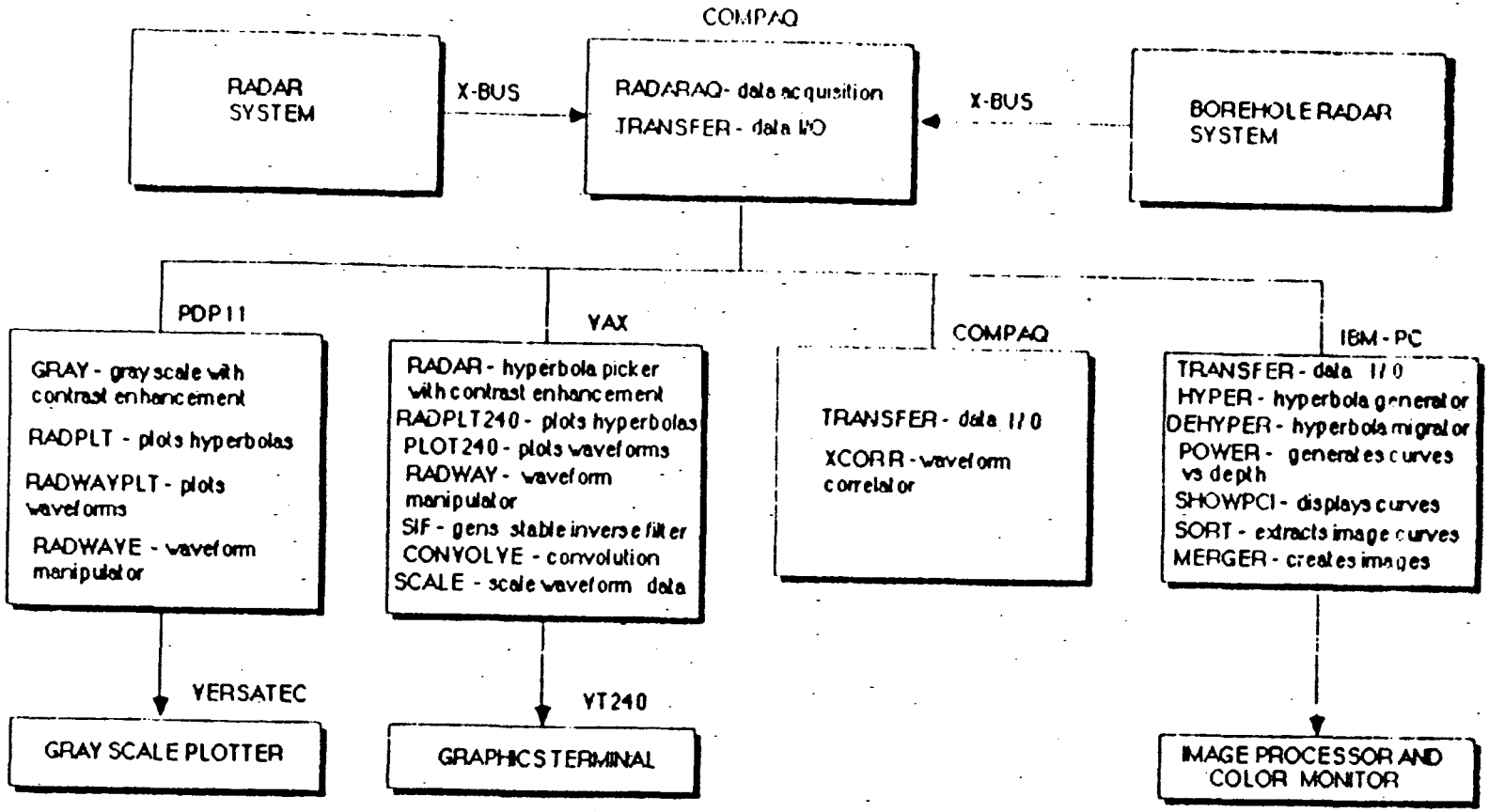

Figure 3-8. Block diagram of the borehole radar system.

which converts the GPR analog signal to 8-bit digital data, and a DMA Timer, which synchronizes the transfer of the real-time data to the computer. This system achieves average data storage rates of 16 KBytes per second and instantaneous rates of 50 KBytes per second. Details are contained in Section 4.4.2 (Radar) of this final report.

3.4.2.3 Antennas

Borehole radar tests were conducted using an available GSSI borehole antenna and a GEO-CENTERS antenna. Tests at Indian Head indicated that the resolution of the GSSI antenna was insufficient to detect the buried ordnance, as shown later in Figure 3-11. The problem is the low operating center frequency (120 MHz) of the antenna. For the soil type at the site, this gives an estimated minimum resolution of 0.3 meter, which is insufficient for detection (Borehole Progress Report, April, 1986 [1]). Resolution can be improved by increasing the frequency of operation. To this end, GEO-CENTERS designed and constructed a borehole antenna which operated on a center frequency of approximately 210 MHz. The design used two tapered conductive elements fitted into 3 inch diameter fiberglass tube sealed at the ends with PVC caps. A drawing of the tapered element antenna is presented in Figure 3-9. This design was tested at the test sites at Indian Head, Maryland and CRREL, Alaska. Results on this design were inconclusive because the native soil at Indian Head severely attenuated the radar signals, and the boreholes at the CRREL site were too small in diameter for the antenna casing. On-site modifications of the antenna housing disrupted their normal operation and prevented valid testing.

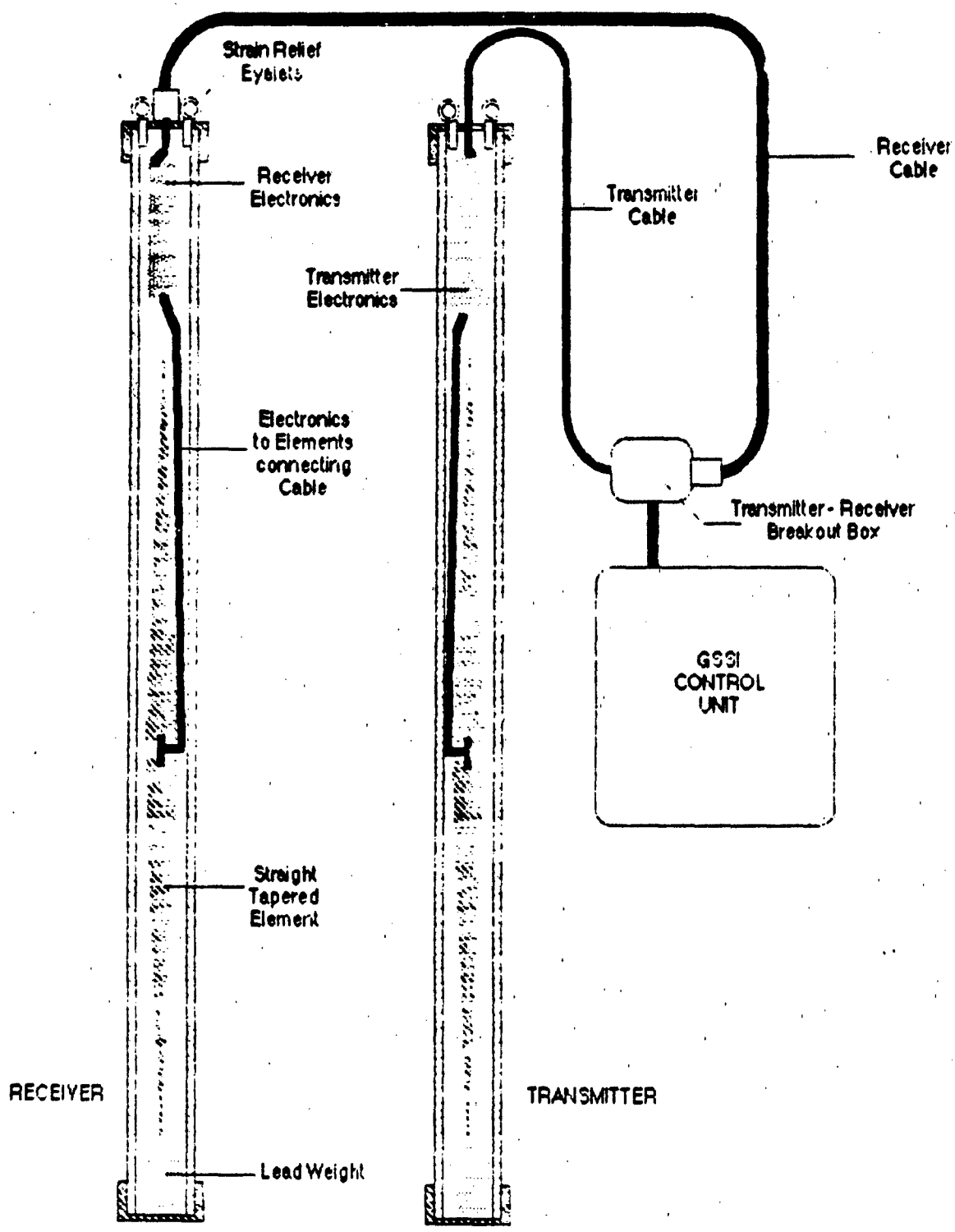

Figure 3-9. GEO-CENTERS drawing of tapered conductive paper element borehole antenna.

3.4.3 Field Experiments

A series of experiments was designed to investigate the source-receiver characteristics of borehole radar antennas and to assess their ability to locate buried ordnance in different soil types. Based on the theory of electromagnetic scattering, briefly summarized in Section 4.2.3 (Radar), three types of experiments were designed: monostatic reflection, cross-hole reflection and tomography.

3.4.3.1 Monostatic Reflection

Monostatic reflection, in which purely reflected signals are recorded, used a single transceiver down one borehole. The transceiver was lowered at a steady rate, with fiducial marks inserted in the records at one foot intervals. This method is diagrammed in Figure 3-9. A total of 19 downhole scans were collected with this method. Close inspection of the data revealed no evidence of reflections from the target at the expected depth. An example of the data is shown in Figure 3-10. The absence of an identifiable target in the data is believed to be due to the lack of sufficient resolution achieved with the relatively low frequency commercially available antenna.

3.4.3.2 Cross-hole Reflection

In cross-hole reflection the subsurface is imaged by both direct and scattered energy. Separate transmit and receive antennas were lowered simultaneously in selected borehole pairs. A diagram of this method is shown in Figure 3-11. A total of 39 scans were recorded uring this method at the two test sites. An example of the data is shown in Figure 3-12. Preliminary analysis

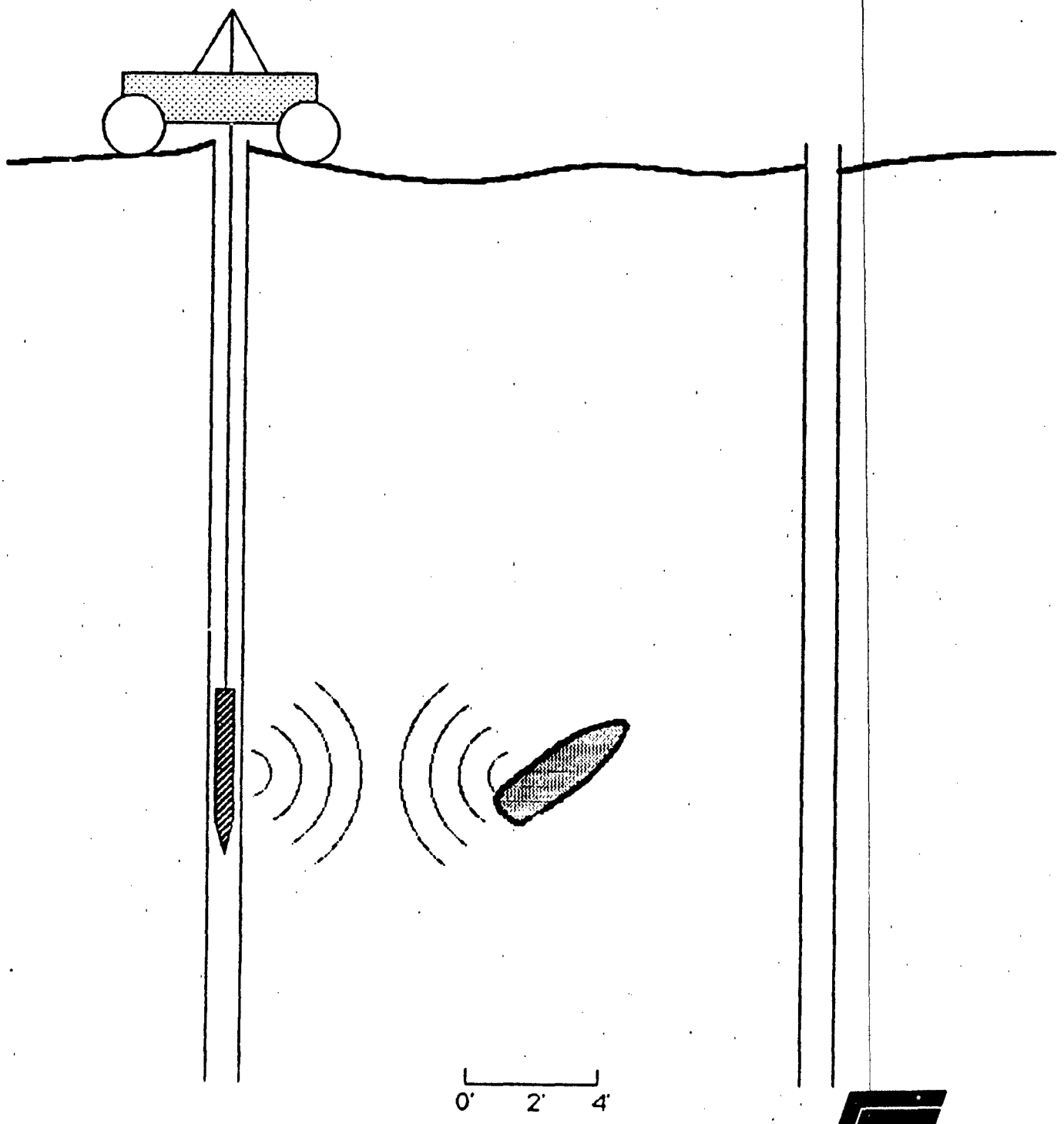

Figure 3-10. Monostatic reflection method.

GEO-CENTERS, INC.

Figure 3-11. Monostatic reflection profile recorded in Borehole I, Indian Head, Maryland. No evidence of target MK-82 can be seen.

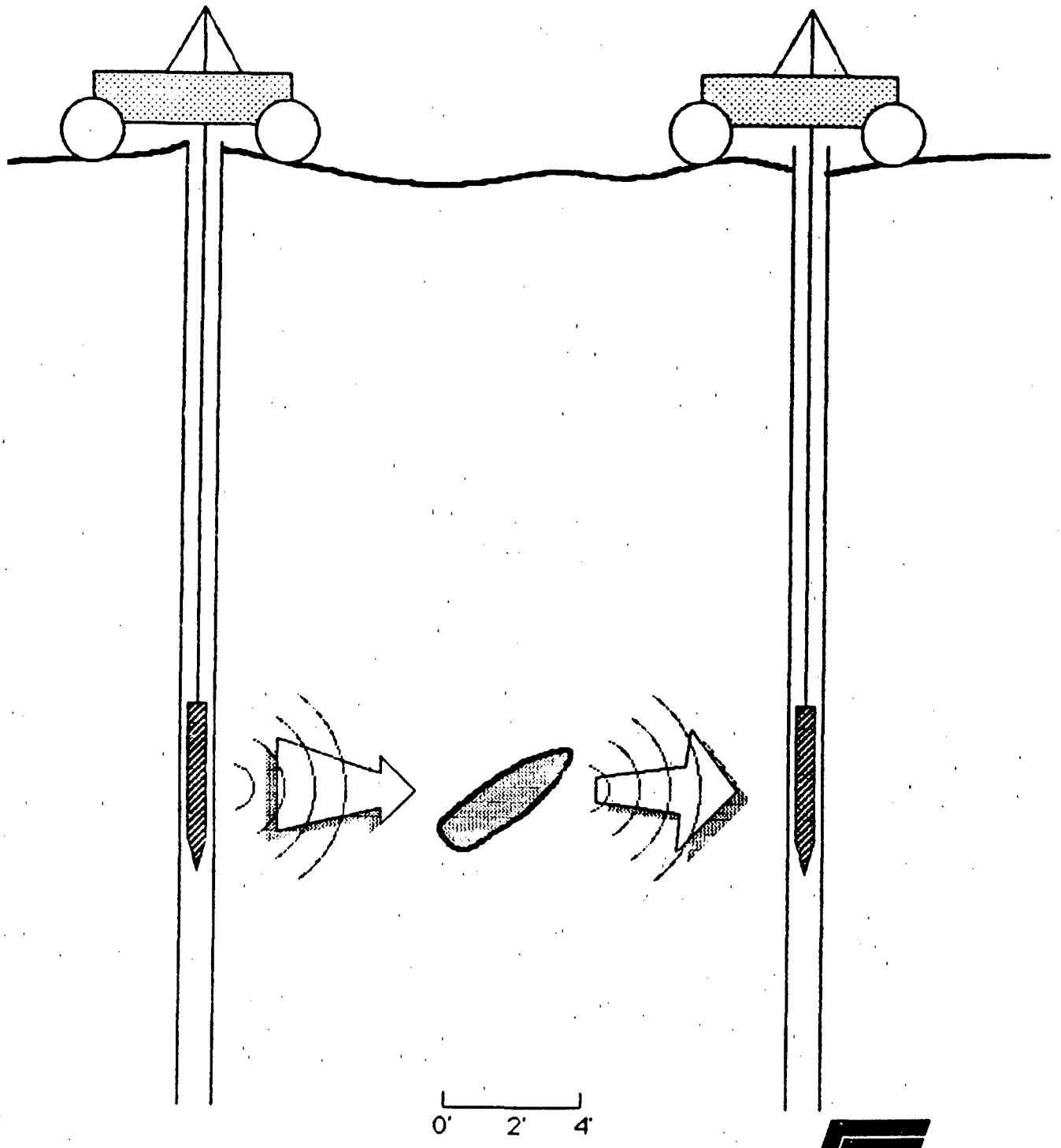

Figure 3-12. Cross-hole reflection method.

GEO-CENTERS, INC.

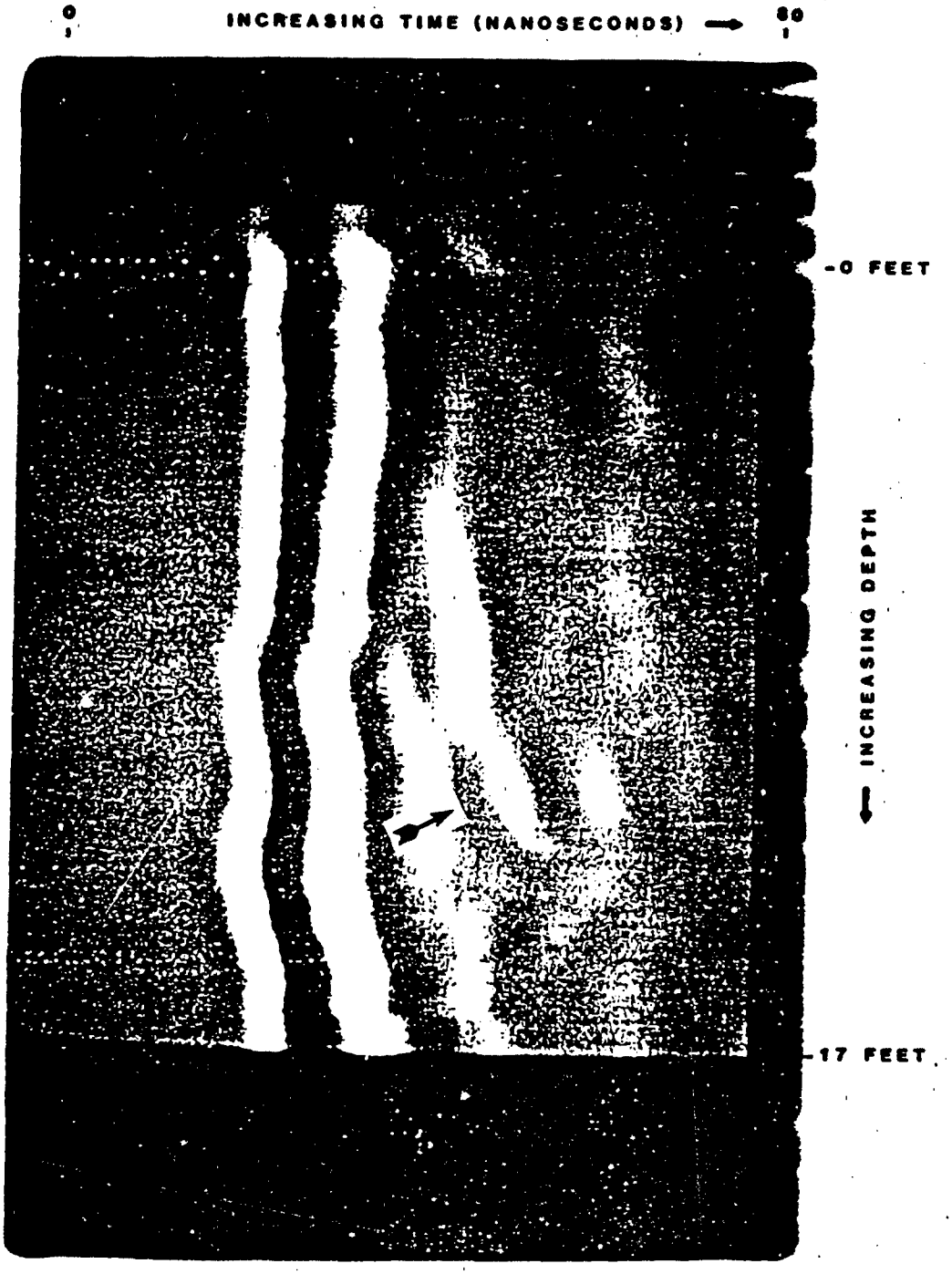

Figure 3-13. Cross-hole reflection data, Boreholes I and H, Indian Head, Maryland. Possible target indication, MK82, is shown at arrow.

GEO-CENTERS, INC.

of the records confirmed target detection in a few cases. The evidence is not conclusive, however, due to the low amplitude of the reflected signals in the data caused by the highly attenuating clay soil.

3.4.3.3 Tomography

Tomography is an imaging technique based on mapping the received signal along a ray path. A cross-section image is formed when the plane area between two boreholes is traced with overlapping multiple ray-paths between the transmitter in one hole and the receiver in another. A diagram of the geometry involved in the method is given in Figure 3-14. These experiments were performed by holding the receiver fixed in one hole and moving the transmitter in another. The receiver was lowered to a different position, and the process was repeated A total of 102 scans were taken using this method, between a total of 6 borehole pairs. An example of the data is presented in Figure 3-15. Preliminary examination of the data indicates that tomography holds promise to detect and locate deeply buried unexploded ordnance. However, additional development in data processing and imaging techniques is required in order to confirm the validation of this method.

The data acquisition system performed extremely well under field conditions. For the Indian Head tests, the quality of the borehole radar data from both the GSSI and GEO-CENTERS antennas was, as expected, poor. The natural clay soil in that region is known to severely attenuate radar signals. The signal to noise ratio in the data is very low. Moreover, the operating frequency of the GSSI antenna is too low to provide the resolution necessary to detect buried ordnance items. Plans had been to use the GEO-CENTERS tapered element antenna at the CRREL test site to

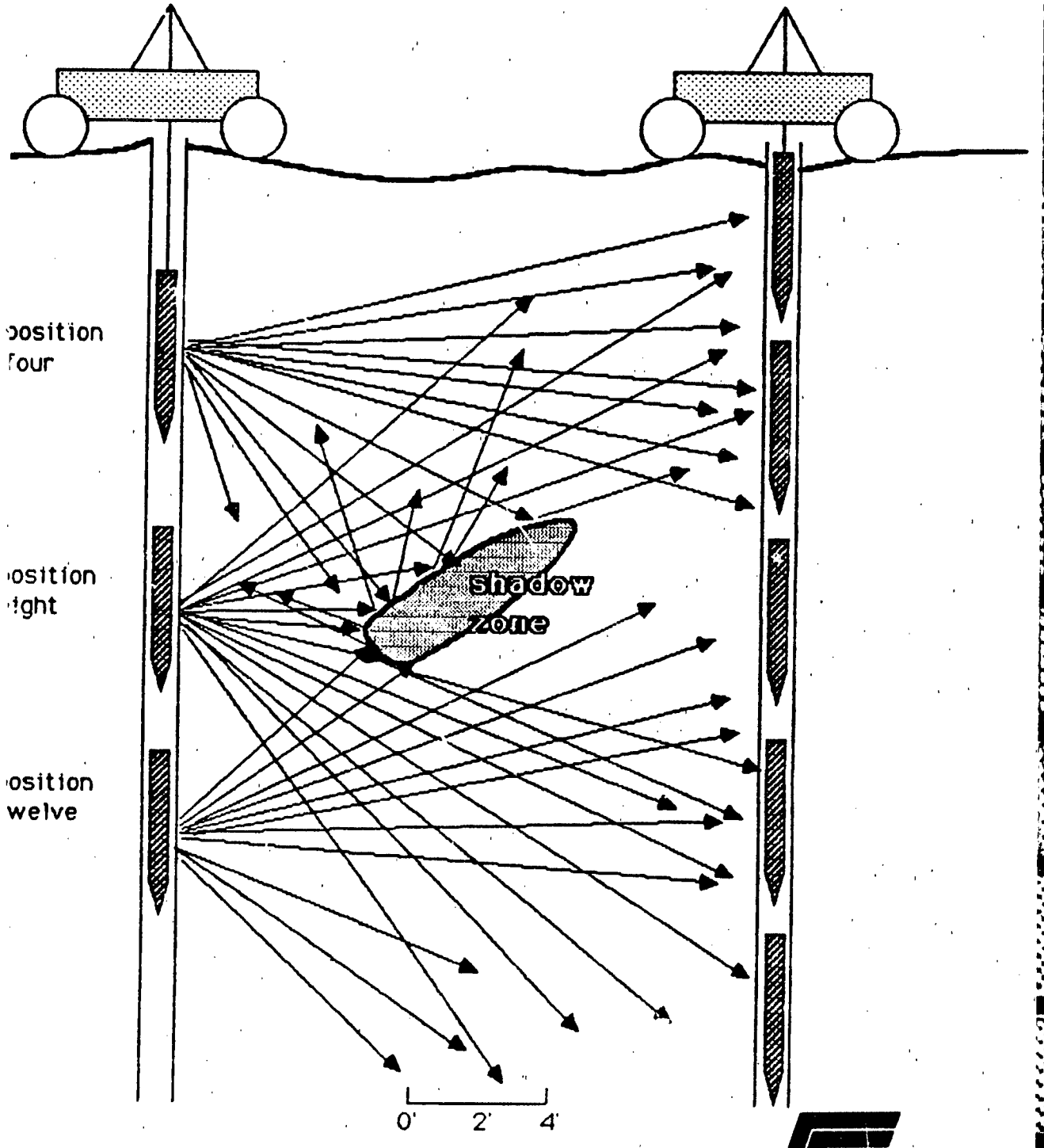

Figure 3-14. Tomography data collection.

GEO-CENTERS, INC.

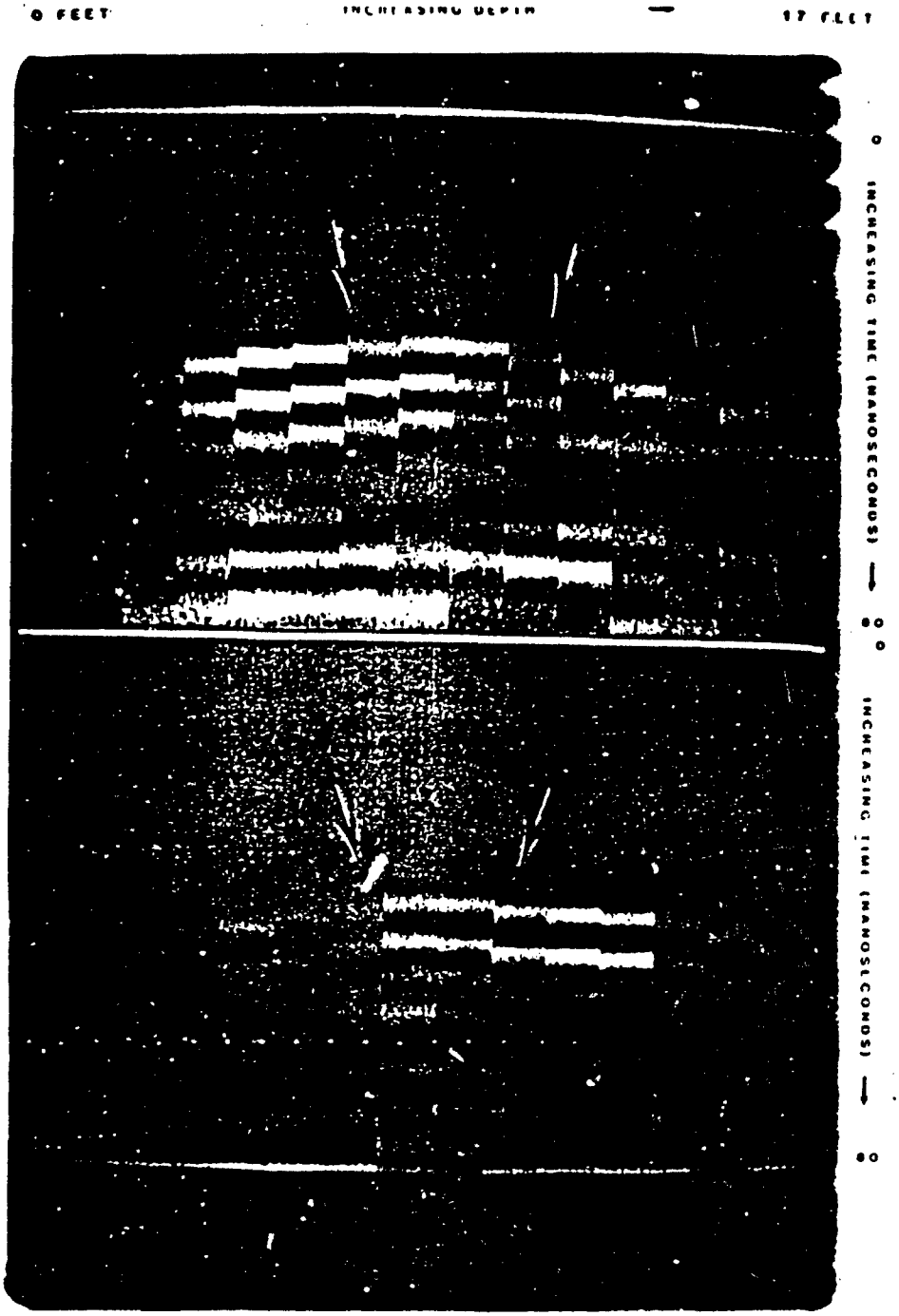

Figure 3-15. Sample tomography data collected at Indian Head. Top portion has receiver at 11 feet below the surface. Bottom has receiver at 9 feet. Diminished intensity caused by presence of bomb is indicated by the arrows (arrows outline the shadow-zone).

obtain higher resolution borehole data. However, the boreholes were too small in diameter for the antenna casing. Attempts to modify the antennas on-site disrupted their normal operation.

In conclusion, field experiments did not provide an opportunity to test the performance of the GEO-CENTERS tapered element antenna.

3.4.4 Signal Processing

The application of signal processing techniques to borehole radar improves target detection capabilities. These techniques increase the signal-to-noise ratio (SNR) in the data to enhance reflections off targets.

Trace stacking, which improves the SNR by enhancing coherent signals, is implemented in GEO-CENTERS' radar data acquisition software. The radar images in Figures 3-11 and 3-13 above have been stacked with no loss of information. This is done by summing corresponding data points in adjacent traces and dividing by the number of traces (see Appendix D for details). Noise tends to be incoherent and, therefore, will cancel in summation. The improvement in the SNR is a factor of SQRT(N)/N, where N is the number of traces stacked.

Convolution and deconvolution algorithms were tested with little success on the borehole radar data. The convolution and deconvolution algorithms are discussed in Appendix D.

Waveform filters were tested and designed to discriminate against a particular input, usually frequency. An example of this is the bandpass convolver shown in Figure D-2 in Appendix D. This

bandpass filter discriminates against the high frequency noise present in an unprocessed waveform.

In conclusion, several signal processing techniques have been applied to borehole radar data. These include stacking, filtering and deconvolution. The stacking and filtering algorithms have been shown to be effective in increasing the SNR.

3.5.0 DRILLING PLATFORM

3.5.1 Borehole Drilling Technologies

Drilling platform requirements need to be carefully defined in order to accomplish borehole range clearance efforts. Some of the common types of drilling methods used for borehole installation are: cable tool, hydraulic rotary, air rotary, auger, jet drilling, wash and drive, and driver points. These methods were compared and their relative advantages and limitations assessed. The factors used to evaluate these techniques for range clearance were: drill rig availability, mobility, depth range, speed, drilling fluids introduced, hole size, and relative cost per hole.

Table 3-2 presents a comparison of drilling methods. Two methods, augering and rotary drilling, are possible candidates. A brief descriptive summary of these two techniques is given below.

3.5.1.1 Auger Drilling

Solid stem continuous flight augers bore holes by "screwing" an augered bit into the ground. This process is illustrated in Figure 3-16. The cuttings are brought to the surface by the rotary flights. Auger bits are of two types: fishtail or drag bits for unconsolidated materials, and claw bits for lithified or cemented soils. Once the desired depth is reached, the auger is rotated until the hole is cleaned out.

This method works best in loose unconsolidated sediments. Auger drilling rigs are generally mobile, rapid, and inexpensive to operate. This method cannot be used to drill in rock.

Table 3-2. Comparison of Drilling Methods.

	Wash & Drive	Drive Points Jetting	Auger (Solid) (Hollow)	Cable Tool	Hydraulic	Rotary Air	Special Reverse
Availability	Good	Good	Good	Good	Good	Low	Low
Mobility/Access	Very Good	Very Good	Good	Good	Good	Poor	Low
Max. Depth Range	200 ft.	100-150 ft.	100-150 ft.	500-1000 ft.	1000+ ft.	1000+ ft.	1000+ ft.
Casing Requirements	Yes	N/A	No/Integral	Yes	No	Yes	No
Speed	Slow to Moderate	Fast	Fast	Slow	Moderate	Very Fast	Moderate
Drilling Fluids: Soil	Water	None/Water	None	Small Amounts	Mud	Air	Mud
Hole Size	2-6 inches	2 inches	6 in./8 in.(3)	4+ inches	2 3/8-6 inches	6+ inches	6+ inches
Relative Cost	Low	Low	Moderate	Moderate	Moderately High	High	Very High

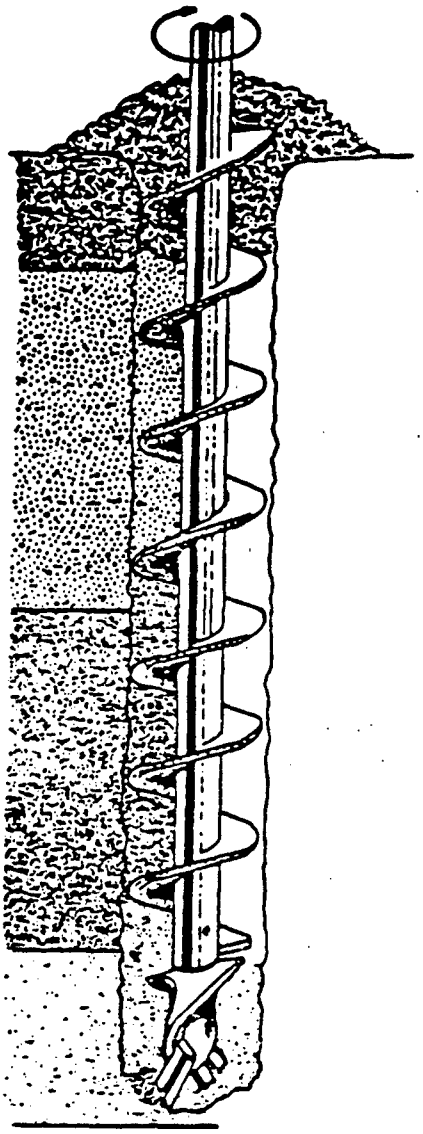

Figure 3-16. Continuous flight auger drilling. The contiuous-flight auger bores into the soil and rotates the cuttings upward along the flights. The uppermost cuttings are discharged at the surface to make room for the space of the auger as it penetrates additional soils [5].

3.5.1.2 Rotary Drilling

Rotary drills operate by pumping fluid, either water or air, down the center of the drill stem which is rotated under pressure to bore the hole. The fluid lubricates and cools the drill bit and flushes cuttings to the surface along the annulus created by the stem. This process is illustrated in Figure 3-17.

Rotary drill rigs are the most commonly available. They are very rapid, mobile, and can drill in any type of soil or rock.

In conclusion, both auger and rotary drilling methods would work for borehole ordnance clearance. Because of mechanical simplicity and relative low cost, auger drilling is the method of choice for the borehole ordnance detection system.

Outright purchase of a drill rig requires that the NAVEOD-TECHCEN assume all costs such as general maintenance, repairs, drill bits, drill piper, auger stems, and fuel. It also requires that skilled operators be hired and trained. The drill rig must also be transported to sites around the country.

Contracting through local well drillers has many advantages over outright purchase of drill equipment. The process of competitive contracting results in lowest possible costs. Bids can be on a cost-per-foot or cost-per-hole basis; the cost per hole has been quoted at $250 at the Indian Head, Maryland test site. Also, since drillers can have several types of rigs available to them, this allows for versatility on meeting site specific drilling requirements.

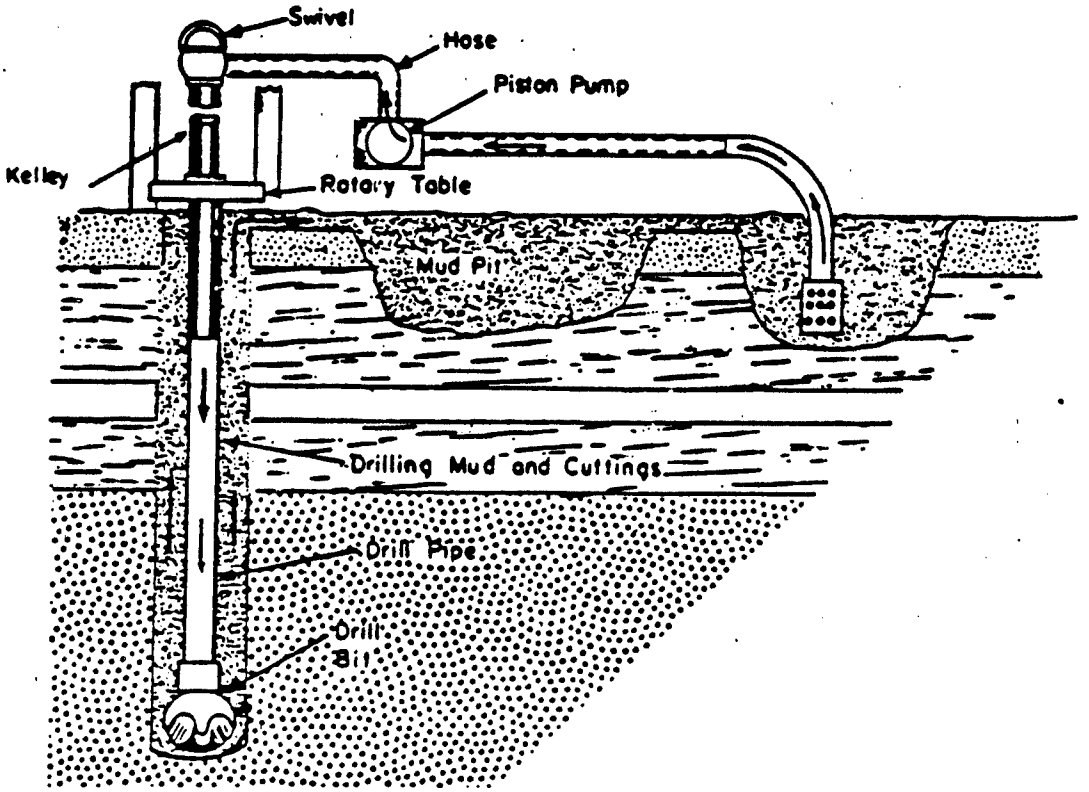

Figure 3-17. Mud rotary drilling. The drilling fluid (or water) is pumped through the swivel and down through the kelley which is turned by the rotary table. The mud then flows down through the drill pipe, out through the bit, and back up the hole carrying cuttings which settle out of the mud in the first section(s) of the mud pit [5].

3.5.2 Navigation Systems

A navigation system is required to accurately locate boreholes with respect to an established ground control grid. This includes position with reference to a local coordinate system and accurate depth determination of the sensor. The coordinates are used in data processing.

The discussion on navigation systems in Section 2.4.3 (STOLS) of this report is directly applicable to borehole work and is not reproduced here.

3.6.0 SUMMARY AND CONCLUSIONS

This project identified two practical and effective methods for the detection and location of buried ordnance: magnetometry and ground penetrating radar.

Hardware was developed to acquire magnetometry and radar data at two specially prepared test sites; one at Indian Head, Maryland, and the other at CRREL, Fairbanks, Alaska. Field tests at these sites demonstrated the feasibility of collecting borehole data with a computer based data acquisition system.

Borehole magnetometry has been shown to be effective at detecting deeply buried ordnance at both sites, and based on the results of the field tests, total field magnetometers are selected as the sensor of choice.

Ground penetrating radar gave mixed results, as expected, for use in borehole detection. Based on the experience in the field and analysis of the data obtained, areas of improvement for increasing radar effectiveness have been identified. These include modifying available antennas to operate at higher center frequency, thereby increasing resolving power, and refining radar signal processing algorithms to improve the signal-to-noise ratio and to enable tomographic mapping.

References

1. GEO-CENTERS, INC. Monthly Progress Report for April, 1986, prepared for NAVEODTECHCEN, Indian Head, Maryland.

2. GEO-CENTERS, INC. Monthly Progress Report for January, 1986, prepared for NAVEODTECHCEN, Indian Head, Maryland.

3. GEO-CENTERS, INC. Monthly Progress Report for February, 1986, prepared for NAVEODTECHCEN, Indian Head, Maryland.

4. GEO-CENTERS, INC. Monthly Progress Report for June, 1986, prepared for NAVEODTECHCEN, Indian Head, Maryland.

5. Scalf, M.R., et. al., Manual of Ground-Water Sampling Procedures, National Water Well Association, Worthington, Ohio, 1981, 93 pp.

SECTION 4

GROUND PENETRATING RADAR FOR ORDNANCE LOCATION

TABLE OF CONTENTS

TABLE OF CONTENTS (cont.)

LIST OF FIGURES

4.1.0 INTRODUCTION

4.1.1 Use of Radar

Subsurface radar detection systems have been the object of study for over a decade by both military and environmental agencies. In both applications, the objectives are to locate and identify buried or submerged objects, otherwise not detectable, and to determine spatially the structural make-up of the subsurface.

Systems generally consist of antennas towed over the surface with data recorded for subsequent analysis. Depths of penetration are dependent on local geology and can range from one to hundreds of feet. Tradeoffs can be made between penetration and resolution. For the purposes of range clearance, targets to be detected may be as small as an 60mm rocket propelled grenade or as large as an MK82 500 lb. bomb. For these resolution requirements, ground penetrating radar (GPR) can be expected to detect ordnance to a depth of up to 15 feet.

4.1.2 Overall Program Goal

The goal of the overall program is to design and construct a fieldable GPR system suitable for range clearance by military operators.

The currently available commercial GPR systems consist of one of several different frequency antennas controlled by an analog sampling system with tape storage and graphic recorder output. It requires trained personnel to both operate and interpret the data.

The technology needs to be advanced to the level where a system can be implemented using arrays of directional radar antennas and advanced electronics to provide wide area coverage, increased signal strengths and deeper penetration, as well as automating data interpretation through the application of computer processing techniques.

4.1.3 Task Identification

Improvements in many areas will lead to a technology advanced enough to warrant use in a range clearance scenario. These areas can be identified by examining each major element of a GPR system and specifying tasks where improved technology can be applied. Areas for improvement can be targeted as follows:

- Antennas - Develop small, lightweight directional antennas suitable for mounting as an array on a boom.

- Data Acquisition & Storage - Examine the constraints imposed by ordnance detection requirements and reduce complexity and training required for equipment operation. Employ the use of high speed digital data acquisition and storage. The use of open architecture and industry standards will allow straightforward implementation of robust, state-of-the-art hardware while providing an upgrade path for future enhancements such as real time digital signal processing.

- Data Analysis - Employ computer processing of data. Examine single and multichannel data processing techniques and evaluate their effectiveness for use with radar data. Develop image processing and pattern

recognition algorithms for automation of data analysis and ordnance detection.

4.1.4 Program Accomplishments

In performance of these tasks, the following specific accomplishments were achieved:

- Antennas - Designed and built 900 MHz V-antenna and 450 MHz tusk antenna. Evaluated antenna materials. Performed antenna configuration and polarization experiments.

- Data Acquisition and Storage - Designed, built, and fielded interim radar system, performing real time digital data storage from GSSI system. Digitized previously acquired data and added to catalog of ordnance target signatures. Specified design of multichannel GPR system which will allow acquisition of array data.

- Data Analysis - Evaluated antenna frequency vs. detection effectiveness. Prepared catalog of data from field tests at Fort Polk, Indian Head, and Alaska. Developed hyperbolic pattern recognition program. Evaluated signal processing algorithms, single and multichannel. Developed image processing techniques. Collected and evaluated synthetic array data. Aided in design and construction of field test pit at Indian Head.

For the purpose of performing the tasks described above, it is important to understand the operation of time domain radar systems. This is described in the next section, with following sections providing details on the developments made in antennas, data acquisition, data processing, and associated field experiments.

4.2.0 THEORETICAL BACKGROUND

4.2.1 Introduction

GPR is an effective tool when local geology is favorable - about 50% of the time. It is possible to predict at a field site when GPR should be utilized by understanding the effects of soils on electromagnetic propagation and, more specifically, on a pulse viewed in a time domain system. The constitutive parameters describing electromagnetic propagation are discussed in detail in Appendix C, as are soil models and the theory concerned with electromagnetic propagation in the earth.

4.2.2 Overview

In a time domain GPR system, a Gaussian pulse is coupled into the earth and the backscattered energy is sampled with respect to time. A Gaussian time domain pulse has an essentially flat spectrum over the range of frequencies used in GPR. Transmitting this pulse through an antenna filters it, radiating some bands of frequencies and damping others. Coupling this antenna into the ground can change the antenna's filtering properties, as can various antenna designs and configurations.

Once the pulse is in the earth, the earth both filters it and slows it down. Different types of earth have different effects on the pulse, but, in general, high frequencies are attenuated more rapidly than low frequencies. Attenuation of the signal is primarily a function of the conductivity of the soil (which generally increases with increasing frequency). Velocity is related to earth electrical properties, primarily the dielectric constant ε =

$\varepsilon_o\varepsilon_r$. Changes in these parameters are usually associated with changes in local geology, such as soil layers, rock layers, water tables, etc., and cause a portion of the pulse to be reflected back. Figure 4-1 shows depth of penetration as a function of attenuation for various frequencies and dielectric constants. The reflected signal is delayed by an amount equal to the time from initiation of the pulse to time to reach the reflecting interface and then back to the surface. Half this round trip time can be multiplied by the average velocity of propagation in the soil to determine distance from the surface to the reflecting interface.

The resolving power of GPR is determined by the wavelength in the earth. Since GPR uses a broadband pulse, the wavelength is generally determined with respect to the center frequency of the spectrum radiated by the antenna, with 1/2 the wavelength approximately defining the smallest detectable object. For the purpose of detecting ordnance, ideal center frequencies lie from 300 MHz to 1000 MHz. Although lower frequencies are commonly used and provide deeper penetration, they fail to provide enough resolution. Higher frequencies are generally not used because of signal attenuation.

It is possible to use two different antennas to obtain two different resolutions and depths of penetration. Because smaller ordnance items (such as small projectiles or mortar rounds) generally remain within the first few feet of the surface, it may be desirable to use a higher frequency antenna for shallow range clearance with increased resolution. Large ordnance items (such as MK81 or MK82 bombs) may be buried over 10 feet below the surface, requiring more penetration but less resolution because of their larger size.

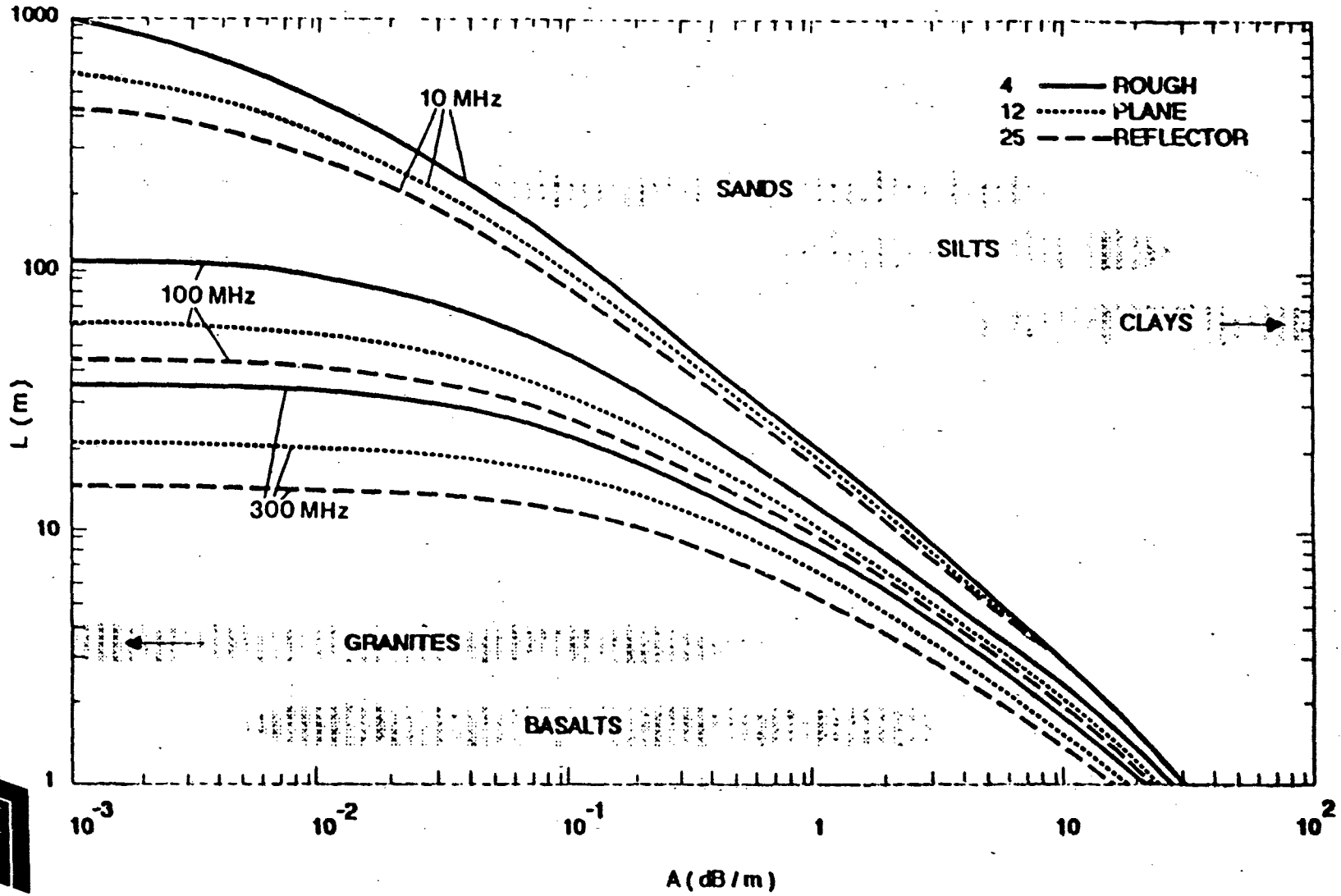

Figure 4-1. Variation of maximum depth of penetration (L) as a function of attenuation (A) for different frequencies and dielectric constants. Typical ranges of attenuation for different earth materials are also shown.

GPR data are generally analyzed in grey scale image form. The image is created by displaying pulse return waveforms adjacent to each other, with two-way travel time on a vertical scale. As a scan progresses along the surface, returns from subsurface reflectors create features in the image, which are flat for plane reflectors and hyperbolic for point reflectors.

4.2.3 Electromagnetic Scattering

In order to interpret radar images, an understanding of the effects of electromagnetic wave scattering off targets is required. The following is a basic description of the principles involved.

A scattering system consists of an incident field (E^i,H^i), a target or obstacle, and a probe which samples the total field consisting of the incident field and scattered field (E^s,H^s) where

$$E = E^i + E^s$$
$$H = H^i + H^s \qquad (1)$$

Usually remote scattering measurements are made at the source, or incident field location. These are called monostatic or backscattering measurements. Scattering in other directions is called forward or bi-static scattering. Single frequency systems are concerned with steady state scattering. Time domain systems using narrow band temporal pulses, like ground penetrating radar (GPR), are concerned with time domain scattering. The time domain (TD) and frequency domain (FD) scattering problems do not have a distinct boundary. Steady state FD scattering results can give insight into TD systems. Steady state scattering results for the

center frequency region of a TD system can give a good first approximation to the TD scattering solutions. This comes about because the TD system can be decomposed into its FD spectral components. Superposition of the individual spectral results leads to a total TD solution. Since the center frequency of the TD pulse is dominant, it dominates the results.

Insight intc distributions of scattered field can be gotten from the limiting cases of the low and high frequency results. The former corresponds to the case when the wavelength (λ) of the incident field is large compared to the size of the obstacle (L). The latter case corresponds to the case where the wavelength is small compared to the size of the scatterer. Results for these two cases are described below. Attention is focused here on metallic scatterers:

Case I $\lambda > > L$

Here, since the scatterer is small compared to the wavelength of the incident field, only a small amount of the incident field or energy is scattered. Scattering in this regime is essentially isotropic meaning that scattering energy is uniformly distributed in space.

Case II $\lambda < < L$

When the object is large compared to the wavelength, only the specular scatter is important. This result is similar to that of optics where light reflection from mirrors is a specular phenomena. In this case, large amounts of energy can be reflected in the specular direction.

When the wavelength is of the order of the size of an object the situation is more complex. An example will be given here to show the major results for this regime. In Figure 4-2 taken from King [King, R.W.P. and Wu, T.T., "The Scattering and Diffraction of Waves", Harvard University Press, 1959] a plane electromagnetic wave is scattered from a cylinder whose electrical radius is about a half wavelength. The dashed and dotted lines show the maxima and minima of the electric field. A good way to visualize the phenomena is to imagine the surface of a long narrow rug which has been bunched up to a cylindrical post. Note that in addition to the backscattered field, a field has been scattered in the forward and intermediate directions. This diffracted field has a pattern which depends on the size of the scatterer. For some size scatterers, little field is sent in the forward direction, for others appreciable forward scatter is present.

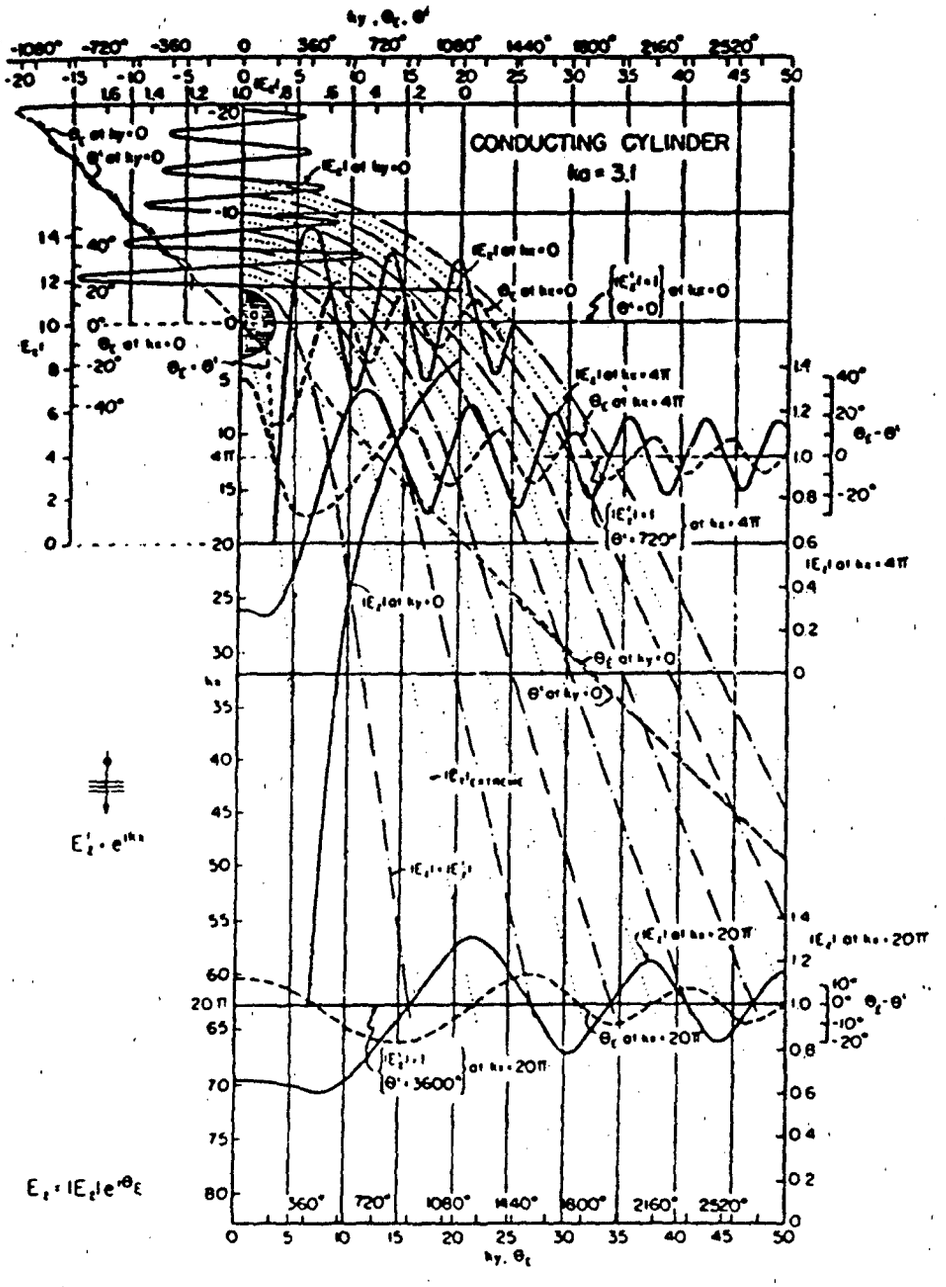

Figure 4-2. Electric field $E_z = |E_z| e^{i\theta E}$ near a conducting cylinder when the electric field is parallel to the axis of the cylinder; Ka = 3.1. From King and Wu [1].

4.3.0 ANTENNAS

4.3.1 Introduction

The antenna is the transducer responsible for coupling the electromagnetic pulse into the ground. The primary requirement of a time domain (TD) antenna is that it must be broadband; it must have a constant matchable impedance over a range of frequencies from about 10 MHz to 1000 MHz. If the impedance is not constant, distortions will occur in the pulse which can render the signal difficult to use, if not useless.

Traditional GPR systems have used a bow-tie dipole resistively loaded at the ends. Although this is a very efficient broadband radiator, which can be used successfully for ordnance detection and location; it has several limitations. One is that it is an almost omnidirectional antenna, meaning the radiation pattern extends well off to the sides in a hemispherical pattern, hindering clutter discrimination. It also has a very low front to back ratio, radiating a substantial amount of energy above the antennas into the air instead of into the ground. This results in "ghost" data from above surface reflectors such as chain link fences, trees, and power lines. This data can often be recognized and dismissed by trained operators, but for an automated system it would be necessary to program a computer to reject this information. Efforts at shielding the top surface to prevent back radiation have had some success but increase the size and weight of the antenna considerably. For the desired use in an array configuration, several improvements to the traditional bow-tie antenna would prove beneficial. For these reasons, GEO-CENTERS applied previous experience with low frequency time domain antennas to

design and build a broadband, directional, lightweight antenna with a high front-to-back ratio, suitable for use in an array.

4.3.2 Antenna Development

Development of GPR directional antennas involves many different tasks. GEO-CENTERS time domain (TD) antennas for GPR are generally related to the reflectionless antennas of Wu and King [1]. For GPR use, GEO-CENTERS has developed a special material for the practical realization of the reflectionless design. In addition, new geometrical shapes were involved allowing vastly increased directionality without sacrificing efficient coupling of the radiated waves into the earth. The basic configuration of the directive TD antennas is a continuously loaded dipole in which the resistive profile is prescribed. A V-configuration is used for directivity similar to the design used by Sandler [2] in 1962 for a traveling wave V-antenna for radio astronomy in space.

In this final report, focus will be given to a topical review of the various aspects of the antenna development program. Topics include the following:

1. Materials

   Chemical constituents, resistive measurements, element fabrication, testing.

2. Antenna Design and Evaluation

   Element design, V-structure, miniaturization, tusk antenna testing.

3. Antenna Loading

   Materials for increased earth coupling, element foreshortening.

4.3.2.1 Material Evaluation

Construction of resistive paper elements [3] suffers from many drawbacks. Most important for the GPR program is that it is not a useful construction technique for element miniaturization. A more useful technique would allow curved and folded elements to be constructed, thus reducing element size. An epoxy graphite mix was devised, and a measurement program was initiated for quality control [3]. In this early period, only the DC resistivity was measured.

A spiral configuration, "tusk" shaped in a V configuration, was designed to reduce the size for use in detecting ordnance. The center frequency is 450 MHz. A casting technique was used for fabricating the epoxy graphite antennas [3]. Two-section plaster molds were used to produce 900 MHz curved and straight elements.

A feasibility study was initiated [4] for using powdered metals in the epoxy-graphite mixture. Uneven distribution of the metals prevented further work on this approach. Recent investigation of alternate epoxy materials shows promise for increased control over electromagnetic properties [5]. A final evaluation of materials and antennas is expected in December, 1986, under contract N00014-86-C-2266.

4.3.2.2 Antenna Design and Evaluation

Original fabrication of reflectionless type elements by GEO-CENTERS involved paper type elements. They were made by

applying resistive paint to triangular shaped pieces of vellum. When the paper was rolled over a fiber glass tube (1/4" diameter), a triangular resistive taper was produced. Experiments on the V-antenna configuration had shown that an apex angle of 45 degrees produced half-voltage beam widths of 40 degrees. This compares very favorably with the commercial GSSI antenna which had near hemispherical coverage [6]. Increased signal levels (900 MHz design) were also reported.

A new directive radiating element was developed based on the Wu-King design. Two spiraled monopoles were combined into a "tusk" configuration [3]. The tusk antenna has the advantage that its physical size can be smaller than the V-configuration. Also, the driving point of the antenna was closer to earth, aiding in coupling the pulse into the ground. A photograph of the tusk antenna and its enclosure for field use is shown in Figure 4-3. Basic time and frequency domain calculations were begun to help in the design of the tusk elements [3].

Software was developed to predict the radiation properties of reflectionless antennas [7]. Using the approach of specifying the element geometry segment by segment, a wide variety of shapes were analyzed. This work was used to design the tusk configuration.

Tests using an earth chamber to compare the returned signal of the GSSI and the tusk antenna were encouraging [8].

To improve the polarization response of the tusk antenna, a cross configuration was developed [9]. Measurements were taken to characterize the interaction of a linearly polarized target rotated between a transmitter and receiver. Backscatter measurements using the cross configuration were also taken [10]. It was

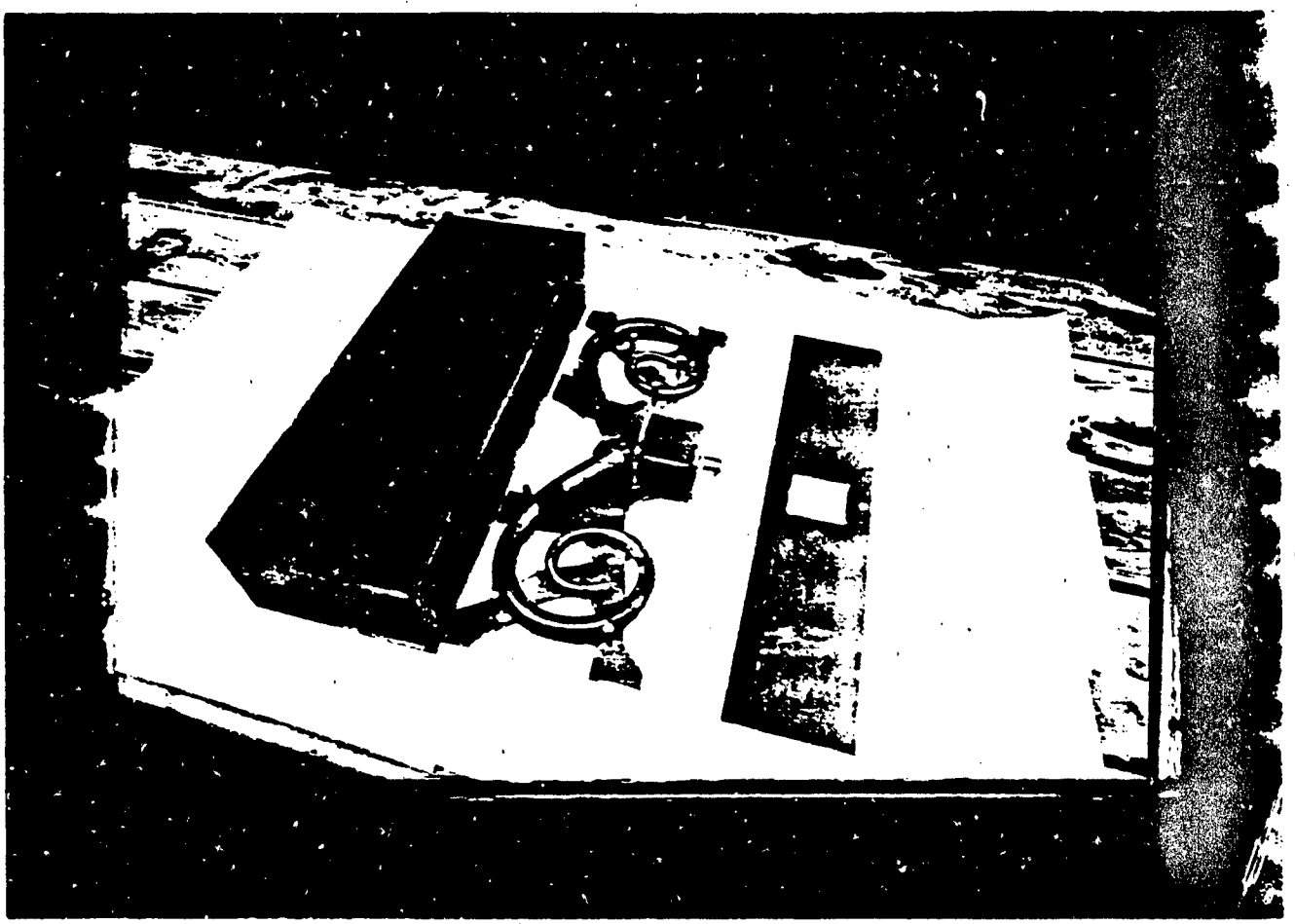

Figure 4-3. Tusk antenna with enclosure.

found that the cross configuration did not help the response of the tusk antenna by reducing effects of polarization and, in fact reduced signal strengths.

Antenna impedance is a very important parameter which allows optimum matching conditions. An impedance measuring program was started using field and laboratory conditions [10,11]. Measurements show that an impedance mismatch was present between the tusk antennas and their associated interface electronics to the GSSI system. This mismatch was responsible for reduced signal strengths found in the field experiments. Further antenna impedance measurements were made using a microwave network analyzer attached to a monopole tusk antenna above a ground plane. Results of these measurements have led to a much better understanding of effects due to the materials used for antenna fabrication than the previous DC measurements. This allows manipulation of constituent materials in the epoxy matrix to control impedance characteristics and allow better matching of the antenna. Final selection of antenna materials and fabrication of a better matched tusk antenna are expected in December, 1986, under contract N00014-86-C-2266.

4.3.2.3 Loading

A fixture was installed inside the anechoic chamber to study the effects of loading [4]. Titanium dioxide, due to its high dielectric constant, was considered as a loading material. Results for using loading materials showed no appreciable increase in coupling efficiency and caused additional attenuation of the signal [8].

4.3.2.4 Arrays

An experiment to investigate array configurations was designed and performed using one receiver and one transmitter [12]. Those simulated array data were obtained for a target buried 3 feet deep in the ground. Results of this field test were presented [13] along with an analysis of the simulation. Travel time data were analyzed, confirming expected results predicted by geometrical optics. Results of the experiments were used to design deconvolution algorithms for processing radar data. Additionally, these results have been useful in the design of a multi-element time domain array, as well as understanding methods useful for acquiring and analyzing multichannel data. With present knowledge, a simple array can be fielded with confidence in the success of the TD array principle.

4.4.0 DATA ACQUISITION AND CONTROL SYSTEM

4.4.1 Overview

Commercial GPR systems in general use primarily analog technologies and do not take advantage of recent advances in digital processing. GEO-CENTERS field experience with commercial systems combined with engineering expertise has led to the design of a new generation of GPR hardware, employing not only state-of-the-art electronics and data storage, but allowing the use of both current and future techniques in digital signal and array data processing.

To determine effective specifications for a new generation of GPR hardware, it was necessary to develop an interim radar system, not designed for field data analysis, but allowing real time digital data collection in the field. This system has been used to develop techniques in digital field data acquisition and storage, as well as to generate a computerized catalog of known ordnance items in varying soil conditions for the development of processing algorithms. The exploration of algorithms has occurred in parallel with hardware development. For this report, a discussion of the development and use of the interim radar system will be followed by a description of the conceptual design for a new generation of multichannel GPR hardware.

4.4.2 Interim Radar System

The interim radar system consists of a GSSI Subsurface Impulse Radar (SIR) System 7 and a COMPAQ Portable 286 microcomputer. The two systems are connected via custom hardware as shown in Figure 4-4. The development goal of this system was to provide

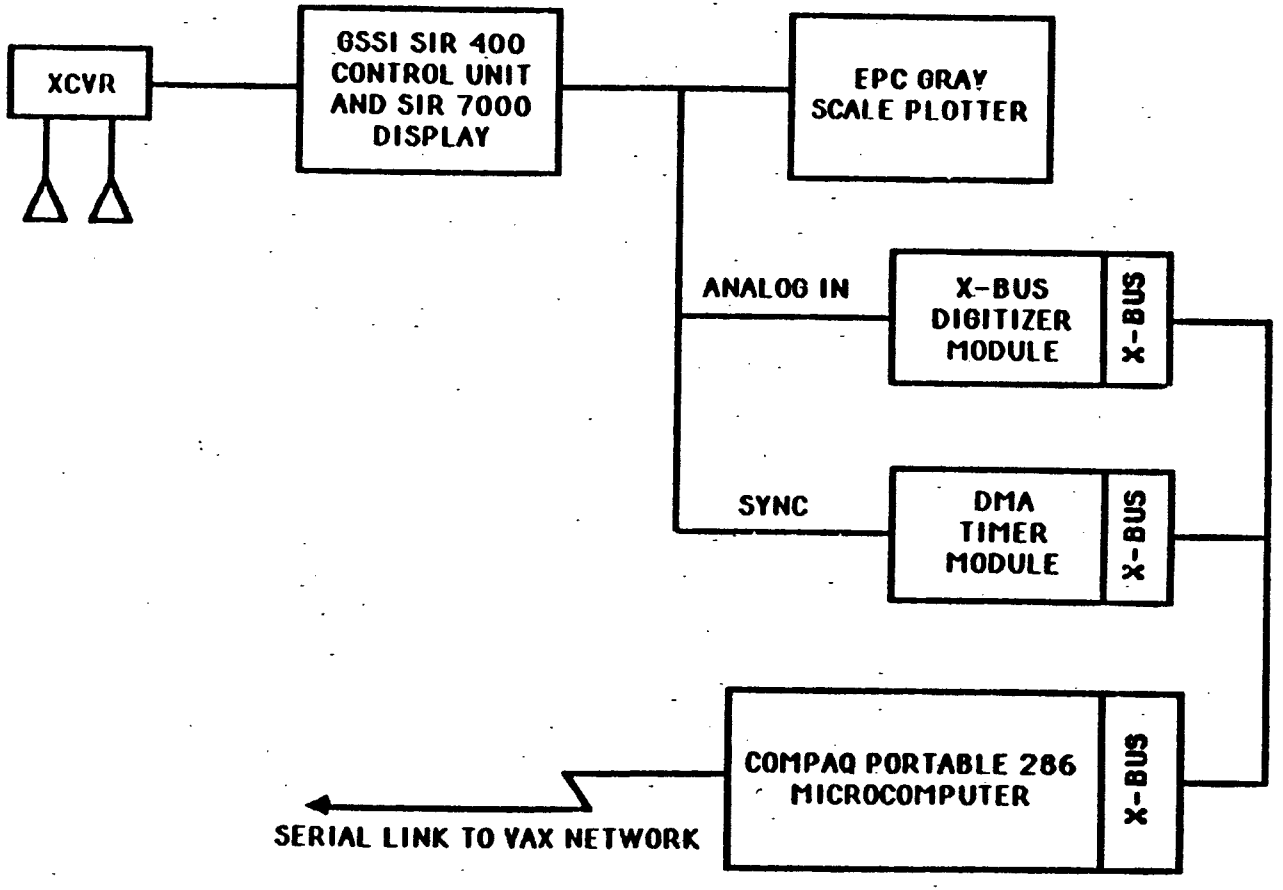

Figure 4-4. Block diagram of interim radar system.

digital data acquisition at a rate consistent with the actual field data acquisition where data are normally stored on magnetic tape in an analog (FM) format. This allows both real time data acquisition and digitization of previously recorded data at a normal playback rate (the previously used digitization process required a significant reduction in playback speed as well as substantial computing resources).

The data acquisition system was originally designed around an IBM PC/XT configured with two 10 MB disk drives and an image processor. This was later replaced by a faster, more rugged and portable computer, the COMPAQ 286, with a single 20 MB hard disk. Use of PC-compatible computers as the heart of the data acquisition system allows a relatively inexpensive and standard method of data access and exchange.

A relatively high data rate (13.2 Kbyte/sec minimum) is required for real time digitization of radar data from the GSSI system. This requirement made it necessary to use direct memory access (DMA) on the PC for data transfer. No commercial 8-bit analog to digital converter boards were available with a flexible DMA feature, so a custom implementation was designed using an external bus, known as the GEO-CENTERS X-BUS. The X-BUS is a simple 8-bit I/O channel designed to interface personal computers to simple data acquisition or control circuits over lengths of not more than two feet. A full description of the X-BUS and its implementation can be found in [9, Appendix A]. Also necessary for the interim radar system were an 8-bit analog-to-digital converter module [5, Appendix A], a DMA timer module [5, Appendix B], and an IBM PC to X-BUS converter [11, Appendix A]. All these modules were successfully built and utilized in field data acquisition, capable of average data storage rates of up to 16

kbytes/sec and instantaneous rates of 50 kbytes/ sec. Typically, 10 minutes of real time GSSI radar data (several scan lines) can be stored on the system.

Additional software development was necessary to utilize the data acquisition hardware. A pseudo disk operating system (P-DOS) was developed in order to create files to store real time data without the overhead required by the MS-DOS file structure. Utilities were also required for playback, screen display, printing of files, etc. Refinements of the software resulting from the use of the system in the field have led to two menu-driven programs built from several utility subroutines. One program, RADARAQ, is used to help maintain field logs while controlling the data acquisition. The second program, TRANSFER, allows selection of data from the P-DOS disk area to any of several outputs, either video or hardcopy displays, or several alternate file formats. Algorithms for data compression are also available during use of TRANSFER. With the use of commercial networking software, the system has also been integrated in the computer network at GEO-CENTERS, INC., allowing data exchange for processing, printing, and algorithm development on several different computers.

The interim radar system has been successfully fielded and used for radar data collection over known ordnance items. The use of the system in the field has aided in the development of requirements of an operational prototype radar system capable of multichannel array data acquisition.

4.4.3 Operational Prototype System

Prior to developing requirements of an operational prototype radar system, an analysis of the GSSI SIR system was performed to

determine where improved technology could be applied [14]. Results of this analysis showed several possible means of improving performance:

- Increased transmitter power
- Improved antenna efficiency
- Use of antenna arrays
- Increased receiver sensitivity
- Application of digital signal processing
- Improved operator controls
- Increased sampling rates

Additional design constraints dictate that the system be modular and flexible enough to allow easy integration of software algorithms, data processing hardware, and allow implementation of real time digital signal processing (DSP) hardware if modeling efforts prove it effective in increasing signal to noise.

Based on these criteria, GEO-CENTERS, INC. has investigated current technology and outlined the architecture of an operational prototype system. An overview of the system is shown in Figure 4-5. The system is designed to keep all analog radar electronics on the operational platform and transmit digital radar data via a fiber optic link for data storage and processing.

Components initially will consist of a single transmitter, eight receiver channels with digital output, a fiber optic data link, and control circuitry to decode commands and synchronize component operation. Commands consist of scan rate, number of receiver channels, gain settings, time window, etc., with provisions for additional as yet unspecified commands. The platform will be linked only by fiber optic and power cables.

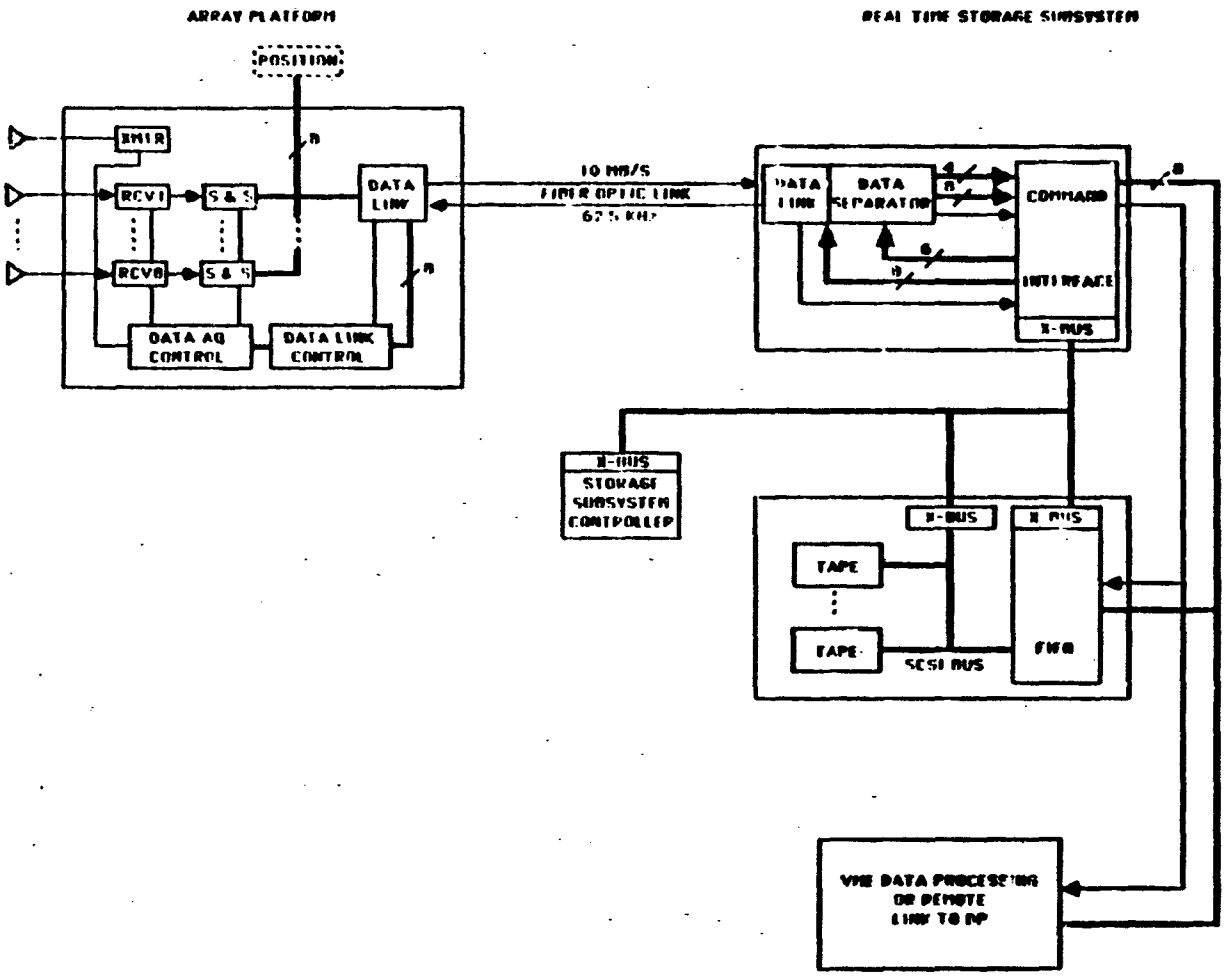

Figure 4-5. Conceptual architecture of operational prototype system.

The transmitter will consist of a pair of opposite polarity high voltage pulsers, one for each side of a dipole, capable of repetition rates up to 1 MHz. Each receiver channel will consist of a buffer stage for the antenna signal, a high gain amplifier, and a variable attenuator. The receiver is followed by a sample and stack network which samples the return waveform, digitizes it with a flash converter and saves the data in an accumulator. Eight samples are averaged (stacked) by the accumulator to increase the signal-to-noise ratio, and the data are then passed on to the data link via an internal 8-bit data bus. The data bus time-multiplexes the eight data channels to the data link, which defined the factor of eight in signal stacking. The data link circuits are identical on each end of the fiber optic link, consisting of transmitters, receivers, encoding/decoding, and control circuitry capable of serial transfer rates up to 10 Mbits/sec. Provisions have also been made to allow the addition of position data and future integration of real time digital signal processors on the platform. All of these components are in various stages of development under contract N00014-86-C-2266.

The storage subsystem is designed to function as a self-contained unit capable of storing large amounts of data quickly from a data acquisition system, allowing subsequent playback of the data into a signal processing system. This will allow initial signal processing algorithms to run slower than real time for developmental purposes, or at full speed to test real time processing.

A data processing system for field use on the operational prototype has not yet been specified. As specific data processing algorithms are selected for implementation on the prototype system, a data processing system will be implemented via the same

data path as the storage subsystem, using such industry standards as the VME bus. However, until speed and processing requirements are better defined, waiting to specify the processing architecture allows selection of the latest possible technology for data processing.

4.5.0 DATA PROCESSING

4.5.1 Introduction

Analysis of GPR data has traditionally been the domain of trained personnel with years of experience in data interpretation. In order to use GPR for range clearance, it is desirable to automate data analysis to the point where targets can be automatically identified and located by the instrumentation. Toward this end, GEO-CENTERS, INC. has examined and modeled several types of signal and data processing techniques and identified several that warrant advanced development for field testing.

4.5.2 Data Processing Techniques

Development of data processing techniques has required consideration of the vastly increased amounts of data expected from improved hardware and an array of multiple receivers. Real time signal processing methods leading to an increase in signal-to-noise ratio of radar data will lead to simplification of data analysis algorithms. Similarly, reduction of the amount of data will allow more time for data processing and less data requiring analysis. The data analysis algorithms need first to detect targets, then determine their depth and location.

GEO-CENTERS, INC. has performed a review of techniques used in real time digital signal processing, pattern recognition, image processing, and exploratory geophysics. Theoretical background, mathematics, and algorithms appropriate to these techniques are presented in detail in Appendix D. Techniques appropriate for use with GPR have been investigated further by either coding of al-

gorithms or modeling the effects of the algorithm on radar data. Several of the techniques examined have been eliminated from consideration, while several others warrant further development.

Techniques used for data analysis can be broken into two broad categories: signal processing and image processing. Signal processing is generally concerned with improving signal-to-noise ratio in single-channel or waveform data and may actually modify the data. Image processing may employ multichannel signal processing techniques (e.g., two dimensional deconvolution) as well as other techniques such as pattern recognition, which do not modify but, instead, examine and reduce the data.

Signal processing techniques can often be implemented in real time with special purpose hardware. For example, to aid in both data and noise reduction, real time sample stacking by a factor of eight will be incorporated in the hardware design of the receiver channels. This is a variation of the stacking techniques described in Appendix D. Image processing is often computer intensive, requiring relatively large amounts of memory and time. Reducing execution time of image processing software is possible by code optimization or use of additional hardware such as array processors, but this requires substantial development effort. For this reason, the data processing hardware configuration will not be finalized until algorithms for data reduction have been selected.

4.5.3 Overview of Developed Software

As previously mentioned, several potential algorithms have been modeled or coded by GEO-CENTERS. The programs on their respective computers are shown in Figure 4-6, with data shown

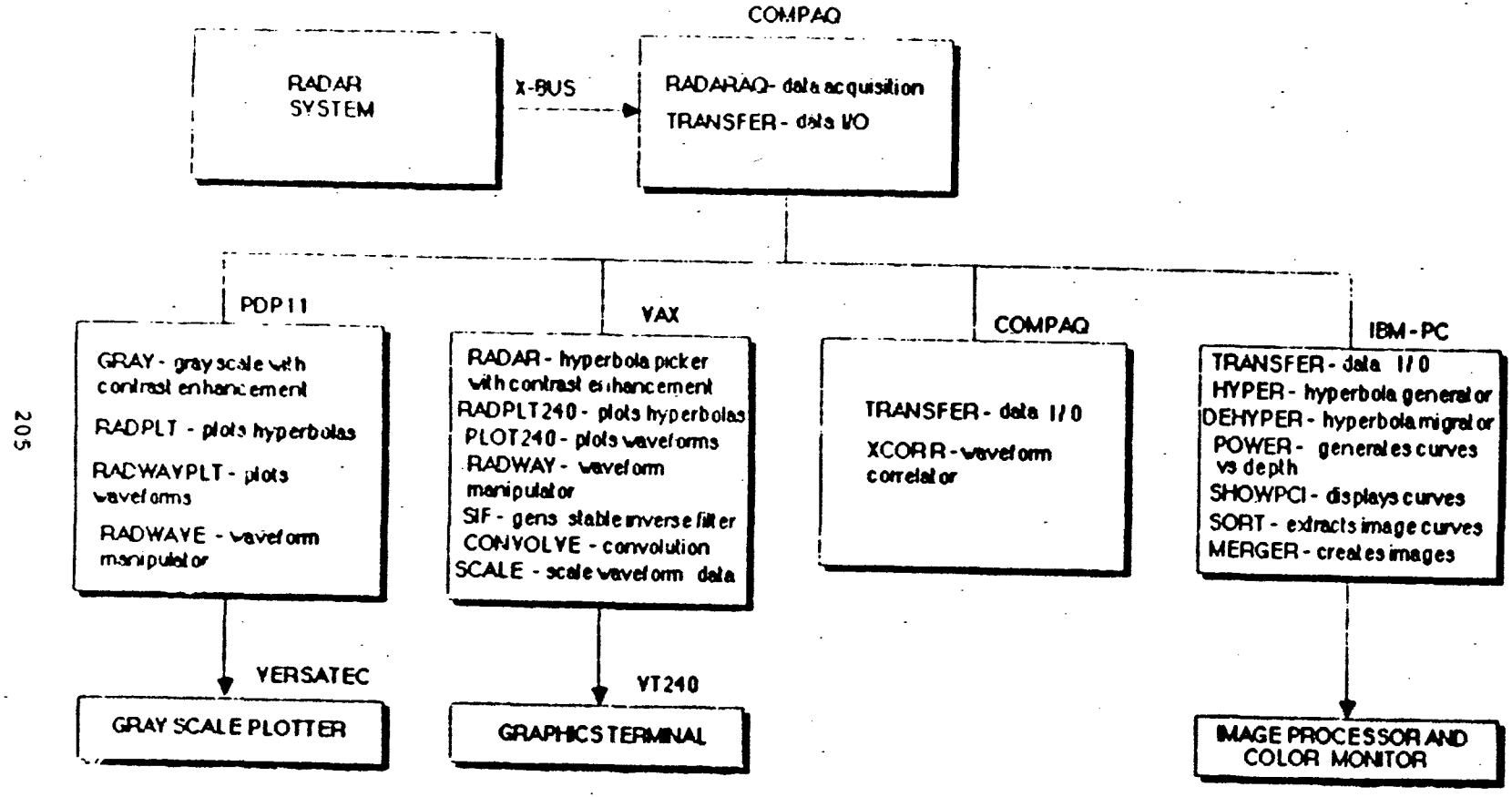

Figure 4-6. Overview of software and data flow for radar data acquisition and processing.

originating from the interim radar system on the top level. These programs consist of signal processing algorithms operating on individual waveforms (e.g., SCALE, RADWAVE), correlators of waveforms (e.g., XCORR), or programs to generate filters that operate on waveforms (e.g., SIF). Brief programs designed to evaluate techniques such as migration that can be performed through a variety of algorithms were written to determine if the concept was valuable enough to pursue algorithm optimization. Several other programs were written to display data either in different views or after different stages of processing.

As a result of this software development, several techniques have been identified that warrant use for range clearance. Digital filters can be very helpful in increasing signal-to-noise ratio. The difficulty in implementing these is that they must incorporate a calibration process performed in the field. An advantage is that they may be implemented in real time hardware on an array platform. Signal stacking is another signal processing technique that, as mentioned above, will be incorporated into the hardware design on the platform. This technique was used on almost all data taken on the field and was so common it became a software feature of the interim radar system in the TRANSFER program.

Two independent data analysis techniques have been identified to detect targets in field acquired data. The program RADAR is fully documented [5, Appendix C] and consists of several algorithms, any combination of which may be used to process data, where the common method is hyperbola recognition. This method is used because a reflected pulse from a target forms the general shape of a hyperbola as the radar approaches, passes over, then recedes from a target. A contrast enhancement algorithm was found

to aid automation of the program by freeing the user from setting most parameters. Figure 4-7 shows a raw radar data set from Fort Polk as plotted by the program GRAY on a Versatec gray scale plotter. Figure 4-8 shows the same data after being run through the contrast enhancement algorithm. Notice that the main features are more clearly visible. Figure 4-9 shows the results of the RADAR program on this data. Notice that the main feature is shown in bold indicating that the program has identified it as hyperbolic.

Another method, known as Power Curve Imaging (PCI) has also shown merit as a target detector [11]. Here hyperbolic data are run through a migration routine, and overlapping time (depth) sections of resulting waveforms are reduced to the amount of power reflected in that section. Shown in Figure 4-10 are data taken using GEO-CENTERS' tusk antennas at Indian Head with their associated power curves. The upper left shows raw data taken in the sand pit over several targets. To the right are six power curves derived at overlapping time sections. On the bottom left are the same data after migration, and the bottom right shows the associated power curves. Since each curve represents the total reflected power within a certain time (depth) range, the peaks of each curve should indicate the presence of an actual reflector within that range. It is easy to see, particularly for the mid-range reflectors, the peaks of the power curves from the raw data. Since the migration effect is smaller for shallow targets, they show a less dramatic improvement than deeper ones. Reflectors in these data consist of both ordnance items and shelves in the sand pit. Images created from the power values for a given time section will show "bright spots" in areas of high reflectivity, indicative of targets. Simple image processing techniques can easily pick out these bright spots.

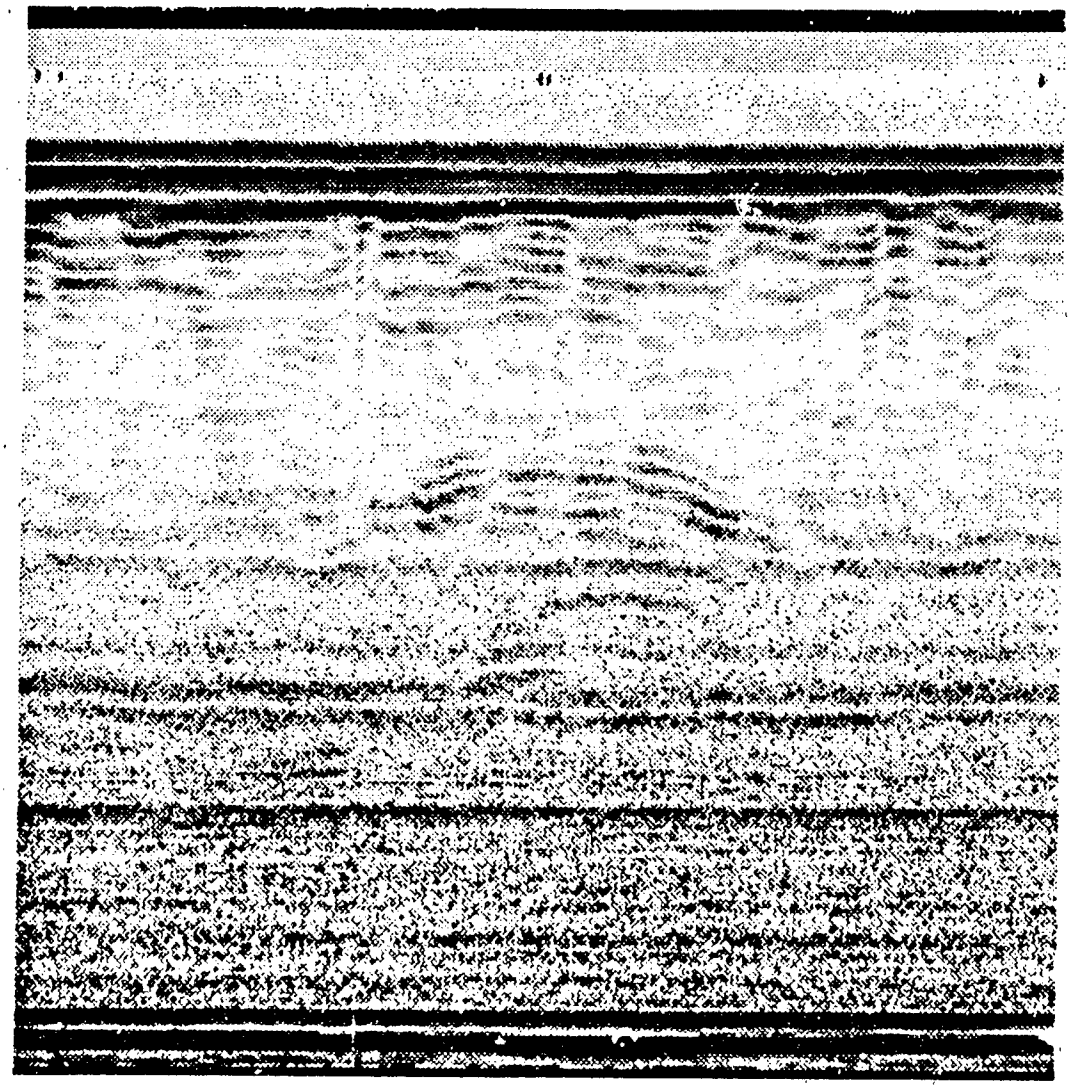

Figure 4-7. Raw data over a 91 mm projectile at Fort Polk, Louisiana.

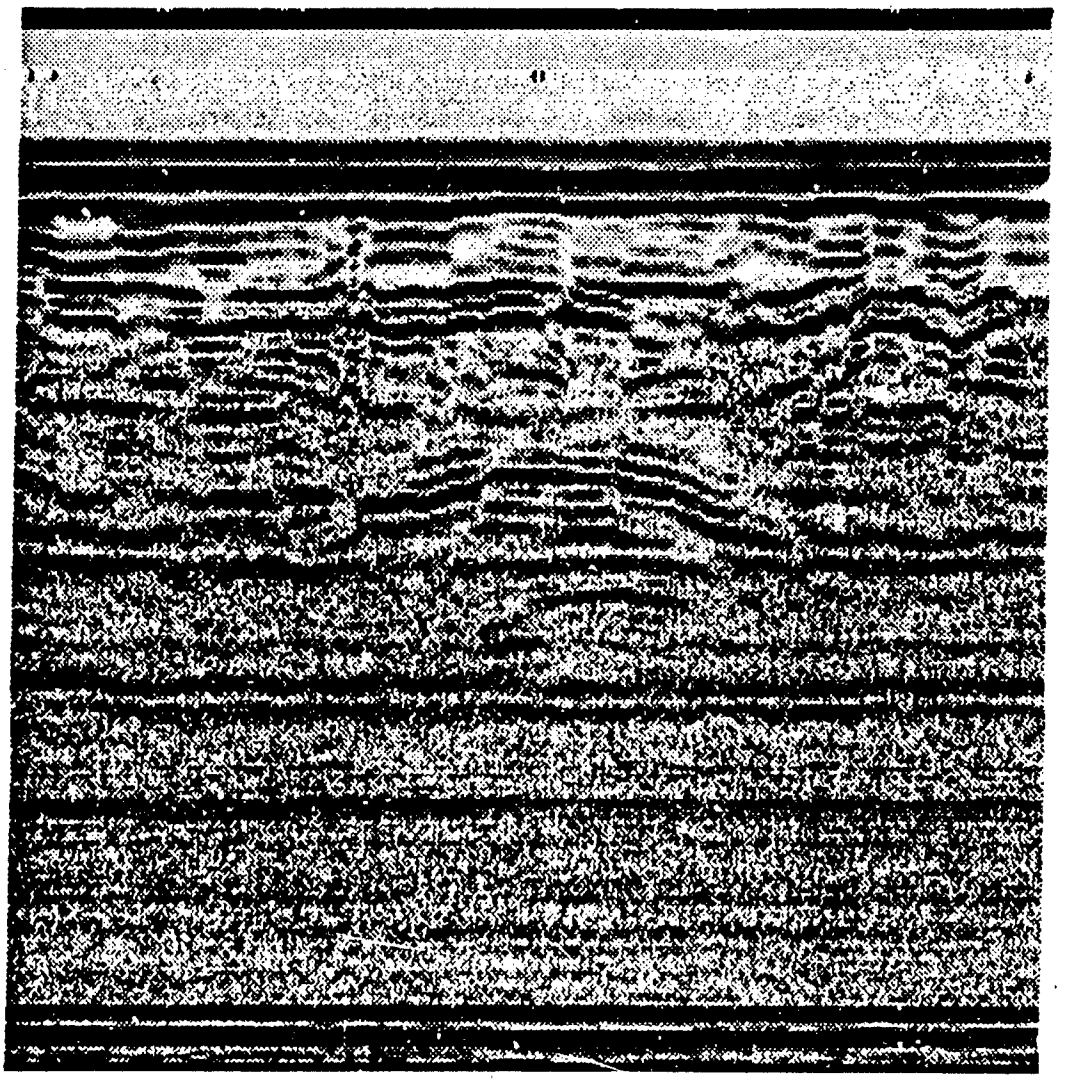

Figure 4-8. Contrast enhancement of Figure 4-7.

RADAR DATA FILE: DL1:FTP080.DAT

VERSION: COMBINATION IF-FILTER METHOD

PARAMETERS USED:

NAME	--->	WINDOW	SEGDIST	XDIST	YDIST	RADMIN	BYPASS
VALUE	--->	300	3	6	4	256	65
NAME	--->	SEGMIN	FTSMOOTH	XSMOOTH	YSMOOTH	ENDSRCH	POINTMIN
VALUE	--->	40	4	2	2	160	3
NAME	--->	ENDDEP	HYPSEC	CONWIND			
VALUE	--->	3	4	25			
NAME	--->	HSLOPE	LINDIF				
VALUE	--->	20.000	0.300				

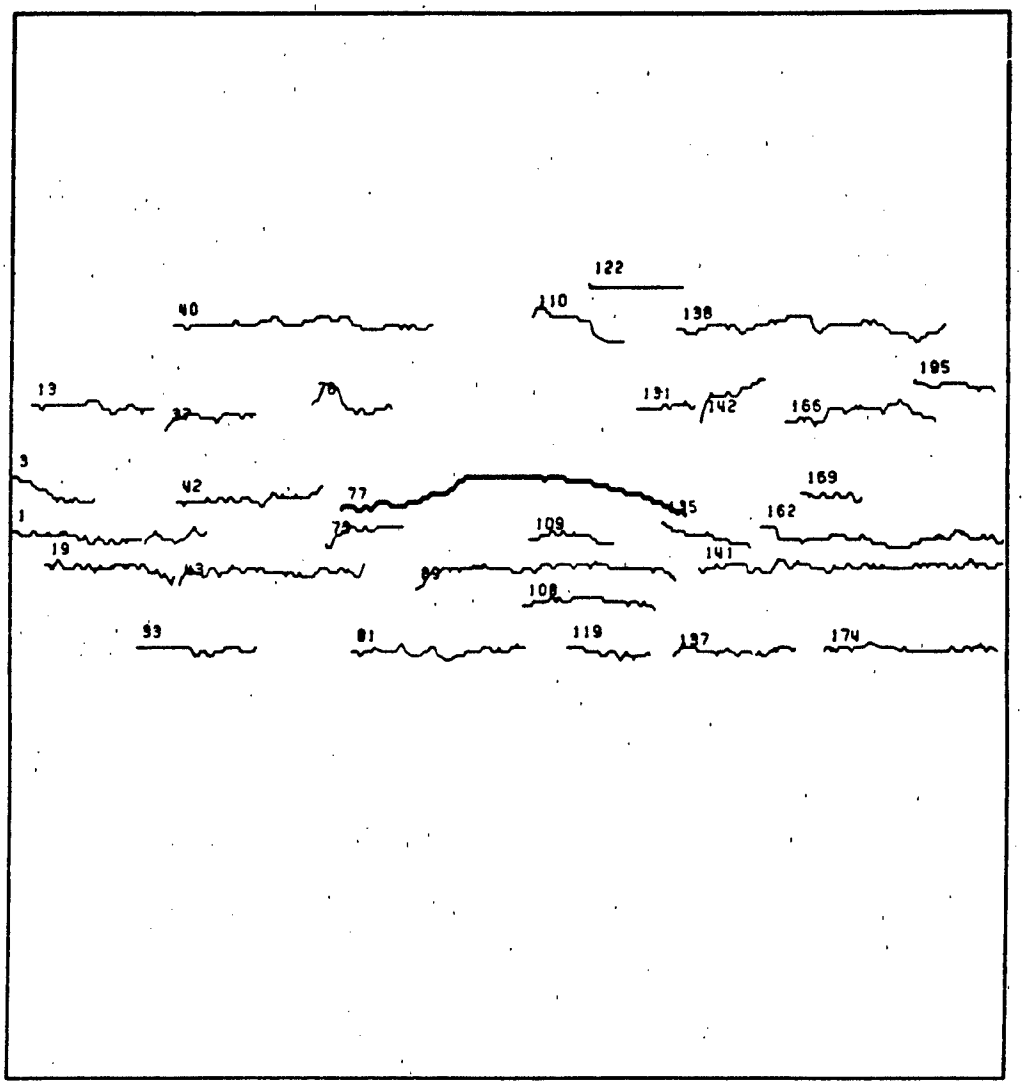

Figure 4-9. Feature extraction of data in Figure 4-8. The identified hyperbolic signature is shown in bold.

GEO-CENTERS, INC.

A) Raw data.

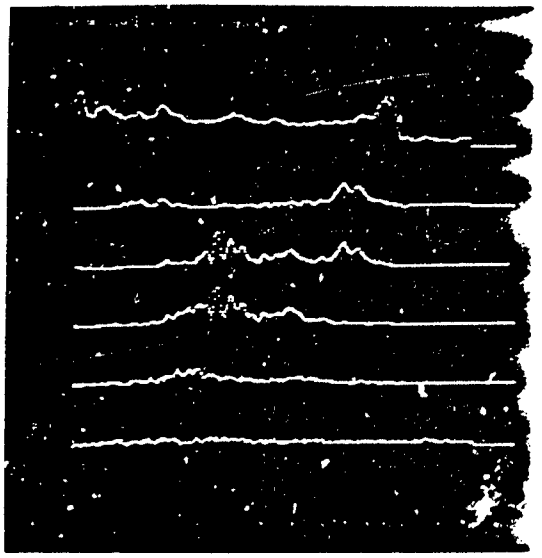

B) Power curves from raw data.

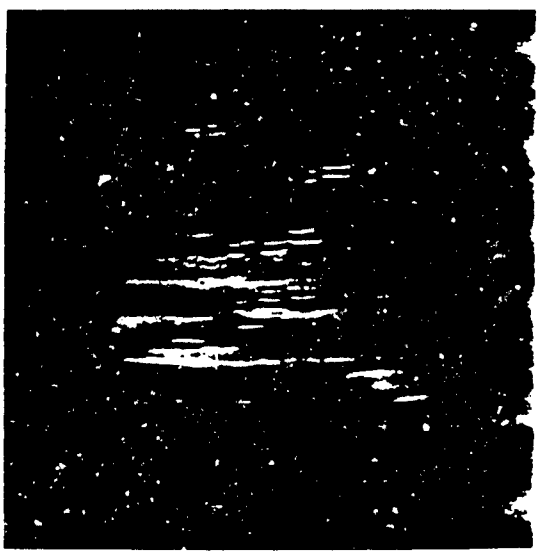

C) Migrated data from A.

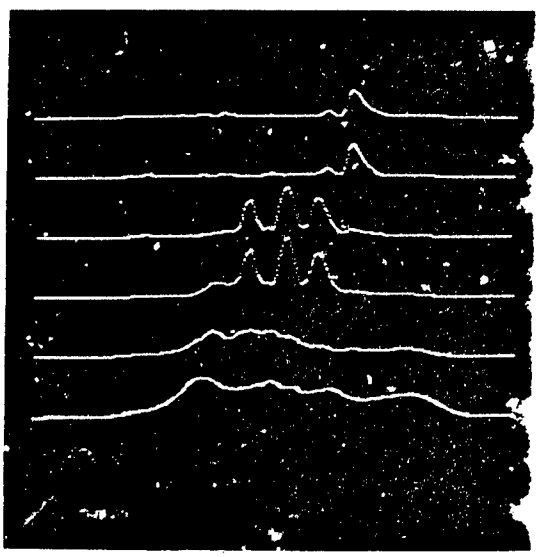

D) Power curves generated from migrated data.

Figure 4-10. Data taken in sand pit at Indian Head with tusk antennas.

The methods discussed above are multichannel techniques employing data from adjacent waveforms. Modifying these techniques to incorporate data from adjacent receivers is easily done and is the key to implementation of radar arrays. This is typically done in exploration geophysics by oil companies, where an impulse generator followed by an array of geophones is moved along the earth's surface. Although the frequency regime is different, it is very analogous to GPR, and many of the same analysis techniques apply.

4.5.4 Implementation of Data Processing

Detection of targets can be accomplished by the methods previously discussed. For field use, however, detection must be followed by location of the object. It is assumed that field implementation of data processing will incorporate external navigation either by adding it into the data stream from the platform or through the use of a system such as evaluated for use by STOLS (see Section 2.4.3). This information will allow location of surface position, while depth may be calculated by the computer from local calibration data determining propagation velocity in the soil. Data could be stored on digital mass storage such as tape cartridges, and a hardcopy map of targets could be printed out in the field following the field survey.

4.5.6 Field Surveys

4.5.6.1 Introduction

Over the performance period of the contract, three controlled field surveys were made at three different test ranges over known ordnance. The surveys had the common goal of obtaining a catalog

of radar signatures. Survey techniques and local geology differed for each site. Equipment evaluation was also a goal of the tests. The three test ranges were located at Fort Polk, Louisiana; Indian Head, Maryland (NAVEODTC); and Fox, Alaska (USA CRREL). Site descriptions and survey maps for each area are included for reference in Appendix E.

4.5.6.2 Fort Polk, Louisiana

The first GPR survey to locate ordnance was conducted at Fort Polk, Louisiana, from November 28 to December 6, 1984. The main purpose of this test was to begin generation of a catalog consisting of the radar signatures using different antennas over known ordnance. Examination of these signatures provided the initial determination of data processing techniques.

The survey was conducted with a GSSI System 7 SIR. Equipment consisted of a portable gasoline powered electrical generator, a power supply, a graphic recorder, and a tape recorder all mounted in a vehicle. Antenna frequencies used were 300 MHz and 1000 MHz. Data were recorded on magnetic tape and on a hardcopy graphic recorder; the latter information was compressed because of the high input rate (25.6 scans/sec). After the field survey, the magnetic tape data were played back at a slower speed to generate full-resolution hardcopy for visual analysis.

Data were taken over the targets within a very limited distance on either side of the ordnance items - on the order of 1 to 2 feet. At least two perpendicular scan lines were taken over each object. A full description of the survey and a catalog of hardcopy data can be found in a prior progress report [15]. These data were also played back and digitized after development of the

interim radar system. It was found that although these data were useful for waveform processing and development of pattern recognition analysis, there was not enough non-target data to simulate a real field survey. Therefore, subsequent surveys used long scan lines over targets, perhaps acquiring several targets on the same line for testing of data analysis.

4.5.6.3 Indian Head, Maryland

To aid in performance evaluation of ordnance detection technologies, it is desirable to have a test site where locations of buried targets is known with confidence and control over the site can be maintained. For this reason, a test site was built at the Naval Explosive Ordnance Disposal Technology Center (NAVEODTC) in Indian Head, Maryland. A resistivity survey [16] determined the ideal location for ordnance tests with GPR and, coincidentally, magnetics. A stepped pit was excavated and filled with graded sand, with ordnance items placed as described in Appendix E.

A series of field tests and experiments were conducted at the Stump Neck Road Test Site during the week of May 12-17, 1986. The tests were designed to accomplish three goals. The first was to create a new catalog of radar data taken over known ordnance items in both sand and clay. The second was to test and evaluate equipment developed to date. This included data acquisition hardware and software, tusk antennas, transmitters, and antenna reflectors. The third goal was to perform various antenna experiments examining effects of orientation, polarization, and dielectric loading. A full description of the survey can be found in a prior progress report [10].

This was the first field test to employ real time digital data acquisition through the use of the interim radar system. Although the test resulted in several software changes to aid in keeping track of data, the system performed extremely well, allowing data to be acquired at the GSSI's highest repetition rate of 51.2 scans/sec. Use of this data set has led to encouraging results in the testing of several algorithms (such as PCI) and further automation of data processing via the RADAR program. Several problems solved in the field have led to engineering design constraints for a final system, such as use of rigid cables in the analog signal paths and use of fiber optics for digital data links. Characterization of antenna polarization effects will also be useful for array design. Field experiments with antenna loading also confirmed laboratory experimental results that indicated marginal utility. In conclusion, the Indian Head survey resulted in several refinements in the interim radar system, as well as in signal and image processing and the specifications for an operational prototype system.

4.5.6.4 Fox, Alaska

A week long series of tests utilizing both ground penetrating radar and borehole techniques was conducted in Alaska between September 3 and 10. The test goals for surface radar were to examine ordnance detection capabilities in permafrost and local subsurface features found in permafrost regions. The site is currently used by U.S. Army CRREL for geophysical studies of permafrost and data are available from previous radar surveys at lower frequencies than used for ordnance detection.

This site is a variation on the Indian Head borehole test area, with only two targets buried, although a simulated third

target was added during the course of the testing. The site is described in Appendix E, and a description of the field tests can be found in [5].

Frozen ground generally provides good conditions for GPR. However, the top meter of thawed soil followed by a layer of ice rich soil proved to first attenuate the signal in the upper active zone and then reflect most of the energy of the radar pulse at the permafrost boundary, allowing very little signal to penetrate to the depths of the buried ordnance. This was especially true with the higher frequency antennas because of the increased attenuation at shorter wavelengths. Barely satisfactory penetration was obtained at 300 MHz, but nowhere near the penetration CRREL had obtained previously with 80 MHz antennas. However, data taken with the soil completely frozen (such as has been done by CRREL) may help at higher frequencies by eliminating the first meter of thawed soil which seems to substantially attenuate the signal. Therefore, use of GPR as a technique in northern latitudes with permafrost will likely be confined to winter time operation.

4.6.0 SUMMARY AND CONCLUSIONS

Significant improvements have been made in ground penetrating radar and a new flexible system incorporating advances in technology has been designed capable of acquiring digital radar array data, utilizing directional antennas, and implementing software to both aid in ordnance detection/location and in reducing operator expertise. Many parts of the system are already in the development stage.

Improvements have been made to a commercial GPR system (GSSI System 7) which allow real time digital data acquisition at the highest data rates capable from the GPR hardware. This system has been field tested with good success at two ordnance test ranges. Results of fielding the equipment have led to the specification of an operational prototype multichannel array ground penetrating radar system suited for ordnance detection and location.

The operational prototype system has been conceptualized and consists of an array of a single transmitting antenna with up to eight receiving antennas. System parameters will be under computer control, requiring less operator training. Directional antennas for use on the array have been developed with a center frequency of 450 MHz and a high front to back ratio. Improved materials for antenna construction are currently under evaluation. Several electronic subsystems have been designed and are in various stages of development and test.

Received radar data will be digitized and processed before being sent over to a real time storage subsystem. The subsystem will be used for both data storage and playback to test real time

signal processing algorithms implemented in hardware and advanced development of software algorithms designed for use with array data. It utilizes removable tape cartridges for the logging of field data.

A variety of signal processing and image processing algorithms have been researched, tested with field data, and evaluated. Several show promise for improvement in signal over noise and for use in automated analysis of radar data. In particular, hyperbolic pattern recognition and power curve imaging have been used to identify targets in field data, and signal stacking is commonly used for noise reduction. Multichannel techniques can also be implemented in array analysis software.

References

1. Wu, TT, and King, R.W.P., "The Cylindrical Antenna with Non-reflecting Resistive Coating", IEEE Trans. on Ant. and Prop., May, 1965, Vol. AP-13, No. 3, pp. 369-373.

2. Sandler, S.S., "Traveling Wave V Antenna for Radio Astronomy in Space" (for NASA), 1962-1965, Northeastern University, Boston, MA.

3. GEO-CENTERS, INC., "Ground Penetrating Radar System for Ordnance Location", 1985, prepared for USNRL/NAVEODTECHCEN, Report No. GC-IR-85-536.2B.

4. GEO-CENTERS, INC., Monthly Progress Report for April, 1985, prepared for NAVEODTECHCEN, Indian Head, Maryland.

5. GEO-CENTERS, INC., Monthly Progress Report for August-September, 1986, prepared for NAVEODTECHCEN, Indian Head, Maryland.

6. GEO-CENTERS, INC., "Directive Time Domain Antenna Design", 1982, prepared for EG&G, Inc., Report No. GC-TR-82-302.

7. Iuzzolino, H., "Time Domain Calculations", GEO-CENTERS, INC., April, 1985. (See also Ref. 9)

8. GEO-CENTERS, INC., Monthly Progress Report for May, 1985, prepared for NAVEODTECHCEN, Indian Head, Maryland.

9. GEO-CENTERS, INC., Monthly Progress Report for March, 1986, prepared for NAVEODTECHCEN, Indian Head, Maryland.

10. GEO-CENTERS, INC., Monthly Progress Report for April-May, 1986, prepared for NAVEODTECHCEN, Indian Head, Maryland.

11. GEO-CENTERS, INC., Monthly Progress Report for June-July, 1986, prepared for NAVEODTECHCEN, Indian Head, Maryland.

12. GEO-CENTERS, INC., Monthly Progress Report for July, 1985, prepared for NAVEODTECHCEN, Indian Head, Maryland.

13. GEO-CENTERS, INC., Monthly Progress Report for August, 1985, prepared for NAVEODTECHCEN, Indian Head, Maryland.

14. GEO-CENTERS, INC., Monthly Progress Report for September, 1985, prepared for NAVEODTECHCEN, Indian Head, Maryland.

15. GEO-CENTERS, INC., Interim Progress Report No. GC-TR-85536.2A, February, 1985, prepared for NAVEODTECHCEN, Indian Head. Maryland.

16. GEO-CENTERS, INC., Monthly Progress Report for October, 1985, prepared for NAVEODTECHCEN, Indian Head, Maryland.

SECTION 5

ELECTROMAGNETIC TAGGING OF ELECTRIC BLASTING CAPS

TABLE OF CONTENTS

LIST OF FIGURES

5.1.0 INTRODUCTION

We have investigated the feasibility of the remote detection of electrical blasting caps (EBC) using microwaves. EBCs are initiators for improvised explosive devices, which have been identified as a potential threat to commercial aviation. A reliable means to detect EBCs, therefore, would enhance airport security and contribute to air travel safety.

5.2.0 BACKGROUND

An effective microwave tag for EBCs must meet certain criteria: high detectability, low false alarm rate, conformability with existing EBC manufacturing design specifications, and low single unit cost in mass production quantities.

Four different microwave detection methods were investigated. The first three were disqualified for failing to meet the criteria stated above. All are discussed below for completeness.

5.2.1 Resonant Circuits

Resonant circuits are based on resistive (R), inductive (L) and capacitive (C) lumped circuit elements. These are all linear, passive components which form resonant RLC circuits when joined in certain configurations. An example is the LC tank resonator found in radio receivers. The resonant frequency, fo, is given by the formula

$$f_o = \frac{1}{\sqrt{LC}}$$

This method was ruled out because of the large physical size required for efficient, low loss L and C circuit elements.

5.2.2 Oscillating Micro-circuits

The method using oscillating micro-circuits is similar to the resonant circuit method discussed above, except that instead of

passive circuit elements, an active circuit acts as the tag. In effect, an active circuit behaves as a transponder, emitting a signal in response to an external stimulus. Such circuits are small (approximately 50 mils square) and can be incorporated into the body of an EBC. However, the high unit cost (on the order of $1.00) disqualifies this method from further consideration.

5.2.3 Re-radiating Striplines

This method uses lengths of stripline, which is an electrical transmission line fabricated from conductive foil, as tuned antenna elements. In response to a microwave pulse, the stripline "rings" with a characteristic oscillation. Because this phenomenon occurs with other articles, a high false alarm rate would be expected. This inherent drawback removes this method from consideration.

5.2.4 Microstripline Resonators

This method was selected for experimentation because it has the potential to satisfy all the criteria. Microstripline resonators, as the name implies, resonate like an LC circuit when excited by a microwave signal of the right frequency. They can be made small and inexpensive. They have been used in the telecommunication industry for years, so a lot is known about their design and fabrication. What is not known is how efficient they are as tags. To determine this, we undertook a feasibility study involving the design, fabrication and testing of microstripline resonators.

5.3.0 AMBIENT FIELD MEASUREMENTS

In order to identify regions in the radio-frequency (RF) spectrum which could be used for EBC detection without interfering with airport communications and radar, it was necessary to make measurements of the ambient RF background at airport baggage handling locations.

Measurements were made with an HP8559A Spectrum Analyzer connected to a set of shielded loop antennas at Logan International Airport, Boston, MA. Data were collected at three locations: the baggage claim area, the passenger screening portal, and a main corridor. In all three locations, a quiet region between 1.4 GHz and 2.2 Ghz was measured and very little RF activity was detected above 5 GHz. These regions were selected as possible microwave operating frequencies.

5.4.0 LABORATORY MEASUREMENTS

A measurements laboratory was set-up to conduct microwave backscatter measurements. The basic arrangement is illustrated in Figure 5.1. Major components of the system are: frequency generator, spectrum analyzer, power meter, transmit/receive horns, and an anechoic chamber.

5.4.1 Experimental Set-up

An anechoic chamber was constructed to provide a quiet region for microwave measurements. The 4x4x8 foot chamber is lined on the inside with a commercially available RF absorber which provides 30-40 dB attenuation of stray RF energy. The transmit/receive horn pair is mounted at one end of the chamber and a sample test platform is mounted at the other end. Baseline data were collected of the backscatter from the interior of the vacant chamber. This data revealed a smoothly varying standing wave pattern, as expected, resulting from the finite dimensions of the chamber (see Figure 5.1).

5.4.2 Resonant Cavity

A resonant cavity acts as a trap for electromagnetic energy of just the right frequency. The dimensions of the cavity uniquely determine which frequency is allowed inside. For a cube, the wavelength is given by the length of the diagonal on a side. A probe inserted through a wall of the cavity couples energy to the inside from external sources. At the precise resonant frequency, power flows into the cavity. In the case where the probe is connected to a wire pickup, acting as an antenna, the sudden

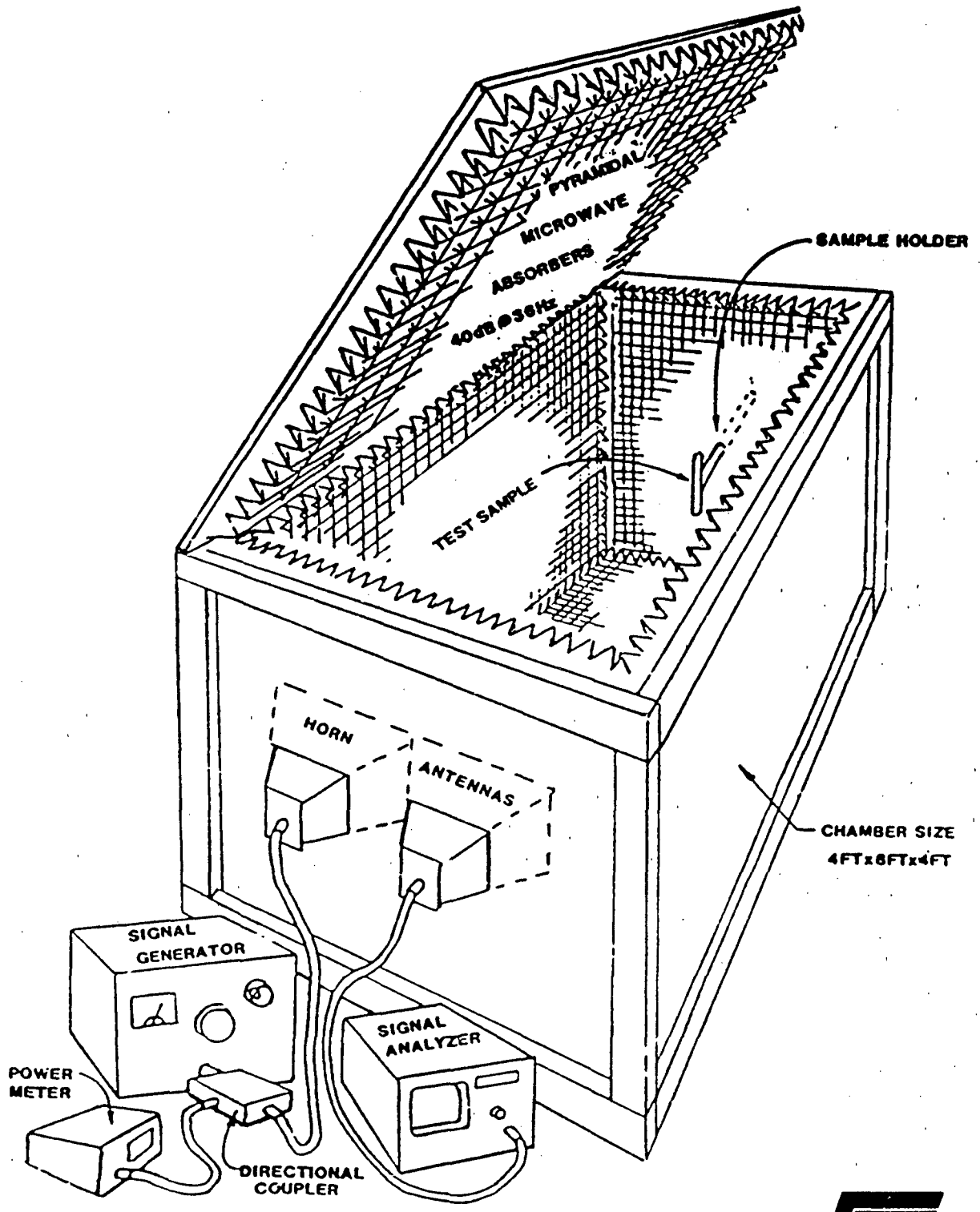

Figure 5-1. Isolation chamber.

GEO-CENTERS, INC.

in-rush of power to the cavity alters the radiation properties of the wire. The backscatter from a plain wire and a wire connected to the cavity should show a marked difference as a result.

The validity of the principle was demonstrated in the chamber using a resonant cavity, constructed from brass and designed to resonate at 2.0 GHz. The resonant response, as detected from the other end of the chamber, is shown in Figure 5.2.

Subsequent efforts went to realizing a comparable resonance response from a microstripline resonator. The following section summarizes the design and fabrication of test resonators.

5.4.3 Microstripline Circuits

A microstrip is a type of open wave guiding structure consisting of two pieces of copper cladding separated by a dielectric substrate. The upper surface of the dielectric supports a specific geometric contouring of the copper cladding while the entire lower copper surface is the conducting ground plane. Figure 5.3 depicts a rectangular microstrip patch. The coordinates (x',y') refer to the driving point where the rectangular patch is electrically driven with respect to the ground plane. When the patch is electrically excited, guided RF waves are set up between the patch and the ground plane. The rectangular microstrip acts very much like the desirable closed rectangular cavity resonator in that resonant modes are established corresponding to an absorbtion of energy. The essential difference between the two structures is the open sided nature of the microstrip that allows energy to radiate from these open edges. The undesirable radiation of energy is a problem encountered with any microstrip structure, but if the thickness of the dielectric is much smaller than a wave-

GEO-CENTERS, INC

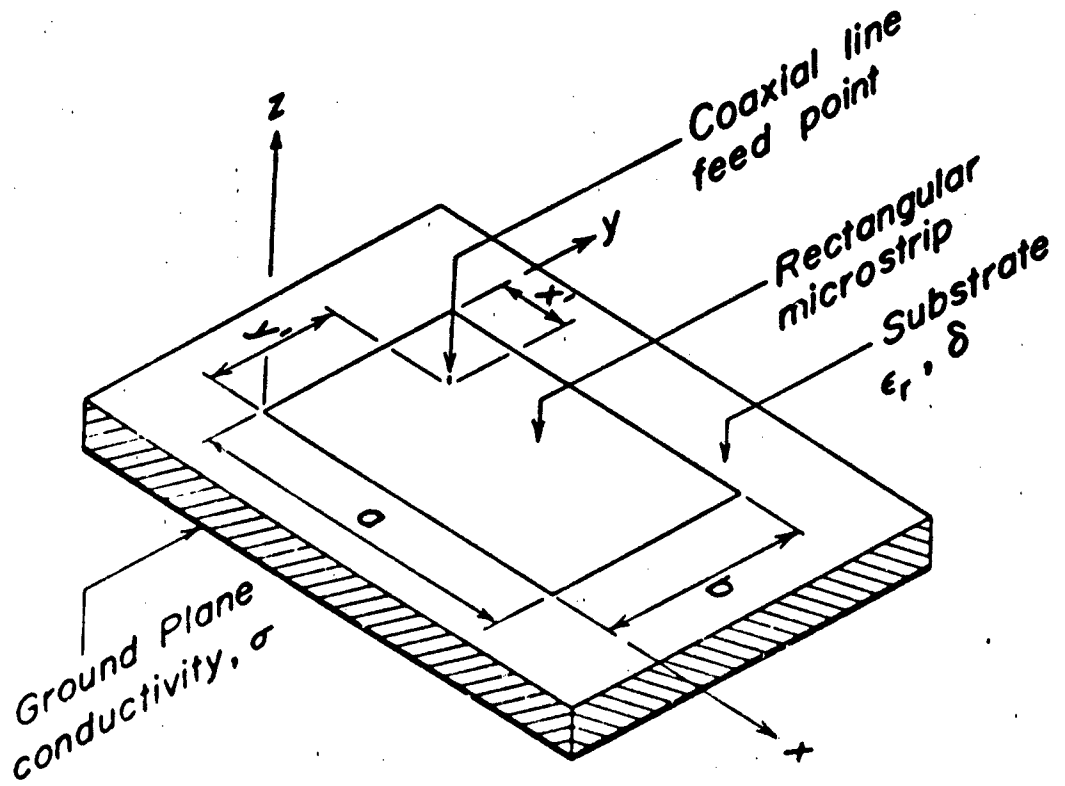

Figure 5-3. Rectangular microstrip.

length, then the patch can be viewed as a slightly leaky cavity, and appropriate expressions for the field distribution can be inferred. The design problem becomes one of maximizing the energy absorbed and at the same time minimizing the energy radiated.

A standard quantitative measure of how well a resonator performs is the quality factor, Q. Q is defined as the ratio of total energy stored to energy dissipated over one cycle. A high Q factor corresponds to a distinct drop in received energy (or an increase in absorbed energy) within a narrow frequency band centered at the resonant frequency of the microstrip. A low Q factor indicates an energy drop over a broader frequency band making the resonator signature less distinct and more easily masked by outside noise. For closed wall cavity resonators, such as discussed above, Q's in the 1000's are routinely achieved, whereas, even in theory, Q's for leaky cavities or microstrip resonators rarely reach into the 100's.

In addition to designing a microstrip resonator with a high Q, it is important to achieve an input impedance that is as closely matched as possible to the input impedance of the antenna attached to the microstrip to receive and transfer the RF signal. If a significant impedance mismatch occurs between the patch microstrip and the antenna, then very little RF energy will be passed to and, consequently, absorbed by the patch.

5.4.3.1 Rectangular Patch Resonators

Y.T. Lo and his coworkers (1,2) have been able to obtain good correlation between experiment and theory based on viewing a rectangular patch microstrip as a leaky cavity. The field under the patch is approximated by the dominant mode of the cavity

derived by enclosing the patch periphery by a magnetic wall. From this field, radiative and ohmic losses associated with the patch are determined together with stored energies. The resonant frequency and Q are computed at resonance and the impedance is calculated from the losses and stored energies.

The magnetic wall cavity model is founded on three conditions which are approximately true for thin (t<<lambda) substrates:

1. The electric field under the patch has only a z-component, and the magnetic field has only x and y components (z is normal to the patch).

2. The fields under the patch are independent of z.

3. The normal component of the electric current on the patch normal to the edge goes to zero at the edge. Hence, there is no tangential component of the H field at the sides of the cavity, to the degree that the above conditions are satisfied.

The analysis proceeds by expanding the fields inside the cavity in a complete set of cavity expansion modes. The coefficient of each mode is found from the particular feed used, and the internal fields of the cavity are found by summing all of the modal fields. The z-directed electric field is expressed as:

$$E = jk_o\eta_o \sum_{m=0}^{\infty} \sum_{n=0}^{\infty} \frac{\phi_{mn}(x,y)\phi_{mn}(x',y')}{k^2 - k_{mn}^2} j_o\left(\frac{m\pi d}{2a}\right)$$

where:

$k^2 = \varepsilon_r (1-j\delta) k_o^2$

$k_o = 2\pi f/c$

f is frequency

c is the speed of light

ε_r is the relative dielectric constant

δ is the loss tangent of the dielectric

$\phi_{mn}(x,y) = (\varepsilon_{om}\ \varepsilon_{on}/ab)^{1/2} \cos(m\pi x/a) \cos(n\pi y/b)$

$\varepsilon_{om} = 1$ for $m = 0$ and 2 for $m \neq 0$

d is the "effective width" of a uniform strip of z-directed source current of one amp

$\eta = 377\ \Omega$

$k_{mn}^2 = (m\pi/a)^2 + (n\pi/b)^2$

$j_o(x) = \sin(x)/x$

Once the electric field is obtained, then the magnetic field is:

$$H = 1/j\omega\mu_o \hat{z} \times \nabla E_z$$

and a magnetic current source, $K(x,y) = \hat{n} \times \hat{z}\, E(x,y)$ at the perimeter, with the unit normal, is defined. This source is allowed to radiate into space and the radiated power, Prad is found. Within the cavity, the power lost in the copper wall, Pcu, and in the dielectric, Pd, is calculated in a standard way.

From these losses, the input impedance Z is expressed as:

$$1/Z = [P + j2\omega(W_E - W_M)/|V|^2$$

where:

$P = P_d + P_{cu} + P_{rad}$
W_E is the time-averaged electric stored energy
W_M is the time-averaged magnetic stored energy
V is the driving point voltage which equals tE averaged over the feed strip

The magnetic wall leaky cavity assumption neglects the effects of the fringing fields present on the edges of any open structure. To account for these edge fields, an "effective length" for the patch dimensions is used which is slightly larger than the physical length. The amount of edge extension is a function of substrate thickness, patch dimensions, and frequency. There is considerable controversy among investigators as to an exact formula predicting edge extension. An approximate, linear formula is

$$\Delta l = k \cdot t$$

where delta l is the additional edge length, t is the substrate thickness, and k is a constant determined to be approximately 0.9 (personal communication with Y.T. Lo).

5.4.3.2 Modeling

In order to understand how microstripline width, substrate thickness, and substrate permittivity influence characteristic impedance and impedance as a function of frequency, a number of models were generated. Closed form expressions for characteristic impedance are from the work of Bahl and Garg(3). Equations relating characteristic impedance and effective dielectric constant

to frequency dispersion effects are from Getsinger(4) and Edwards and Owens(5). Figure 5.4 is a computer generated model of characteristic impedance as a function of microstrip width, substrate thickness and permittivity.

A Fortran computer program(6) for modeling resonant frequency, Q, and impedance Z(f),using Lo's magnetic wall leaky cavity theory for rectangular microstrip patches, was installed on the GEO-CENTERS MicroVAX computer. The source code listing is presented in Appendix F. The parameters of existing patches were input to the program to compare theory and experiment, and to determine the appropriate edge extension values. An analysis of a broad range of patch dimensions and driving point locations (feed points) was conducted to determine optimal parameters for a Q = 100, 80 ohm input impedance patch with a resonant frequency at about 2.0 GHz. The input impedance of a half-dipole antenna, which is used in our backscatter experiments, is approximately 80 ohms at resonance. Figure 5.5 is a listing of computer modeled values of Q, fo and Zo for a rectangular patch (1.5 cm x 4.7 cm) with a variable feedpoint (x',y').

A patch (#11-1.5) with dimensions of 1.5 cm x 4.7 cm was etched and the feedpoint was located at .75 cm along the shorter side and 1.9 cm along the longer side. This configuration resulted in the desired board with Q = 102, input impedance = 90 ohms, and the resonant frequency = 1.962 GHz.

5.4.3.3 Fabrication

The fabrication of a microwave resonator begins with a photo mask. The artwork created to produce a photomask is the negative of the actual design made at a scale of 5:1. The artwork is

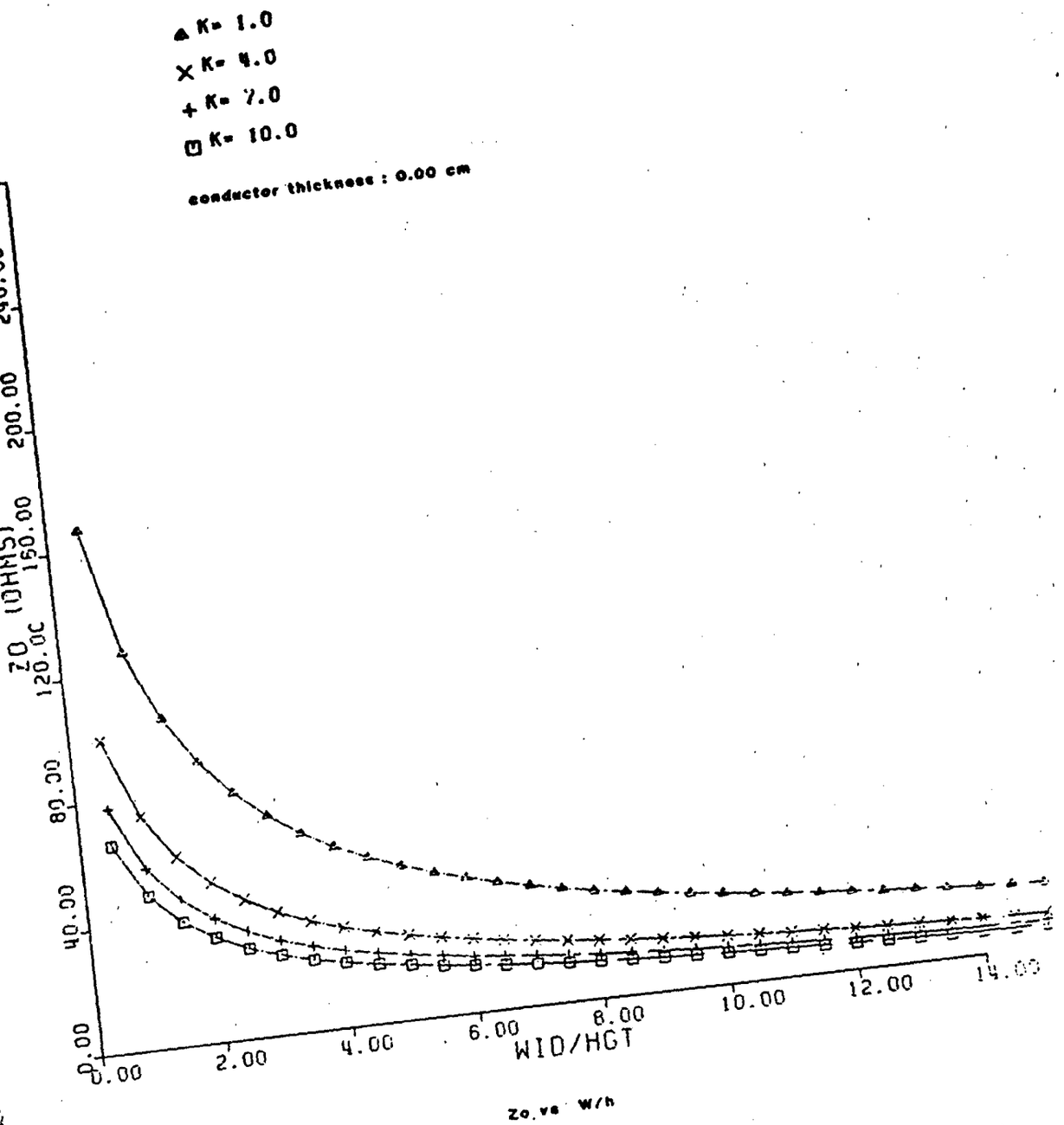

Figure 5-4. Computer model of impedance as a function of microstrip width.

RECTANGULAR MICROSTRIP

t= 0.1630000 d= 0.5000000 extension= 0.2934000

A	B	X	Y	Q	FO		ZO
1.50	4.70	0.75	0.00	131.43	1962.23	1856.84	6.66
1.50	4.70	0.75	0.10	131.43	1962.23	1828.02	4.88
1.50	4.70	0.75	0.20	131.43	1962.23	1785.08	3.53
1.50	4.70	0.75	0.30	131.43	1962.23	1728.72	2.45
1.50	4.70	0.75	0.40	131.43	1962.23	1659.83	1.59
1.50	4.70	0.75	0.50	131.43	1962.23	1579.49	0.93
1.50	4.70	0.75	0.60	131.43	1962.23	1489.00	0.43
1.50	4.70	0.75	0.70	131.43	1962.23	1389.76	0.10
1.50	4.70	0.75	0.80	131.43	1962.23	1283.34	-0.09
1.50	4.70	0.75	0.90	131.43	1962.23	1171.45	-0.15
1.50	4.70	0.75	1.00	131.43	1962.23	1055.84	-0.08
1.50	4.70	0.75	1.10	131.43	1962.23	938.34	0.10
1.50	4.70	0.75	1.20	131.43	1962.23	820.83	0.36
1.50	4.70	0.75	1.30	131.43	1962.23	705.13	0.69
1.50	4.70	0.75	1.40	131.43	1962.23	593.09	1.08
1.50	4.70	0.75	1.50	131.43	1962.23	486.48	1.50
1.50	4.70	0.75	1.60	131.43	1962.23	386.99	1.93
1.50	4.70	0.75	1.70	131.43	1962.23	296.19	2.35
1.50	4.70	0.75	1.80	131.43	1962.23	215.49	2.75
1.50	4.70	0.75	1.90	131.43	1962.23	146.20	3.11
1.50	4.70	0.75	2.00	131.43	1962.23	89.41	3.42
1.50	4.70	0.75	2.10	131.43	1962.23	46.02	3.66
1.50	4.70	0.75	2.20	131.43	1962.23	16.70	3.82

Figure 5-5. Computer modeled Q, fo and Zo for microstrip patch parameters.

t = substrate thickness
d = effective current width
extension = edge extension

photographically reduced by a factor of five, thus producing a very precise mask of the design. The design is then transferred to the copper clad test material. For our tests we selected Rexolite 2200 board manufactured by Norplex/Oak Laminates Division. Rexolite 2200 has a dielectric constant of 2.64, dielectric thickness of 0.062 inches, and two sides of 1 oz. copper cladding.

The Rexolite stock material is cleaned with an alumina polishing solution and degreased, prior to being photosensitized with a positive photoresist. The sensitized board is covered with the mask and exposed under a photoflood lamp. The exposed board is transferred to a solution of etchant (ferric chloride), which removes the unexposed copper areas. The board is washed and cleaned with acetone. After visual inspection for surface imperfections, the board is readied for testing. A SMA type connector is used to connect the board to test instruments. A hole is drilled at the location of the feedpoint and the SMA connector is soldered directly to the board; the center pin is soldered to the microstrip side, and the connector body is soldered to the ground plane.

5.4.3.4 Characterization and Results

The microstrip patch resonator is primarily characterized by three parameters: resonant frequency (fo), quality factor (Q), and input impedance as a function of frequency (Z(f)). The quantities are measured using an HP8410C network analyzer with the HP8743 and HP8745 transmission/reflection test sets. An HP8305B oscillator supplies microwave frequencies in the range from 0.01 to 8.4 GHz.

Energy from the microwave generator is directed through the transmission/reflection test set and coupled to the resonant patches through SMA coaxial connectors, which are soldered directly to the test boards. Reflected energy is directed through the transmission/reflection test set to the network analyzer for display and plotting. A block diagram of the experimental test set-up is given in Figure 5.6. The network analyzer displays the complex impedance as a function of frequency directly on a Smith chart screen overlay. Patch resonance occurs when the input impedance is solely a real quantity. This corresponds to the center horizontal line on the Smith chart, hence, the resonant frequency and resonant impedance are easily read directly from the chart.

In order to determine Q, two additional curves must be drawn on the Smith chart indicating the 3 dB down points for the energy on either side of resonance. Q can be calculated as the ratio of the resonant frequency to the difference in frequencies of the two 3 dB down points: $Q = fo/\Delta f$. Figure 5.7 indicates the position of the 3 dB curves for a Smith chart. With these lines drawn on the Smith chart overlay, Q factor can be readily calculated. Figure 5.8 is a Smith Chart plot complex impedance as a function of frequency for patch #11-1.5. The 3 dB down points for calculation of Q are indicated.

Four rectangular patch boards with directly measured Q's in the 70-102 range have been tested in the chamber. While no significant energy absorption was observed at resonance, a small drop in energy was seen, Figure 5.9, which is of the same level as the background noise.

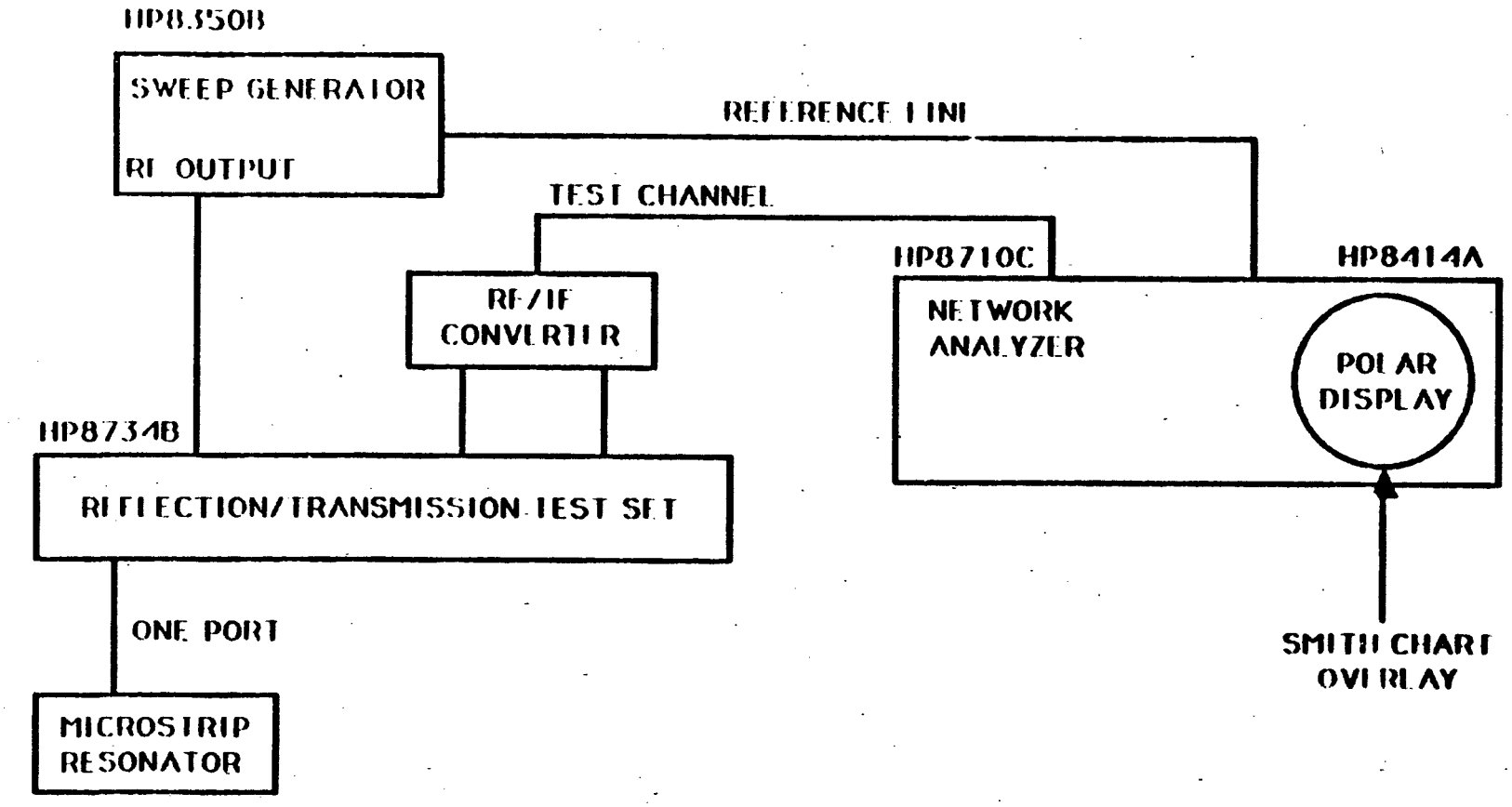

Figure 5-6. Block diagram of experimental test set-up.

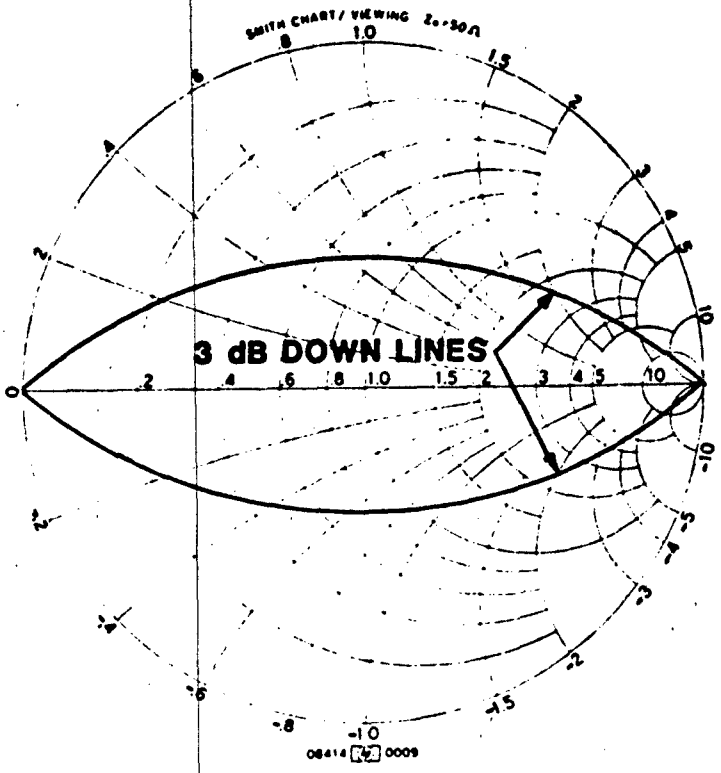

Figure 5-7. Smith chart with 3 dB down lines.

GEO-CENTERS, INC.

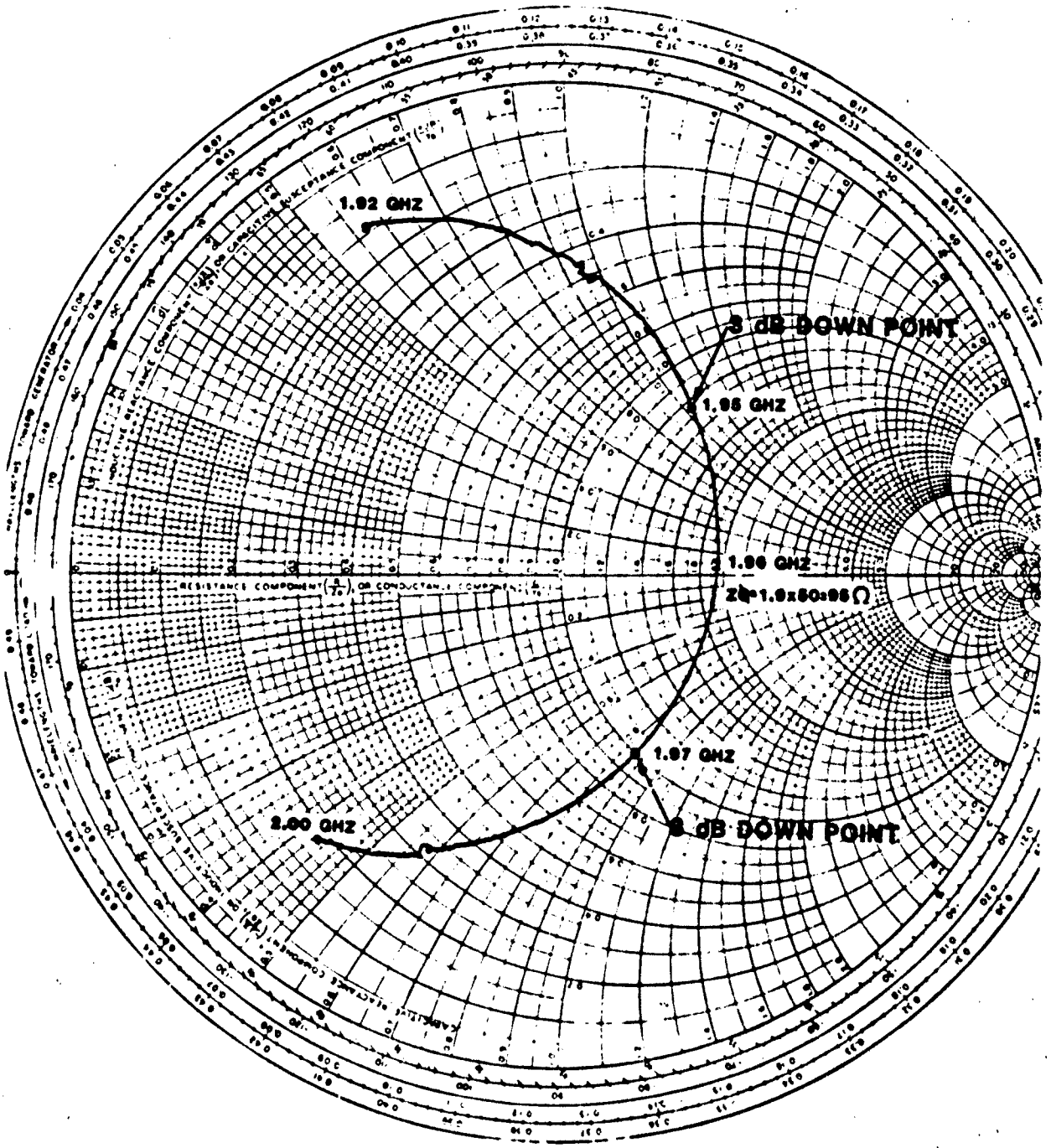

Figure 5-8. Complex impedance as a function of frequency for patch 11-1.5. Q = fo/Δf = 1.962/(1.970-1.951) = 102

GEO-CENTERS, IN

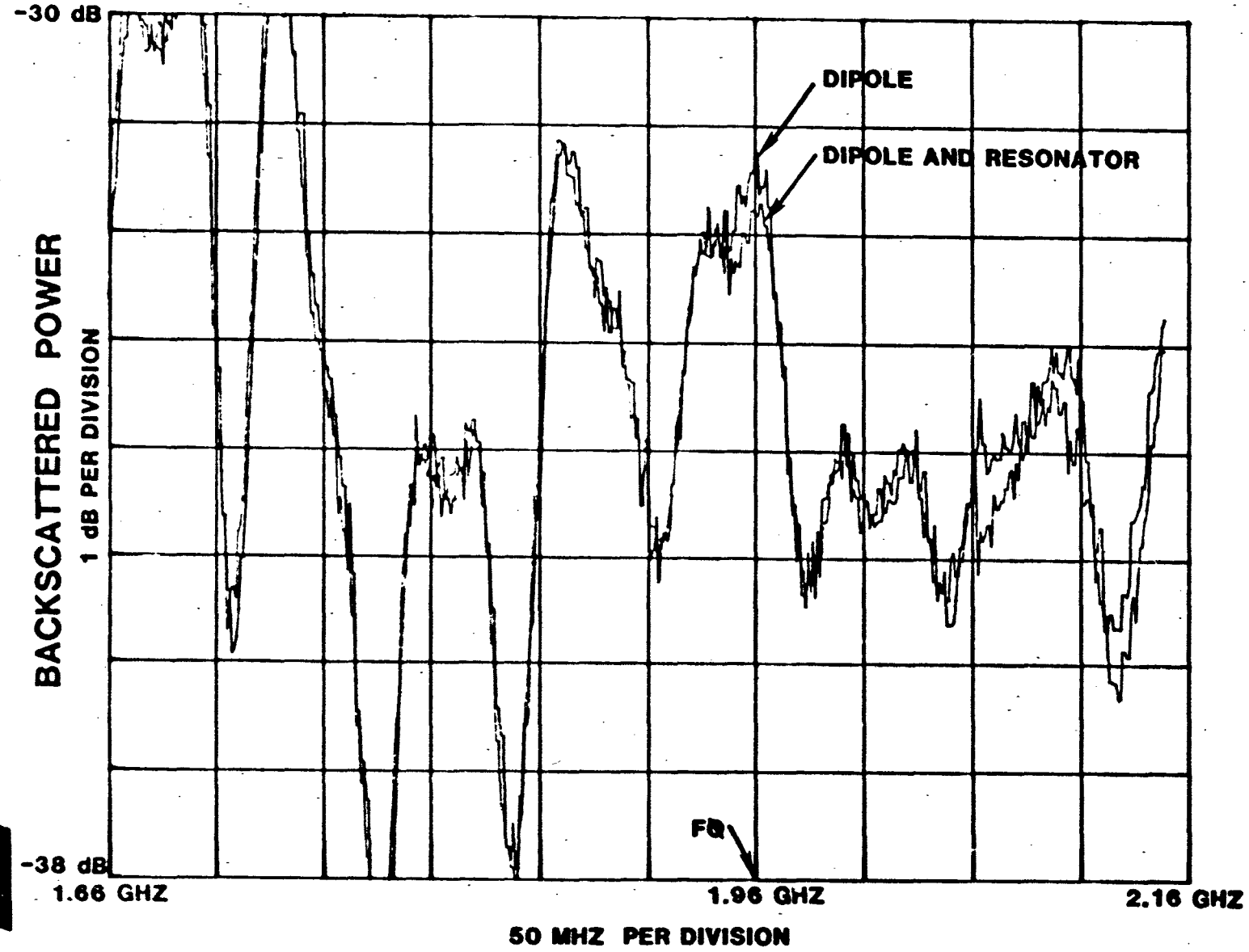

Figure 5-9. Resonance of rectangular microstrip resonator 11-1.5.

In addition to the above parameters, the boards are characterized by their physical dimensions, driving point locations, dielectric constant of the substrate, and substrate thickness, which are all easily obtainable quantities.

5.5.0 CONCLUSION

Accomplishments include the standardization of board production, the refinement of test procedures and equipment, the implementation of a computer model on the MicroVAX, and the design of resonant patches that yield data consistent with theory. The production of the desired 102 Q board with an input impedance of 90 ohms has been achieved. Unfortunately, desired absorption of energy at resonance has not been definitely established.

References

1. Lo, Y.T., Solomon, D., and Richards, W.F., "Theory and Experiment on Microstrip Antennas", IEEE Trans., Vol. AP-27, pp. 137-145, March, 1979.

2. Richards, W.F., Lo, Y.T., and Harrison, D.D., "An Improved Theory for Microstrip Antennas and Applications", IEEE Trans., Vol AP-29, January, 1981, pp. 38-46.

3. Bahl, I.J. and Ramesh, Garg, "Simple and Accurate Formulas for Microstrip with Finite Strip Thickness", Proc. IEEE, Vol. 65, 1977, pp. 1611-1612.

4. Getsinger, W.J., "Microstrip Dispersion Model", IEEE Trans., Vol. MTT-21, 1973, pp. 34-49.

5. Edwards, T.C., and Owens, R.P., "2-18 GHz Dispersion Measurements on 10-100 ohm Microstrip Line on Saphire", IEEE Trans., Vol MTT-24, 1976, pp. 506-513.

6. Richards, W.F. and Lo, Y.T., "A Fortran Program for Rectangular Microstrip Antennas", RADC-TR-82-78, April, 1982.